

University of Louisville

ThinkIR: The University of Louisville's Institutional Repository

Electronic Theses and Dissertations

5-2023

Compositional engineering of precursor inks for intense pulsed light compatible deposition of perovskite solar cells.

Blake Martin
University of Louisville

Follow this and additional works at: <https://ir.library.louisville.edu/etd>



Part of the [Chemical Engineering Commons](#)

Recommended Citation

Martin, Blake, "Compositional engineering of precursor inks for intense pulsed light compatible deposition of perovskite solar cells." (2023). *Electronic Theses and Dissertations*. Paper 4113.
Retrieved from <https://ir.library.louisville.edu/etd/4113>

This Doctoral Dissertation is brought to you for free and open access by ThinkIR: The University of Louisville's Institutional Repository. It has been accepted for inclusion in Electronic Theses and Dissertations by an authorized administrator of ThinkIR: The University of Louisville's Institutional Repository. This title appears here courtesy of the author, who has retained all other copyrights. For more information, please contact thinkir@louisville.edu.

COMPOSITIONAL ENGINEERING OF PRECURSOR INKS FOR INTENSE
PULSED LIGHT COMPATIBLE DEPOSITION OF PEROVSKITE SOLAR CELLS

By

Blake Martin
B.S. Centre College, 2016

A Dissertation
Submitted to the Faculty of the
J.B. Speed School of Engineering
In Fulfillment of the Requirements
For the Degree of

Doctor of Philosophy
In Chemical Engineering

Department of Chemical Engineering
University of Louisville
Louisville, KY 40292

May 2023

COMPOSITIONAL ENGINEERING OF PRECURSOR INKS FOR INTENSE
PULSED LIGHT COMPATIBLE DEPOSITION OF PEROVSKITE SOLAR CELLS

By

Blake Martin

B.S. Centre College, 2016

A Dissertation Approved on

April 27, 2023

By the Following Dissertation Committee

Dr. Gautam Gupta

Dr. Thad Druffel

Dr. Delaina Amos

Dr. Gerold Willing

DEDICATION

To my wife, Shannon, who has been my constant source of support throughout this journey, and my daughter, Lily, who never fails to brighten my day and motivate me to do better, I dedicate this dissertation.

To my parents and family, who have always believed in me and provided me with the foundation to pursue my dreams, and to my friends and colleagues, who have stood by my side through thick and thin, I am eternally grateful for your unwavering love and encouragement.

ACKNOWLEDGEMENTS

I would like to express my sincerest gratitude to my advisors, Dr. Thad Druffel and Dr. Gautam Gupta, who have offered their invaluable guidance, insight, and expertise throughout the course of this project. Your patience, wisdom, and mentorship have been instrumental in shaping not only this dissertation but also my growth as a researcher and scholar.

My heartfelt thanks go to the University of Louisville, which has provided me with an environment conducive to learning and exploration. The resources, facilities, and opportunities afforded by this institution have been critical to my success in this endeavor.

I am grateful to the National Renewable Energy Laboratory for their collaboration and support, which have significantly enriched the quality of my research. Your dedication to advancing the frontiers of science has been an inspiration and a driving force behind my work.

Lastly, I wish to acknowledge the Department of Energy for their generous funding and support of this project. Your commitment to fostering innovation and progress in the field of energy has made this research possible and has contributed to the advancement of knowledge in our shared pursuit of a sustainable future.

To all who have played a part in this journey, I offer my deepest appreciation and gratitude.

ABSTRACT

COMPOSITIONAL ENGINEERING OF PRECURSOR INKS FOR INTENSE PULSED LIGHT COMPATIBLE DEPOSITION OF PEROVSKITE SOLAR CELLS

Blake Martin

April 27th, 2023

Perovskite solar cell (PSC) technology presents a promising alternative to silicon-based photovoltaics (PVs), yet the challenges of stability, module efficiency, and scalability remain significant obstacles to its commercialization. The drive to attain optimal efficiency has resulted in substantial advancements in PSC technology, as power conversion efficiencies (PCEs) now match those of crystalline silicon (c-Si) cells. However, it is important to note that while these solutions have made progress in PSC commercialization, they often partially resolve issues or create new challenges that must be addressed. To proactively address and deter commercialization challenges, the field of PSCs needs a comprehensive approach to consider the interplay between compositional engineering, thin-film deposition, drying, and annealing processes, and their impact on PSC efficiency, durability, scalability, and bankability. The aim of this study is to explore potential solutions to overcome the scalability and cost limitations of PSCs, addressing many of the technical barriers to commercialization.

Our methodology begins by leveraging the existing understanding of perovskite thin film deposition and translating it into scalable analogs. Conventionally, perovskite solar cells are deposited in three stages: deposition, translational phase formation, and annealing. To adapt this approach for scalable platforms, we employ wide-area

depositions using meniscus coating methods (blade- and slot-die coating), drying via forced laminar airflow, and annealing through radiative annealing methods. By constraining our process methodology in this manner, we were compelled to explore creative solutions within other process parameters, ultimately yielding a process that is more amenable to roll-to-roll fabrication.

First, perovskite solar technology is an economically viable PV based primarily on low cost of materials and scalable manufacturing. Solution phase deposition of all active layers lends itself towards roll-to-roll manufacturing, a well-established platform with production rates of several hundred square meters per minute. A technoeconomic analysis was conducted to consider the opportunity to scale at this production throughput with manufacturing exceeding 1 GW per year in a single plant. IPL is utilized to minimize costs associated with the footprint, equipment and operation. The analysis is limited to the operation of the roll-to-roll manufacturing with the product being a perovskite solar film that can be incorporated into modules. Costs associated with materials, labor, equipment depreciation are considered along with utilities determined from the fundamental engineering calculations. The results show that at very large-scale operations, the costs to produce the solar films range between \$0.04-\$0.10 per watt.

Laboratory-scale depositions use conductive annealing methods, which are not scalable, necessitating alternative methods for high-throughput PSC production. RTA combined with a rapid drying step reduced processing time from ~150 seconds to ~14 seconds for blade-coated perovskite thin films. This approach attains adequate performance, yielding a champion PCE of 14.58% for devices fabricated on flexible ITO-coated PET substrates.

Balancing solution ink formulation and scalable manufacturing is often overlooked. This study developed a mixed-cation perovskite ink with a robust coating window, utilizing compositional engineering and IPL annealing, addressing stability and manufacturability. The resulting blade-coated, flexible mixed-cation PSCs on ITO-PET substrates achieved a champion PCE of 16.7% using IPL annealing, representing one of the fastest fabrication methods for perovskite solar films.

This work contributes to broader goals towards commercialization of perovskite solar technologies. By integrating compositional engineering and post-deposition treatments, we challenge conventional approaches to PSC fabrication, paving the way for further advancements in commercial perovskite solar technologies and addressing challenges posed by high-throughput roll-to-roll manufacturing. Radiative annealing techniques, such as RTA and IPL, offer scalable, rapid, and cost-effective production of PSCs, with the potential to outpace silicon PV production and contribute to the global renewable energy landscape. Future research should focus on stability, module development, and durability testing under realistic operating conditions to accelerate commercialization of perovskite solar technologies.

TABLE OF CONTENTS

ABSTRACT.....	v
LIST OF TABLES.....	xi
LIST OF FIGURES	xii
CHAPTER 1 – Introduction	1
1.1 Global Energy Outlook.....	1
1.2 Next-Generation of Solar Energy	2
1.3 Challenges for PSCs	8
1.4 Proposed Approach.....	10
1.5 Objectives of Study.....	15
1.5.1 Specific Objectives	15
1.6 Organization of Thesis.....	16
CHAPTER 2 – Background	18
2.1 Solar cell background	18
2.2 PSC design.....	18
2.2.1 Overview.....	18
2.2.2 PSC physics	19
2.2.2 ETL	22
2.2.3 Perovskite Absorber Layer	25
2.2.4 HTL.....	31
2.3 Scalable deposition of perovskite layer	31
2.3.1 Perovskite film formation	38
2.3.2 Drying	50
2.3.3 Annealing.....	51
CHAPTER 3 – Experimental Methods	57

3.1 Techno-economic analysis, roll-to-roll production of PSCs via radiative thermal processes.....	57
3.1.1 Assumptions.....	58
3.1.2 Materials Costs.....	58
3.1.3 Equipment and Facilities Costs.....	59
3.1.4 Utility Costs.....	59
3.1.5 Labor.....	60
3.2 Fabrication of Flexible PSCs via RTA.....	60
3.2.1 Device fabrication.....	60
3.2.2 RTA of perovskite thin films.....	61
3.3 IPL-annealed mixed cation perovskites with robust coating window towards scalable manufacturing of commercial PSCs.....	61
3.3.1 Device Fabrication.....	62
3.4 JV Characterization.....	63
3.5 UV-Vis Spectrometry.....	66
3.6 X-Ray Diffraction (XRD) measurements.....	66
3.7 Scanning Electron Microscope (SEM).....	66
3.8 Nomenclature.....	66
CHAPTER 4 – Techno-economic Analysis.....	68
4.1 Introduction.....	68
4.2 Equipment Costs.....	78
4.3 Utilities.....	82
4.4 Total Costs.....	85
4.5 Conclusion.....	87
CHAPTER 5 – Fabrication of Flexible Perovskite Solar Cells via Rapid Thermal Annealing.....	89
5.1. Introduction.....	89
5.2 Process Schematic.....	90
5.3 Characterization of Rapid Thermal Annealed Perovskite Films.....	91
5.4 Utility of radiative annealing methods for low heat-tolerant flexible substrates....	93
5.5 Conclusion.....	94
CHAPTER 6 – IPL-annealed mixed-cation perovskite with robust coating window.....	95

6.1 Introduction.....	95
6.2 Process Schematic.....	99
6.3 Solubility/Evaporation	99
6.4 Transitional phase formation	102
6.5 IPL Annealing.....	105
6.6 Conclusion	112
CHAPTER 7 – Conclusions	115
CHAPTER 8 – Recommendations	118
REFERENCES.....	119
APPENDIX.....	138
CURRICULUM VITAE.....	145

LIST OF TABLES

<i>Table 1: Parameters of equations (5-7) expressed in terms of the physical parameters of the cell.....</i>	<i>21</i>
<i>Table 2: Literature survey of demonstrated scalable coating methods, accompanied by the perovskite structure, and device area.....</i>	<i>34</i>
<i>Table 3: Literature survey of commonly used perovskite solvents, highlighting their characteristics performance metrics and year when published.</i>	<i>45</i>
<i>Table 4: Examples of IPL processing of thin films used in PSCs from literature.</i>	<i>55</i>
<i>Table 5: Labor assumptions for 1 GW production line used in this techno-economic analysis</i>	<i>60</i>
<i>Table 6: Binary diffusion coefficient and vapor pressure of selected solvents used in PSC manufacturing. .</i>	<i>72</i>
<i>Table 7: Concentrations of solvent in air at 10 m/min web speed (approximately 1 GW production).</i>	<i>73</i>
<i>Table 8: IPL conditions for the different layers in a roll-to-roll processed perovskite PV used for this techno-economic analysis.....</i>	<i>78</i>
<i>Table 9: Equipment requirements for the Roll-to-Roll line per 1 GW production used in this techno-economic analysis.....</i>	<i>79</i>
<i>Table 10: Air flow heat calculation for each layer.....</i>	<i>83</i>
<i>Table 11: Comparison of energy usage per layer using IPL vs. traditional oven annealing based on the results of the techno-economic analysis.....</i>	<i>85</i>
<i>Table 12: Results from solubility tests for multiple different perovskite formulations in different solvent systems.....</i>	<i>101</i>

LIST OF FIGURES

<i>Figure 1: Spectral irradiance of the AM0 spectrum vs photon wavelength (left) and photon energy (right). Image selected from pvlighthouse.⁹</i>	3
<i>Figure 2: Maximum power conversion efficiency (PCE) (Shockley-Queisser limit) for a solar-cell operated under AM 1.5G illumination at 298.15 K, as a function of the energy bandgap. Champion PCE's of various technologies updated from 2018.¹⁰</i>	4
<i>Figure 3: The perovskite ABX₃ crystal structure.</i>	6
<i>Figure 4: The diagram presents a comprehensive approach towards commercializing perovskite solar cells. The nodes, which encompass solubility, evaporation, transitional, and annealing processes, serve as broad representations of the functions and methods relevant to perovskite thin film fabrication. The nodes, which encompass efficiency, stability/durability, manufacturing, and validation/bankability, serve as broad representations of the technical challenges for commercialization faced by perovskite photovoltaics. The materials and methods outlined at the center summarize the parameters employed to tackle both processing and technical challenges in the pursuit of commercialization. Positive relationships between nodes are represented by red lines, while negative relationships are depicted by blue lines.</i>	11
<i>Figure 5: Images of three perovskite films taken prior to annealing. The solvent systems used are A) DMF:DMSO, B)DMF:DMSO:NMP, and C) ACN:MA. D) UV-Vis absorption profiles of these three films. ACN – acetonitrile.</i>	14
<i>Figure 6: (a) 3D graphic of a PSC with electrode contacts shown for device testing. The pixel areas (silver squares on top of the black perovskite film) range from 0.1, 0.25, to 1 cm² in this work. (b) Cross-sectional schematic of a PSC, highlighting the different functional layers present in the device. The device thickness is ~500nm to 1um.</i>	19
<i>Figure 7: Energy diagram of PSCs in a p-i-n configuration (left) and a n-i-p configuration (right). Side of solar cell oriented towards the light source is indicated by the colored arrows.</i>	20
<i>Figure 8: Roll-to-roll processing concept flow schematic.</i>	32
<i>Figure 9: Certified PCE for champion PSCs and perovskite solar modules. Lab cells (~0.01 cm²); large lab cells (~1.0 cm²); lab modules (10-200 cm²); small modules (800-6500 cm²)³¹</i>	33
<i>Figure 10: Schematic of blade coating thin films from a side angle, displaying the precursor solution meniscus between blade and substrate.</i>	37
<i>Figure 11: Schematic of slot die coating thin films from a side angle, displaying the coating bead formation.</i>	38
<i>Figure 12: Plot of the Gibbs free energy</i>	39
<i>Figure 13: Schematic illustration of diffusion layer structure neat the surface of a nanocrystal (left) and plot for the monomer concentration as a function of distance x (right). Shaded area represents the diffusion layer.</i>	40
<i>Figure 14: LaMer diagram depicting three stages in the formation of uniform colloidal particles.</i>	42
<i>Figure 15: Plot of vapor pressure and Donor number for commonly used perovskite solvents. Plot credit: Deng et al.¹⁷⁶</i>	44
<i>Figure 16: Measured film thickness h as a function of deposition speed. Two regimes are identified as a function of v *: evaporation and Landau-Levich.¹⁵²</i>	47
<i>Figure 17: Illustration of forced laminar air flow drying of a perovskite thin film.</i>	51

Figure 18: (top) Emission profile of the IPL lamp showing intensity as a function of wavelength from the Xenon source material. (bottom) Illustration of an absorption profile of a visible light absorbing film, with the shaded region highlighting the amount of energy absorbed by the film.53

Figure 19: Schematic of the processing of the individual layers of the perovskite device by slot die deposition, air knife drying and IPL annealing. Flexible plastic is depicted as the substrate for the devices. The fabrication process for a single layer, from start to finish, has been demonstrated in a 2 m length of the process path. 54

Figure 20: An example of a JV Curve for a solar cell device under test, highlighting the relevant parameters of J_{sc} , V_{oc} , FF, and PCE. Device schematic in the upper right corner represents a cross-sectional perovskite solar cell under illumination. 64

Figure 21: Flow chart explaining the overall methodology of the techno-economic analysis. The process under investigation includes the deposition, drying and post-processing using IPL of the four layers (SnO_2 , perovskite, NiO and Cu). A fundamental engineering analysis of each process informs the design of the equipment, utilities and labor. All of these including the material inputs are considered for the overall roll-up of the cost of goods sold..... 69

Figure 22: The drying time for a solvent thickness of 10 mm for DMF and ACN is shown as a function of air velocity over the film surface and for two air temperatures. This relationship is used to estimate drying for different solvent systems based on their physical properties..... 74

Figure 23: Comparison of thermal response to IPL intensity and pulse duration for two substrates. Solid lines denote temperature for the perovskite film and dashed lines for temperature in the substrate, either glass or PET. The legend denotes high (E_{high}) or low (E_{low}) pulse intensity and pulse length of 2 ms or 0.5 ms being applied. 76

Figure 24: Manufacturing costs of PSCs based on annual output. The curves bound the upper and lower cost estimates using a modest and conservative learning rates applied to the ITO coated PET. The bars on the average curve includes 95% confidence intervals from the Monte-Carlo analysis. The lowest curve shows the costs associated with processing (equipment, labor, utilities, & depreciation). (inset) Contribution to overall costs at 2 GW production using the average learning rate applied to the ITO coated PET..... 87

Figure 25: Schematic illustrating procedures to synthesize perovskite thin films using both conductive annealing and RTA. Images of perovskite thin film post-conductive annealing and post-RTA annealing are included. 90

Figure 26: (A) SEM image (B) XRD pattern of perovskite film and (C) JV curve of champion device annealed with RTA. 91

Figure 27: (A) Temperature profile tracking temperature of both PET and PVSK on a R2R line annealed by either conduction or RTA. (B) Strain vs time tracking the strain in both PET and ITO on a R2R line annealed by either conduction or RTA. Critical tensile strain for RTA is ~2%. 93

Figure 28: Venn diagram to visualize the approach to designing high-throughput, functional perovskite solar films. Categories of solubility/evaporation of the ink, transitional phase formation, and IPL annealing all are interconnected in the manufacturing process to realize the solar technology. 97

Figure 29: (a) Schematic of the projected in-line roll-to-roll manufacturing process. Perovskite thin film fabrication conducted in 3 steps: Deposition, Drying, and Annealing. (b-f) Highlights issues with commonly used DMF:DMSO ink formulations for high-throughput, mixed cation perovskite deposition. Analytical tools (XRD, UV-Vis, optical and SEM images) utilized to monitor progress through perovskite film deposition that results in non-uniform, inefficient perovskite films. (g-k) Highlights advantages of optimized ACN:2-ME w/ NMP, PEAI, CH_2I_2 ink formulation for high-throughput, mixed cation perovskite deposition. Analytical tools (XRD, UV-Vis, optical and SEM images) utilized to monitor progress through perovskite film deposition that result in uniform, efficient perovskite films. 99

Figure 30: (a) JV performance data of the champion 6% NMP hotplate-annealed sample, light and dark currents. (b) Device performance statistics of short circuit current density (J_{sc}), open circuit voltage (V_{oc}), fill

<i>factor (FF), and power conversion efficiency (PCE) at different NMP concentrations in ACN:2-ME. Highest efficiencies achieved when NMP concentration reaches 6%. Each condition tested >15 devices.</i>	<i>104</i>
<i>Figure 31: Images of $FA_{0.86}MA_{0.14}Pb(I_{0.95}Br_{0.05})_3$ and $MAPb(I_{0.95}Br_{0.05})_3$ at different times during hotplate annealing. A plot of color conversion time vs ratio of FA to MA.</i>	<i>105</i>
<i>Figure 32: Comparison of performance metrics for Hotplate- and IPL-annealed PSCs. Pixel size is 0.125 cm^2.</i>	<i>107</i>
<i>Figure 33: (a-d) Optical images highlight qualitative approach to observe pros/cons of IPL-annealed perovskite solar films. (e) XRD patterns of neat, hotplate-annealed, and three different IPL conditions at increasing voltages. This highlights the flexibility of IPL parameter space to be tailored for a given application.</i>	<i>108</i>
<i>Figure 34: (a) SEM image of the neat perovskite film after IPL annealing. (b) SEM image of the perovskite film with CH_2I_2 additive after IPL annealing. (c) XRD pattern of the resulting perovskite film after IPL annealing with the CH_2I_2 additive and without the CH_2I_2 additive (Neat).</i>	<i>110</i>
<i>Figure 35: (a) JV performance data of the champion IPL-annealed PSC using the optimized ink formulation, light and dark currents. Optimized ink formulation: $FA_{0.4}MA_{0.6}PbI_{0.95}Br_{0.05}$ in 0.6 ACN:0.4 2-ME (v:v) with 6% NMP (mol%), 3 mg/mL PEAI, 38 $\mu\text{L/mL}$ CH_2I_2. (b) Comparison of the performance data of PSCs with Hotplate-annealed perovskite layer, IPL-annealed perovskite layer, and IPL-annealed perovskite and SnO_2 layers. IPL-annealed samples match hotplate-annealed samples and are processed in <30 seconds. The IPL parameters used for IPL-annealed samples were 1700V, 500 μsec duration, 500 msec delay, 3 pulses.</i>	<i>112</i>

CHAPTER 1 – INTRODUCTION

1.1 Global Energy Outlook

The global energy outlook is a complex and rapidly changing landscape, with a range of factors influencing the production, consumption, and distribution of energy around the world. The fragility and unsustainability of our current energy system was highlighted by recent geopolitical events that had a significant impact on global energy markets.¹ Additionally, the international community is falling well short of the Paris Agreement goals with projections of a 2.8°C temperature rise by the end of the century, with no credible pathway to 1.5°C.² The Solar Energy Industries Association projects that the industry is expected to double the amount of US solar installations over the next 5 years thanks to strong federal policies, rapidly declining costs, and increasing demand across the private and public sector for clean electricity.³ Momentum is building towards a new energy economy as security, climate, and economic priorities are increasingly aligned, leading to advancements in both policy and technology.

Renewable energy's share of US electricity generation rose to 23% from 21% from January to August 2021.⁴ While significant, Deloitte forecasts stronger growth in renewables in 2023 due to cost competitiveness, federal and state clean energy policies, utility decarbonization, corporate renewable procurement, residential solar demand, and private investment.⁵ Renewables are set to account for almost 95% of the increase in global power capacity through 2026, with solar PV alone providing more than half.⁶

More than a decade-long price reduction, driven by increasing scale and technological advances, created a scenario where wind and solar are the cheapest energy sources for power generation in most areas. Shortages in the supply chain, limited transmission capacity, and interconnection delays have caused temporary setbacks, increasing the need for further technological advancements to diversify and mitigate vulnerabilities as we transition to clean energy.

Among all renewable energy sources, solar power has experienced the most substantial increase, with an average annual growth rate of 33% over the past 10 years.³ Solar has added the most generating capacity to the grid for three consecutive years and is expected to install nearly 200 gigawatts (GW) of new U.S. solar capacity over the next five years.³ The majority of this growth is dominated by crystalline silicon (c-Si) technology, leading to concentrated supply chains and potential impacts from instability in critical mineral prices, specifically silver and silicon.⁷ The need for solar diversification has become increasingly important to enable society to cope with disruptions to any one specific solar technology. Consequently, next-generation solar technologies are becoming more crucial, with investment in potential alternatives like thin-film photovoltaics (PV), tandem devices, or concentrated solar power gaining more attention.

1.2 Next-Generation of Solar Energy

Solar energy is the most abundant energy resource on earth, with a constant supply of 173,000 TW, far exceeding the world's total energy consumption by more than 10,000 times.⁸ Sunlight, a form of electromagnetic radiation, is composed of a spectrum

of wavelengths that peak within the visible light region of the electromagnetic spectrum. The Planck relation shows that energy and wavelength are inversely related, as shown below.

$$E = \frac{hc}{\lambda} \tag{1}$$

The critical characteristics that determine how sunlight will interact with a PV cell are the spectral content of the incident light, radiant power density, and angle at which it strikes the cell. The spectral irradiance of solar radiation follows typical blackbody radiation, shown for both wavelength and photon energy in figure 1. The non-uniformity of spectral irradiance is a critical factor in the evaluation of potential solar cell materials, essential for the design of next-generation solar cells.

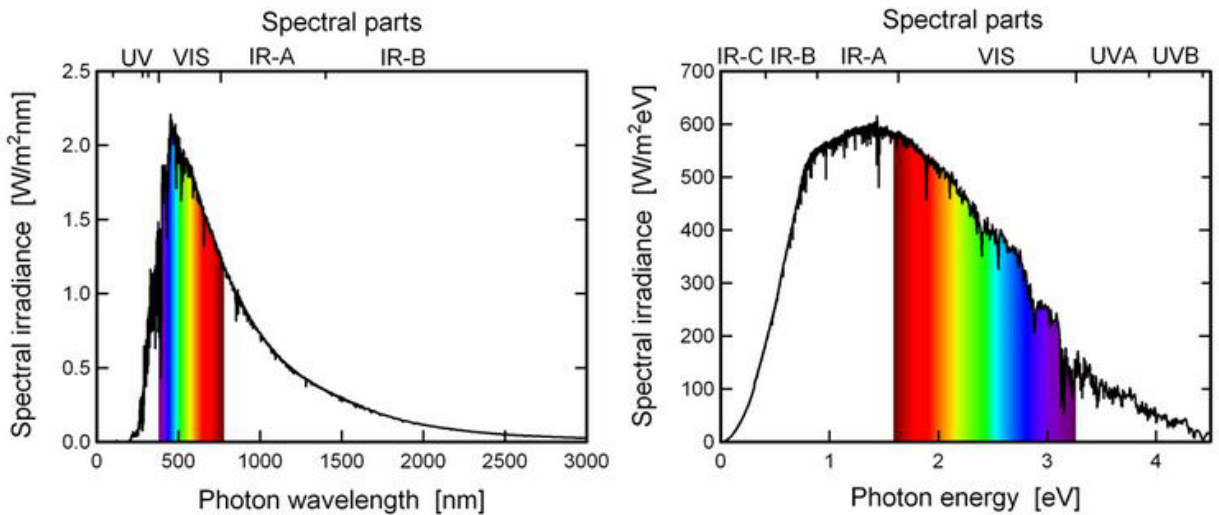


Figure 1: Spectral irradiance of the AM0 spectrum vs photon wavelength (left) and photon energy (right). Image selected from pvlighthouse.⁹

The principles of solid-state semiconductors can be used to explain the fundamental mechanism of solar cells, known as the PV effect. When photons of sunlight, with energy greater than the band gap of the semiconductor material, strike a

solar cell, they excite electrons in the valence band to the conduction band, forming an electron-hole pair. These excited electrons are collected by an external circuit, generating electricity. In solar cells, the band gap of a semiconductor material represents a crucial physical property, as it not only determines the maximum theoretical voltage that can be extracted but also dictates the wavelengths of light that can be absorbed. The significance of the band gap is highlighted through the Shockley-Queisser limit, which illustrates how the maximum theoretical efficiency of a single-junction solar cell can be computed from the band gap of the solar cell material, as depicted in figure 2. Additionally, whether the material has a direct or indirect band gap affects the efficiency of the PV process for that material.

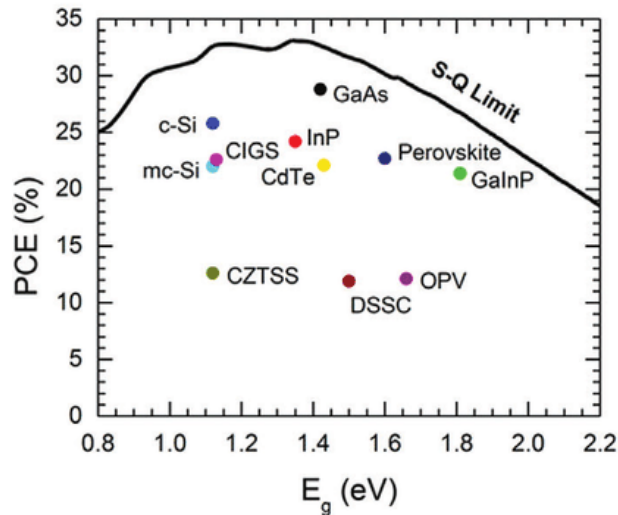


Figure 2: Maximum power conversion efficiency (PCE) (Shockley-Queisser limit) for a solar-cell operated under AM 1.5G illumination at 298.15 K, as a function of the energy bandgap. Champion PCE's of various technologies updated from 2018. ¹⁰

Currently, c-Si solar cells account for 90% of the global production capacity and are the most well-established PV technology, with a history of research spanning over 60 years.¹¹ Silicon PVs have a proven track record of reliability, non-toxicity, and efficiency,

making them a trusted and cost-effective option for solar energy production. However, silicon does not have optimal material properties for PVs. The band gap of silicon, 1.12 eV, falls short of the optimal value of 1.4 eV, according to the Shockley-Queisser limit. Furthermore, as an indirect band gap material, silicon exhibits a low absorption coefficient, necessitating the implementation of light-trapping techniques or layer thicknesses greater than 100 μm .¹¹

Clearly, next-generation solar technologies are necessary to address the shortcomings of current silicon technology and provide alternative solutions for a more resilient energy economy. PSCs have shown remarkable progress in recent years and are a promising class of materials for next-generation solar cells. They have the potential for high efficiencies and cost-effectiveness compared to conventional c-Si solar technologies. The crystal structure of perovskites (for which they get their nickname), ABX_3 , features an organic cation (A), a divalent metal ion (B), and halide ions (X), shown in figure 3. This material is known for its high defect tolerance, tunable band gaps, high absorption coefficients, small exciton binding energies, long charge diffusion lengths, high carrier mobilities, and ultra-low trap densities.¹²⁻¹⁶

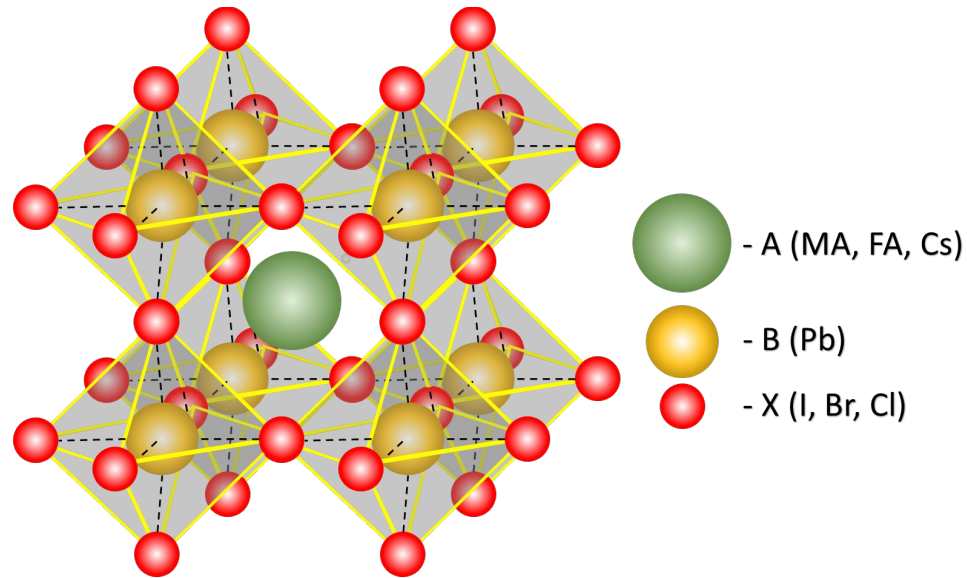


Figure 3: The perovskite ABX_3 crystal structure.

Perovskite is a direct band gap material, meaning that the Brillouin zones for valence and conduction bands are in alignment. This results in higher absorption coefficients because electrons can shift from the highest-energy state in the valence band to the lowest-energy state in the conduction band without a change in crystal momentum. The implications of this for the overall solar cell are that the perovskite absorber material can be <500 nm in thickness and absorb the entirety of the solar spectrum. By comparison, silicon being an indirect band gap material requires much thicker films (order of microns) to accomplish the same absorption. This limits silicon solar panels to rigid architectures and that are plagued by high weights, resulting in excessive soft costs. Perovskites being defect tolerant and thinner have applications for flexible architectures that open up a lot of potential end uses (building integration, wearables, etc.), cost, and manufacturing benefits. The intrinsic band gap alignment is one example of how perovskites are more ideal PV materials than silicon.

Solution phase deposition in the manufacture of perovskite solar cells (PSCs) enables simpler production methods, leading to increased deployment of solar energy systems, surpassing the limitations of silicon-based systems. The possibility of large-scale solar deployment, on the scale of terawatts, through roll-to-roll manufacturing provides a credible roadmap towards this goal. In addition to high production volumes, the diverse potential applications of solution phase deposition offer exciting prospects.

PSCs are annealed at much lower temperatures than their silicon counterparts. As such, they are compatible for roll-to-roll manufacturing on flexible plastic substrates as the temperatures required to anneal different components do not approach glass-transition temperatures for the substrate (that would be under tension). When considering levelized-cost-of-energy (LCOE) for different solar technologies, it is important to consider the amount of energy/electricity required to process the solar cell. This is an area where perovskite has a significant advantage over c-Si, in that c-Si requires ultra-high purity Si achieved in energy intensive electric-arc furnaces around 6,000°C.

Touched on previously, but the environmental impacts of the mining and energy consumed to process a solar material are extra significant for an industry that relies on the image of tackling climate change. Mining silicon is very harmful to the environment and the energy intensive processing results in life cycle greenhouse gas emissions of 45 g CO₂-equivalent per kWh for c-Si PV.¹⁷ Perovskites are expected to produce much less greenhouse gas emissions because of the processing and abundance of starting materials.¹⁷

The potential for PVs to become a primary global power source suggests that current PV market resources must be sufficient to meet future demand. To reach 12.5 TW PV capacity by leading PV technologies, current production rates of tellurium (cadmium telluride-CdTe), gallium (gallium arsenide-GaAs), indium (copper indium gallium selenide-CIGS), silicon (c-Si), and lead (perovskite) would need to be sustained for 1000 years, 500 years, 400 years, 3 years, and a few days, respectively.¹⁸

1.3 Challenges for PSCs

Despite the many advantages of PSCs, there are several challenges that need to be addressed before they can be widely adopted. For perovskite PV technologies to be commercially competitive, their LCOE must be competitive with the LCOE of incumbent technologies at the time they are ready to be deployed. This will be difficult as year-over-year cost reductions in silicon and CdTe PV modules are projected to continue through the next decade and beyond.¹⁹

As LCOE considers the lifetime of the solar cell, for perovskite PV to be cost-competitive with silicon technologies and approach the Solar Energy Technologies Office's (SETO) 2030 goals of \$0.02/kWh, perovskite will have to last at least 20 years in the field.²⁰ Enabling this lifetime requires improving perovskites' ability to withstand various environmental conditions. To this end, much research has been focused on understanding and mitigating the chemical reactions of the perovskite material with oxygen and/or moisture²¹, thermal degradation^{22, 23}, potential induced degradation^{24, 25}, reverse-bias degradation²⁶, electrochemical corrosion between perovskite and metal contacts^{27, 28}, chemical corrosion between perovskite and encapsulation filler sheets, and

mechanical delamination and cracking of the perovskite layer upon thermal cycling, which happens due to mismatch in the coefficient of thermal expansion between perovskite and substrates^{29, 30}. The breadth of different degradation modes presents a formidable challenge, and without a satisfactory resolution, will obstruct any aspirations to commercialize this technology.

While there is no shortage of small area ($\leq 0.1 \text{ cm}^2$) demonstrations with high PCE, efficiencies of large-area perovskite cells ($>10 \text{ cm}^2$) are significantly lower. For most types of solar cell technologies, the absolute PCE value decreases by $\sim 0.8\%$ when the device area increases by an order of magnitude; however, the PCE loss of perovskite solar modules far exceeds this rate due to non-uniform deposition of all functional layers, with perovskite being the most important and challenging.³¹⁻³⁴ Currently, methods for non-scalable, high efficiency PSC deposition are failing to achieve a level of uniformity sufficient enough to maintain efficiencies over large-areas. Roll-to-roll manufacturing is the most feasible and economical approach to large-scale PSC production. Innovative applications of both classical and novel manufacturing methods that align with roll-to-roll manufacturing are required to solve this challenge.

Related to process scalability, PSCs must address barriers related to process control and manufacturing yield that are often underappreciated. As the technology transitions to large production capacities, it is imperative to minimize the distribution in PSC efficiencies. Currently, PCE can be impacted by minute fluctuations in ambient temperature during film deposition, minute changes in precursor molar ratios, and/or ink storage time.³⁵⁻³⁸ Characterization of process robustness must be tested through structured

experimentation, utilizing statistical process control, to ensure changes in performance are significant. The development of processes that, when scaled up, are inherently easier to control is a priority.

1.4 Proposed Approach

PSC technology presents a promising alternative to silicon-based PVs, yet the challenges of stability, module efficiency, and scalability remain significant obstacles to its commercialization. The drive to attain optimal efficiency has resulted in substantial advancements in PSC technology, as PCEs now match those of c-Si cells. However, it is important to note that while these solutions have made progress in PSC commercialization, they often partially resolve issues or create new challenges that must be addressed. To proactively address and deter commercialization challenges, the field of PSCs needs a comprehensive approach to consider the interplay between compositional engineering, thin-film deposition, drying, and annealing processes, and their impact on PSC efficiency, durability, scalability, and bankability. The proposed approach of this study is detailed in figure 4.

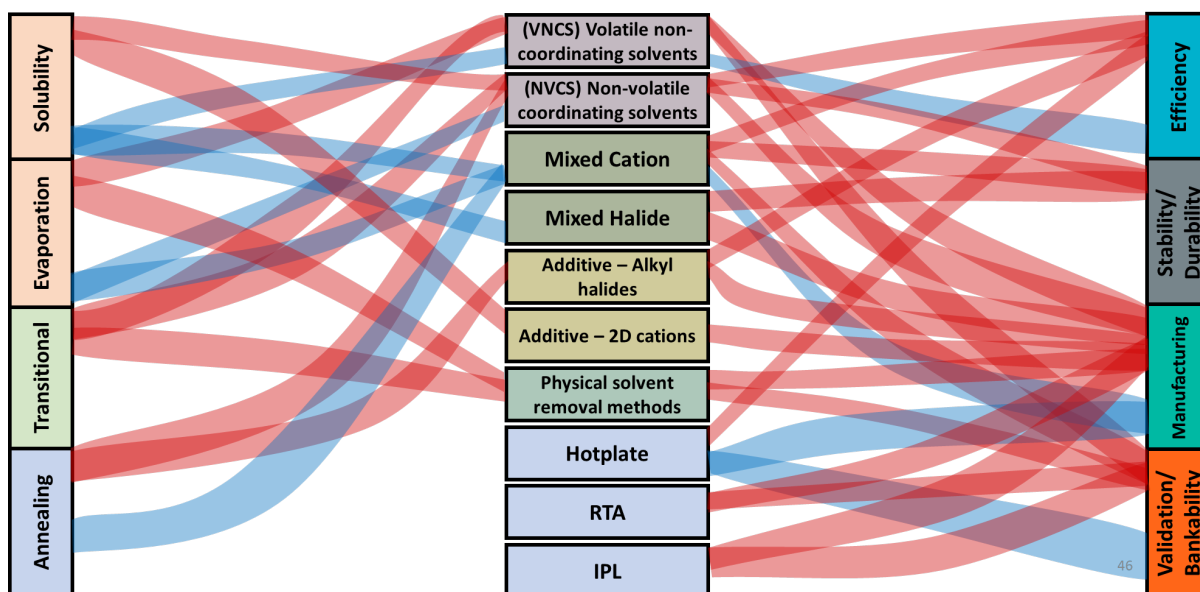


Figure 4: The diagram presents a comprehensive approach towards commercializing perovskite solar cells. The nodes, which encompass solubility, evaporation, transitional, and annealing processes, serve as broad representations of the functions and methods relevant to perovskite thin film fabrication. The nodes, which encompass efficiency, stability/durability, manufacturing, and validation/bankability, serve as broad representations of the technical challenges for commercialization faced by perovskite photovoltaics. The materials and methods outlined at the center summarize the parameters employed to tackle both processing and technical challenges in the pursuit of commercialization. Positive relationships between nodes are represented by red lines, while negative relationships are depicted by blue lines.

The aim of this study is to explore potential solutions to overcome the scalability and cost limitations of PSCs. For most solar cell technologies, the PCE decreases as the device area increases; however, the rate of PCE loss for perovskite solar modules far exceeds the competition, due to non-uniformity in the functional layers. A primary reason for this non-uniformity is the inability for laboratory-scale fabrication techniques to scale. This study investigates alternatives that enhance the feasibility and scalability of solution-phase PSC by evaluating options that effectively align with roll-to-roll manufacturing methods, considered to be the most feasible and economical approach for large-scale PSC production.

Annealing is a critical aspect of PSC fabrication, and its successful completion has largely relied on the use of hotplate in laboratory-scale applications. The lack of an analogous technique to hotplate annealing for roll-to-roll applications has hindered widespread implementation of roll-to-roll PSC manufacturing. Many existing annealing methods either necessitate the use of ovens with impractically long dimensions or demand temperatures that exceed operational stability, highlighting the necessity for alternative approaches. Radiative annealing techniques, including intense pulsed light (IPL) and rapid thermal annealing (RTA), have exhibited the potential to reduce processing times by an order of magnitude. These techniques exploit the physical properties of materials, primarily light absorption, to minimize heat transfer to temperature-sensitive components. For flexible PSC applications, IPL distinguishes itself with μsec pulse durations and the compatibility of the Xenon flash source with temperature sensitive components in PSCs. Building upon the extensive existing knowledge on perovskite thin film formation, this study aims to examine the interactions between radiative annealing techniques and perovskite thin films as a solution to scale PSC manufacturing.

In the context of roll-to-roll processing, the time available for nucleation and crystal growth is limited, creating a situation where commercial viability and perovskite quality can be mutually exclusive. Additionally, in the context of radiative annealing, it is necessary for the perovskite film to have light absorption properties to facilitate effective heat transfer. These requirements are often overlooked in other annealing applications. Integration of roll-to-roll processing and radiative annealing techniques, requires re-

optimizing and tailoring perovskite inks for the annealing process, as existing ink formulations in literature are not satisfactory for this application.

For IPL compatibility, an idealized ink would have strong visible light absorption across most to all visible wavelengths. As shown in figure 5, our preliminary research has revealed that the absorption profile of perovskite transitional phases can be adjusted. Annealing is typically performed after the solvent removal step in perovskite fabrication, and it is reasonable to attribute the observed changes in the absorption profile to the presence of non-volatile coordinating solvents (NVCS), the composition of the perovskite, and any non-volatile additives in the precursor ink. Therefore, qualitative and spectroscopic techniques were used when considering components effect on absorption for the precursor ink. Crystallographic, spectroscopic, and photovoltaic measurements were collected post-annealing to ensure new components did not adversely affect device performance.

In high-throughput roll-to-roll manufacturing, the size of the processing/coating window has direct correlations to overall yields and process robustness, both reducing overall costs. As the process transitions to industrial scale, the physical properties of the precursor become increasingly significant in determining the outcome of film formation. Intrinsic properties of solvents were used to regulate both the evaporation/nucleation rate (vapor pressure) and stabilize the transitional phase (Donor number). Ultimately, solvent systems were created using volatile, non-coordinating solvents (VNCS) and NCVS to expand processing windows, as confirmed by crystallographic, and photovoltaic measurements.

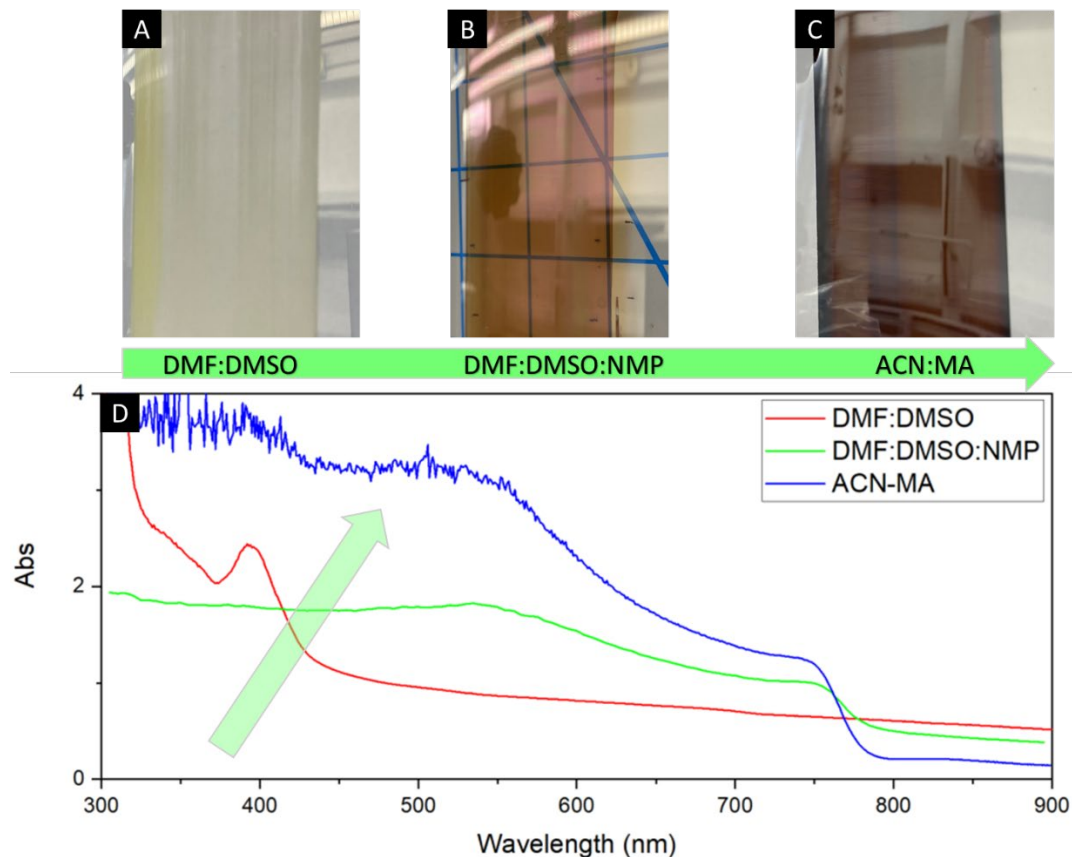


Figure 5: Images of three perovskite films taken prior to annealing. The solvent systems used are A) DMF:DMSO, B) DMF:DMSO:NMP, and C) ACN:MA. D) UV-Vis absorption profiles of these three films. ACN – acetonitrile.

Just as the properties of perovskite film deposition can be adjusted by modifications to precursors, IPL parameters can also be adjusted to match the process. IPL delivers high-energy microsecond pulses of light from a Xenon flash lamp to a large processing area, capable of heating photosensitive materials to temperatures exceeding several hundred degrees Celsius.[32, 33] By controlling the intensity, number of pulses, pulse duration, and delay between pulses, the nature of the interaction between IPL and the perovskite film can be altered. The combination of qualitative, spectroscopic, crystallographic, and photovoltaic analytical techniques were utilized to iteratively optimize IPL parameters for a given precursor formulation.

1.5 Objectives of Study

The objective of this research is to address the limitations in terms of scalability and cost for PSCs and evaluate possible solutions. The commercialization of PSCs has been hindered by a lack of effective transfer of laboratory-scale fabrication techniques to industrial-scale production. One promising approach is the integration of roll-to-roll processing and IPL. To achieve this goal, it is essential to optimize the perovskite ink chemistry, taking into account its composition, additives, solvent systems, and their impact on PSC efficiency, durability, scalability, and bankability. The proposed methodology involves modifying the precursor chemistry and investigating solvents and additives to maintain the optoelectronic properties of the perovskite film after IPL annealing. The efficiency of the PSCs will be confirmed by evaluating the PCE and its influence on commercial prospects. The ultimate goal is to implement the optimized IPL parameters in a rapid manufacturing process and continuously refine the technology through iteration.

1.5.1 Specific Objectives

- a. Conduct cost analysis for integrating IPL annealing into roll-to-roll manufacturing processes of PSCs to evaluate its economic feasibility for large scale industrial production.
- b. Utilize volatile solvents to achieve rapid supersaturation promoting rapid nucleation to form compact and uniform perovskite thin films.
- c. Evaluate high donor number, low vapor pressure solvents as transitional phase stabilizers to understand their role in expanding the processing window for IPL annealing, making thin film deposition more robust.
- d. Explore additives with functionality for IPL that improve the overall crystallinity, morphology or optoelectronic properties of a perovskite film.

- e. Transition to perovskite compositions with higher stability than conventional perovskite compositions and study the changes to perovskite film formation induced by the different constituents.
- f. Develop a comprehensive approach to experimentally study perovskite thin film coating to provide a roadmap for the development of future commercial PSCs.
- g. Optimize IPL parameters for compatibility and increased throughput of PSCs utilizing the improved ink chemistry.

1.6 Organization of Thesis

Chapter 1 aims to offer a comprehensive overview of the prevailing status of renewable energy, with a particular focus on solar energy implementation. This section will analyze the necessary advancements for the next generation of solar technologies to rival existing silicon-based solar technologies. The chapter will then delve into the obstacles hindering the commercialization of perovskite solar technologies and their ability to meet the aforementioned milestones. The study will present a methodical approach to overcoming the challenges posed to perovskite solar and clearly outline the research objectives associated with this endeavor.

Chapter 2 presents a thorough examination of the underlying principles of solar cell operation, with a specific focus on PSCs. The literature review also encompasses the key aspects of thin film deposition parameters that are crucial for the widespread implementation of perovskite thin films.

Chapter 3 outlines the techniques utilized for the deposition of perovskite films and the assembly of the solar cell. This chapter also encompasses the various characterization methods employed to study and evaluate the properties of these materials.

Chapter 4 showcases the findings from a technoeconomic analysis of roll-to-roll manufactured PSCs that have undergone IPL. The results demonstrate the cost advantages and improved productivity attainable through the implementation of innovative annealing methods.

Chapter 5 presents the results of annealing perovskite thin films through RTA techniques. The section also examines the benefits of radiative annealing for its suitability with temperature-sensitive substrates in roll-to-roll production lines.

Chapter 6 outlines a comprehensive and integrated approach to the processing of perovskite thin films through IPL for large-scale production. This chapter discusses the outcomes of this study in detail.

The conclusions and recommendations from this study are included in Chapters 7 and 8, respectively.

CHAPTER 2 – BACKGROUND

2.1 Solar cell background

The first practical solar cell was demonstrated in the 1950s after the advent of semiconductor physics for the transistor. Research and development of PVs received its first major boost from the space industry in the 1960s. The need for a power supply apart from grid power became an interesting scientific variation to rapidly expanding silicon transistor development. The oil crisis in 1970 created an incentive to investigate terrestrial solar power, allowing it to enter the power generating sector. Research into solar cells continued through the 1980s with the 20% milestone achieved in 1985. The growth has continued over the decades where it now can provide substantial fractions of the grid electricity.

2.2 PSC design

2.2.1 Overview

Initially, PSCs evolved as a variant of dye-sensitized solar cells (DSSCs), which led to a lot of similarities in the device structures with the first recorded efficiency in 2009.^{39, 40} PSCs are highly efficient thin film PV devices capable of converting sunlight into electricity with PCEs that rival those of conventional c-Si cells, typically exceeding 25%.⁴¹ They are fabricated through the deposition of thin layers of materials onto a substrate, such as glass or plastic, which has been coated with a transparent conductive oxide (TCO), such as fluorine-doped tin oxide (FTO) or indium-doped tin oxide (ITO).

The deposition process can be performed using various techniques, including solution processing methods such as spin-coating, doctor blade coating, or dip-coating, or vapor deposition techniques like thermal evaporation or chemical vapor deposition. A 3D and cross-sectional representation of a PSC fabricated at our University is depicted in figure 6.

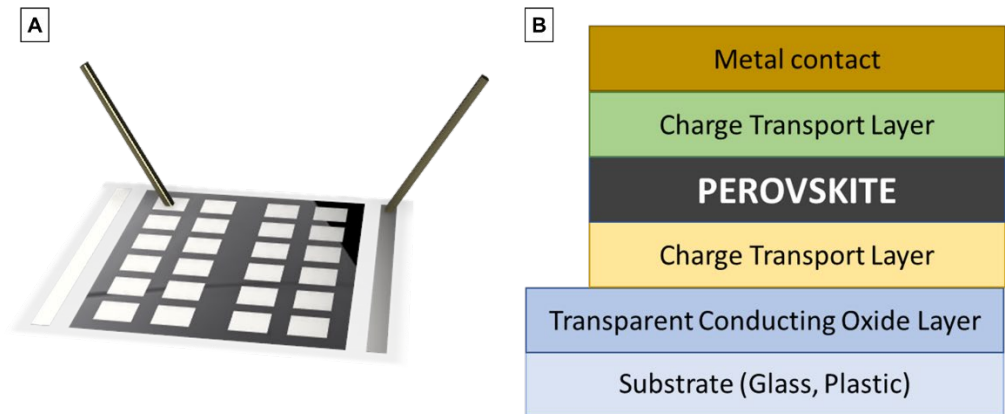


Figure 6: (a) 3D graphic of a PSC with electrode contacts shown for device testing. The pixel areas (silver squares on top of the black perovskite film) range from 0.1, 0.25, to 1 cm^2 in this work. (b) Cross-sectional schematic of a PSC, highlighting the different functional layers present in the device. The device thickness is $\sim 500\text{nm}$ to $1\mu\text{m}$.

2.2.2 PSC physics

Conventional c-Si solar cells are based around the p-n junction of solid-state semiconductors. PSCs are different in that they operate on a p-i-n architecture, where the perovskite absorber layer is sandwiched between p- and n-type materials. PSCs can be defined as either p-i-n architectures or n-i-p architectures, depending on whether light enters into the PV cell through the hole transport layer (HTL) or electron transport layer (ETL), respectively. The process of sunlight striking the perovskite solar material, excites an electron and creates an electron-hole pair. The high dielectric constant of perovskites allows photogenerated excitons to dissociate immediately into free carriers where

electrons and holes drift and diffuse through the absorber and transparent layers to be extracted at the contacts.

It has been argued that the absorber layer in high efficiency cells is essentially intrinsic, which is the basis for the “i” term in the “p-i-n” architecture.⁴² Analytical models can be developed by solving the steady-state electron and hole continuity equations within the absorber, as follows:

$$D \frac{\delta^2 n(x)}{\delta x^2} + \mu E(x) \frac{\delta n(x)}{\delta x} + G(x) - R(x) = 0 \quad (2)$$

$$D \frac{\delta^2 p(x)}{\delta x^2} - \mu E(x) \frac{\delta p(x)}{\delta x} + G(x) - R(x) = 0 \quad (3)$$

where, n and p represent the electron and hole concentration, respectively, D and μ are the diffusion coefficient and mobility, respectively, $E(x)$ is the position-dependent electric field within the absorber layer, $G(x)$ represents the position-dependent photogeneration, and $R(x)$ represents carrier recombination within the absorber layer. Extraordinarily long diffusion lengths in perovskite ensure that $R(x)$ is negligible.

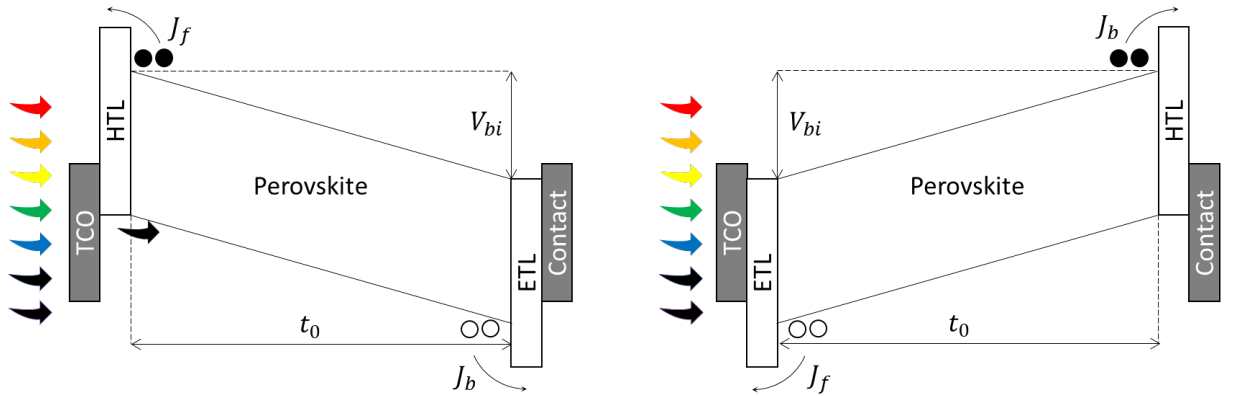


Figure 7: Energy diagram of PSCs in a p-i-n configuration (left) and a n-i-p configuration (right). Side of solar cell oriented towards the light source is indicated by the colored arrows.

Figure 7 highlights the intrinsic nature of the solar cell as $E(x)$ is linear, in the absence of doping or trap states. The generated profile in the absorber layer can be approximated as

$$G_{max} = \int_0^{\infty} G_{eff} e^{-x/\lambda_{ave}} dx = G_{eff} \lambda_{ave} \quad (4)$$

where G_{eff} and λ_{ave} are material specific constants averaged over the solar spectrum.

Equations (3) and (4) can be solved analytically to derive the complete current-voltage characteristics for both p-i-n and n-i-p architectures as shown below in table 1 and equations (5-7):

$$J_{dark} = (\alpha_f * J_{f0} + \alpha_b * J_{b0}) (e^{\frac{qV}{kT}} - 1) \quad (5)$$

$$J_{photo} = qG_{max} (A - B e^{-\frac{t_0}{\lambda_{ave}}}) \quad (6)$$

$$J_{light} = J_{dark} + J_{photo} \quad (7)$$

Table 1: Parameters of equations (5-7) expressed in terms of the physical parameters of the cell.

Variable	Definition
$\frac{1}{\alpha_f}$	$\frac{e^{\frac{q(V-V_{bi})}{kT}} - 1}{\frac{q(V-V_{bi})}{kT}} + \frac{D}{t_0 * S_f}$
$\frac{1}{\alpha_b}$	$\frac{e^{\frac{q(V-V_{bi})}{kT}} - 1}{\frac{q(V-V_{bi})}{kT}} + \frac{D}{t_0 * S_b}$
A	$\alpha_f * \left(\frac{(1 - e^{-\frac{q(V-V_{bi})}{kT} - \frac{t_0}{\lambda_{ave}}})}{\frac{q(V-V_{bi})}{kT} - \frac{t_0}{\lambda_{ave}}} - \frac{D}{t_0 * S_f} \right)$
B	$\alpha_b * \left(\frac{(1 - e^{-\frac{q(V-V_{bi})}{kT} - \frac{t_0}{\lambda_{ave}}})}{\frac{q(V-V_{bi})}{kT} - \frac{t_0}{\lambda_{ave}}} - \frac{D}{t_0 * S_b} \right)$

The parameters summarized in table 1 are functions of the thickness of the absorber layer (t_0), the dark diode current recombining at both transport layers (J_{f0} , J_{b0}), the built-in potential across the absorber layer (V_{bi}), the diffusion coefficient (D), the effective surface recombination velocity at perovskite/charge transport layer (CTL) interfaces (s_b , s_f), and the maximum absorption (G_{max}).

This model describes the basic physics of a p-i-n solar cell under operation. Advancements in organic and DSSCs have benefitted the field of PSCs through the development of a diverse set of PSC-compatible CTLs. The identity of the CTLs has implications across all metrics of PSC device performance. A few other variations that change the model include the composition of the perovskite absorber, quality of the perovskite absorber, and additives incorporated into the precursor ink. The perovskite material possesses a high level of tolerance towards defects, enabling its utilization with a diverse range of A-site, B-site, and X-site compositions, phase stabilization, and dimensionalities (2D/3D) that can impact device physics. This model can be used to interpret PSC operation and obtain physical parameters of the cell to help expedite characterization and optimization of the components.

2.2.2 ETL

Ideal ETLs must combine good electrical conductivity, suitable energy levels, low surface defect density, high transmittance, pinhole-free morphology, as well as good optical and thermal stability. In typical PSCs, any work function difference between ETL and perovskite will lead to a flow of electrons from the low work function material to the high work function material. In thermal equilibrium, a space charge layer will form across the interface.⁴³ The resulting built-in electric field in the depletion region can help

extract electrons into the ETL, suppress back transfer of electrons from ETLs to the perovskite, and further assist in charge separation close to the interface. Ideally, the space charge layer would extend across the entirety of the perovskite, however, the depletion width (x_0) at the ETL/perovskite heterojunction is generally expressed as:

$$x_n = \sqrt{\frac{2\varepsilon_n\varepsilon_p n_p V_0}{en_p(\varepsilon_n n_n + \varepsilon_p n_p)}} \quad (8)$$

$$x_p = \sqrt{\frac{2\varepsilon_n\varepsilon_p n_n V_0}{en_p(\varepsilon_n n_n + \varepsilon_p n_p)}} \quad (9)$$

$$x_0 = x_n + x_p = \sqrt{\frac{2\varepsilon_n\varepsilon_p V_0 (n_n + n_p)^2}{en_n n_p (\varepsilon_n n_n + \varepsilon_p n_p)}} \quad (10)$$

where x_n and x_p are the depletion widths in ETL and perovskite, respectively. V_0 is the difference in Fermi levels, ε_n and ε_p stand for the static permittivity of ETL and perovskite, respectively, e

is the elementary charge, n_n and n_p refer to the doping density of ETL and perovskite, respectively. The impact of the ETL on the space charge layer in combination with a lower number of electrons (in comparison to TCO), deep valence band of ETL to block holes, and prevent shorting of the HTL or metal back contact with TCO makes ETLs an integral component to suppress charge recombination in highly-efficient PSCs.

Inorganic, wide bandgap, n-type semiconductors are excellent candidates and have been utilized extensively to fabricate highly-efficient PSCs thanks to their low cost and considerable charge mobility. Titanium dioxide (TiO_2) was often used due to its proper band alignment and high transmittance, however, the electron mobility of TiO_2 ($0.1\text{-}4 \text{ cm}^2 \text{ V}^{-1} \text{ s}^{-1}$)⁴⁴ is generally one to two orders of magnitude less than perovskite (10-

$100 \text{ cm}^2 \text{ V}^{-1} \text{ s}^{-1}$)^{45, 46} significantly limiting the efficiency of devices. Zinc oxide (ZnO) was first proposed as a promising alternative to TiO_2 due to its charge carrier mobility and ability to crystallize at low temperatures. However, Yang et. al. revealed that ZnO can induce proton-transfer reactions at the ZnO/perovskite interface, leading to decomposition of the perovskite film into PbI_2 .⁴⁷ Tin oxide (SnO_2) receives even more attention because of a variety of properties, first, the deeper conduction band favors the electron injection from perovskite and reduces potential Schottky barrier at the FTO/ SnO_2 interface, second, the high electron mobility ($240 \text{ cm}^2 \text{ V}^{-1} \text{ s}^{-1}$) supports fast electron transport, third, the wider band gap (3.5-3.6 eV) reduces the effect of photoexcitation due to ultraviolet (UV) illumination.^{48, 49} A variety of different approaches have been made to overcome the drawbacks of individual electron transport materials including metal sulfides, metal selenides, ternary ETLs, and amorphous ETLs while most optimization strategies are focused on introducing additional components, such as doping and interface modification.

Interfacial properties of PSCs play a crucial role not only in performance but also in stability of the cell. Tomas et. al. demonstrated that the exposure of TiO_2 to UV light can create photo-generated holes in TiO_2 , which subsequently react with adsorbed oxygen on the TiO_2 /perovskite interface, resulting in the formation of deep trap sites.⁵⁰ These trap sites significantly increase recombination at the interface, thus reducing the overall performance of the cell. This work demonstrates the various factors that can influence the suitability of an electron transport material for commercial perovskite applications, despite its demonstrated ability to function in high-efficiency PSCs.

Organic electron transport materials, such as [6,6]-phenyl-C₆₁-butyric acid methyl ester (PCBM) and C₆₀, have been employed as ETLs in p-i-n architectures with high efficiencies, achieving greater than 20%.^{51 52} However, organic ETLs are generally plagued by instability and are expensive, not suitable for mass production. These materials are useful for consistent, high-quality ETLs, utilized to study materials and processes related to other PSC layers, but the long-term viability of these materials is limited.

2.2.3 Perovskite Absorber Layer

The first iteration of a functioning PSC utilized a methylammonium lead triiodide (MAPbI₃) formulation and has remained the most widely studied formulation through 2022. Regardless of the particular formulation, the stability of perovskite materials is susceptible to alterations caused by environmental conditions such as temperature, moisture, and pressure.⁵³ The optoelectronic properties of perovskite films are dependent upon morphology, crystallinity, and stoichiometry, to name a few, that can be altered by pre-and post-treatments, doping, ambient conditions, deposition methods, solvents, molar compositions, drying conditions, and annealing parameters.⁵⁴⁻⁵⁷ Despite the remarkable progress, the most significant barriers to perovskite PV commercialization are stability, scalability, and manufacturing.⁵⁸

2.2.3.1 Instability of the perovskite layer

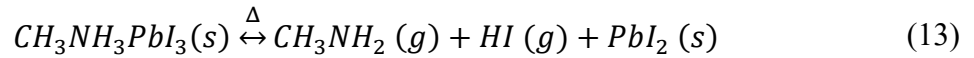
The Goldschmidt tolerance factor can be used to predict the crystal structure of perovskite materials, with the preferred cubic perovskite phase lying between 0.9-1.0.⁵⁹⁻⁶²

$$t = \frac{R_A + R_X}{\sqrt{2(R_B + R_X)}} \quad (11)$$

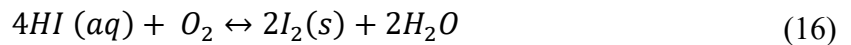
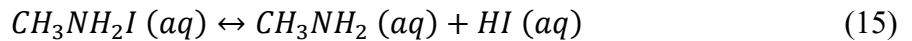
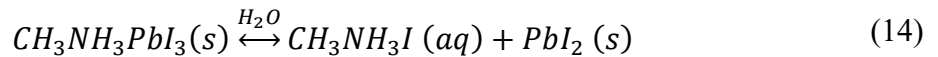
However, it must be noted that the tolerance factor alone is not sufficient for predicting the stability. Octahedral factor determines distortion and stability in perovskites with stable perovskites formed within 0.45-0.89 as follows:⁶³

$$\mu = \frac{R_B}{R_X} \quad (12)$$

The Goldschmidt tolerance factor and octahedral factor are useful indicators of intrinsic lattice strain, but it is important to consider external and operational factors that can degrade the perovskite. For example, thermal stressors at modest temperatures of 45-55°C can volatilize methylammonium (MA⁺) ions in MAPbI₃ perovskites, causing degradation into its components as shown below:^{22, 64}



Moisture acts as a catalyst in the decomposition of MAPbI₃ perovskites and is widely considered the leading cause of degradation in PSCs. Exposure to humidity and oxygen induces a 4-step degradation into its components as shown below:⁵³



Moisture catalyzes the breakdown of MAPbI₃ in equation 14, and the products formed then interact with both oxygen and light, causing irreparable damage to the absorber layer.

Electric fields, present during illumination, activate ion migration in the perovskite layer which create multiple mechanisms for degradation in the layer. At room temperature, a significant concentration of mobile MA⁺ and I⁻ exist.⁶⁵ Accumulation of these ions at HTL and ETL interfaces generate an electric field in opposition to the photo-generated field, thereby reducing the device efficiency.⁶⁶ Furthermore, the ion accumulation at HTL and ETL leads to significant hysteresis and non-steady current during current-voltage measurements.⁶⁷

The instability of perovskites is a result of both intrinsic and extrinsic factors. As such, various strategies have been developed to mitigate this degradation, which include modifications to the intrinsic properties of the absorber layer, as well as limiting exposure to external factors that may contribute to degradation.

2.2.3.2 Mixed Cation Perovskite Formulations

A-site substitutions include (MA⁺), formamidinium (FA⁺), cesium (Cs⁺), ethylammonium (EA⁺), and butylammonium (BA⁺) ions. Replacing MA⁺ with FA⁺ lowers the band gap of the absorber layer, but generally have better electronic properties, higher symmetry and PCE.⁶⁷ Mixing A-site cations have been shown to improve the perovskite crystallinity and phase stability, improve reproducibility, achieve stabilized power output efficiencies, unachievable by the individual compositions alone.^{68, 69} For example, both pure MA- and FA-based perovskites are sensitive to ambient conditions, however, the higher dipole moment of MA⁺ stabilizes photoactive α -FAPbI₃ perovskites when combined.⁷⁰ Unfortunately, the low volatility of MA cation leads to low thermal and photostability.²²

Transitioning from double cation systems to triple and quadruple systems, allows for another parameter to manipulate the perovskite properties. Introducing Cs to double cation systems reduces the tolerance factor towards the stable cubic α -phase and showed higher thermal stability and reproducibility.⁶⁸ Islam et al. reported that, according to their computational study, the addition of Cs to FAPbI₃ induces strain, due to the size mismatch, that suppresses re-orientation of FA⁺.⁷¹ These results were confirmed by Stranks et al. who showed that FAPbI₃ maintained the photoactive α -phase by octahedral tilting of 2°. ⁷² Compositional engineering strategies to suppress the transition to the hexagonal phase upon cooling to room temperature require an understanding of the re-orientational dynamics of FA⁺,⁷³ how they influence octahedral tilting in the halide perovskite, and how the re-orientational modes can be controlled through alloying in the A-site.⁶⁹

A number of strategies have been developed to mitigate A-site cation migration including surface passivation⁷⁴, use of mixed phases⁷⁵, and doping with alkali cations.⁷⁶ ⁷⁷ Schelhas et al. determined that an important parameter to determine phase stability is the Gibbs free energy of mixing (ΔG_{mix}).⁷⁸ Cs-FA perovskites with less negative ΔG_{mix} demonstrated poorer operational stability due to de-mixing of perovskite into photoinactive Cs-rich clusters, thus reducing cation migration.⁷⁹ Methods to reduce the A-site migration is important for mixed cation perovskites should improve operational stability and reduce hysteresis.

Saidaminov et al. suggests that A-site composition have a significant impact on carrier diffusivity across grain boundaries, where MA-based perovskites have an order of magnitude larger diffusivity than Cs-FA perovskites without MA.^{80, 81} Further research is

needed to understand how the relationship between A-site composition, lattice strain, and A-site organic molecule reorientation impact carrier dynamics.⁸²⁻⁸⁴

It is well established that mixing A-site cations improves stability as well as reproducibility of PSCs; however, the relationship of chemical composition/crystal structure/performance/phase stability is yet to be established. Many post-deposition characterization techniques have yielded a lot of information about re-orientation dynamics of alkylammonium cations and structural transitions of MA- and FA-based perovskites, but the lack of detailed information about the role of different cations in the crystallization mechanism need to be urgently addressed.⁶⁹

2.2.3.3 Mixed Halide Perovskite Formulations

Mixed-halide perovskite, such as $\text{MAPbI}_{3-x}\text{Cl}_x$ or $\text{MAPbI}_{3-x}\text{Br}_x$, exhibit superior PV performance in areas of electron-hole diffusion lengths, diffusion constants, and lifetimes.^{85, 86} Mixed-halide perovskite offer bandgap tunability essential for multijunction solar cells; however, detrimental halide segregation under light is often observed.⁸⁷ Br^- increases V_{oc} values and improves device stability while Cl^- enhances the film morphology by regulating the crystallization rate of the perovskite.⁸⁸⁻⁹⁰ The incorporation of small amounts of bromide and chloride ions into the MAPbI_3 perovskite crystal structure has been found to enhance its stability and performance, surpassing the properties of the individual crystal structures alone. This phenomenon is similar to that observed in mixed cation systems.

2.2.3.4 Perovskite Additives

Additives play a critical role in the field of perovskite precursor chemistry. Their functions extend to various aspects of perovskite film formation and performance,

including modulation of film morphology, stabilization of the essential components, namely FA and Cs, both in the precursor solution and in the final perovskite film, alignment of energy levels within the PSC, reduction of non-radiative recombination pathways, mitigation of hysteresis, and overall improvement of operational stability.⁹¹ These additives serve to optimize the crystalline structure of the perovskite film, ensure uniform coverage, enhance efficiency and stability, maximize the conversion of absorbed light into electrical energy, and prolong the lifespan of PSCs. The specific objectives of adding additives may vary, depending on the application, and often involve a combination of these factors.

The formation of 2-dimensional (2D) Ruddleson-Popper and Dion-Jacobson perovskites is driven by the selection of cationic species mixed into the perovskite structure. Incorporating 2D cations into both perovskite precursor chemistry and deposition at perovskite/CTL interfaces have demonstrated suppression of nonradiative recombination through passivation of perovskite surfaces at interfaces⁹², improve intrinsic stability of perovskite⁹³⁻⁹⁵, and stabilize photoactive perovskite phases⁹⁶. Jiang et al. applied a phenethylammonium iodide (PEAI) layer on top of perovskite to achieve a PCE of 23.32% with a Voc of 1.18 eV.⁹² A wide variety of PEAi applications have been shown to improve the performance of PSCs.⁹⁷⁻⁹⁹

Despite the abundance of additive materials, a limited number have been evaluated for compatibility with IPL annealing. Diiodomethane (CH_2I_2) has been shown to reduce pinholes, increase grain size, and improve overall device efficiency for both MAPbI_3 and triple cation PSCs using IPL annealing.^{100, 101} Xu et al. elucidated that the addition of CH_2I_2 promotes grain growth in the vertical direction, increases the I/Pb ratio

in the final film, and removes the I⁻ ionic diffusion/defect signature associated with iodine interstitials.¹⁰² The outcomes of these studies have led to the development of PSCs exhibiting PCEs greater than 17%, as well as significantly reduced annealing times to a millisecond scale.

2.2.4 HTL

HTLs are crucial components in PSCs, however, due to the greater impact of ETLs on the device performance, this section will be comparatively brief. HTLs are characterized by high hole mobility, thermal and UV stability, and a well-matched highest occupied molecular orbital (HOMO) or valence band. The selection of hole transport layers to form ohmic contacts is important as it not only reduces the energy barrier height for efficient charge extraction, but also maximizes the V_{oc} with an optimum built-in potential.¹⁰³

HTLs can be divided into two categories: organic and inorganic. Inorganic HTLs, such as nickel oxide (NiO_x) and molybdenum oxide (MoO_3), have high hole mobility but are difficult to manufacture efficiently.¹⁰⁴ Organic HTLs, such as spiro-OMeTAD and poly[bis(4-phenyl)(2,4,6-trimethylphenyl)amine] (PTAA), have lower stability and higher cost.¹⁰⁴ Currently, there is a trade-off between efficiency of manufacturing and stability for HTLs, making it difficult to find a suitable material for commercial use.

2.3 Scalable deposition of perovskite layer

Roll-to-roll processing is an important class of substrate-based manufacturing processes in which additive and subtractive processes are used to build structures in a continuous manner. The utilization of roll-to-roll production techniques, combined with scalable deposition methods, presents a significant opportunity for achieving low-cost,

high-throughput manufacturing.¹⁰⁵ A simplistic schematic of a concept roll-to-roll manufacturing line is presented below:

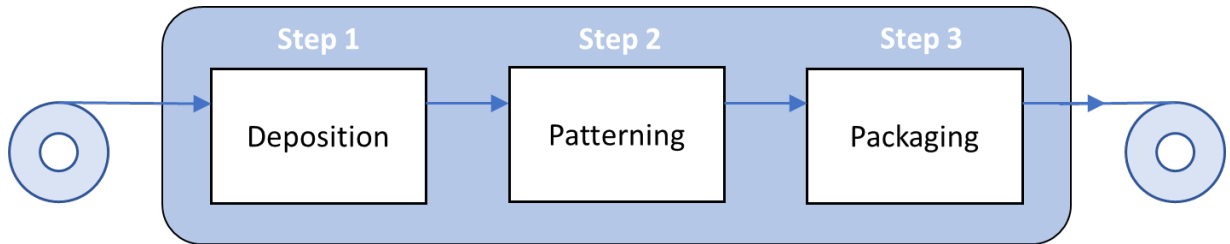


Figure 8: Roll-to-roll processing concept flow schematic.

Various scalable deposition methods have been developed, categorized as solution-deposition methods and vapor-deposition methods. The popular solution phase methods include spin coating¹⁰⁶, blade coating¹⁰⁷, slot-die coating¹⁰⁸, bar coating^{109, 110}, spray coating¹¹¹, inkjet printing^{112, 113}, and screen printing¹¹⁴. Spin-coating is a widely studied technique for the deposition of thin films, however, it is known to be less suitable for large-scale production when compared to other techniques. This is due to its limitations in terms of scalability and uniformity.

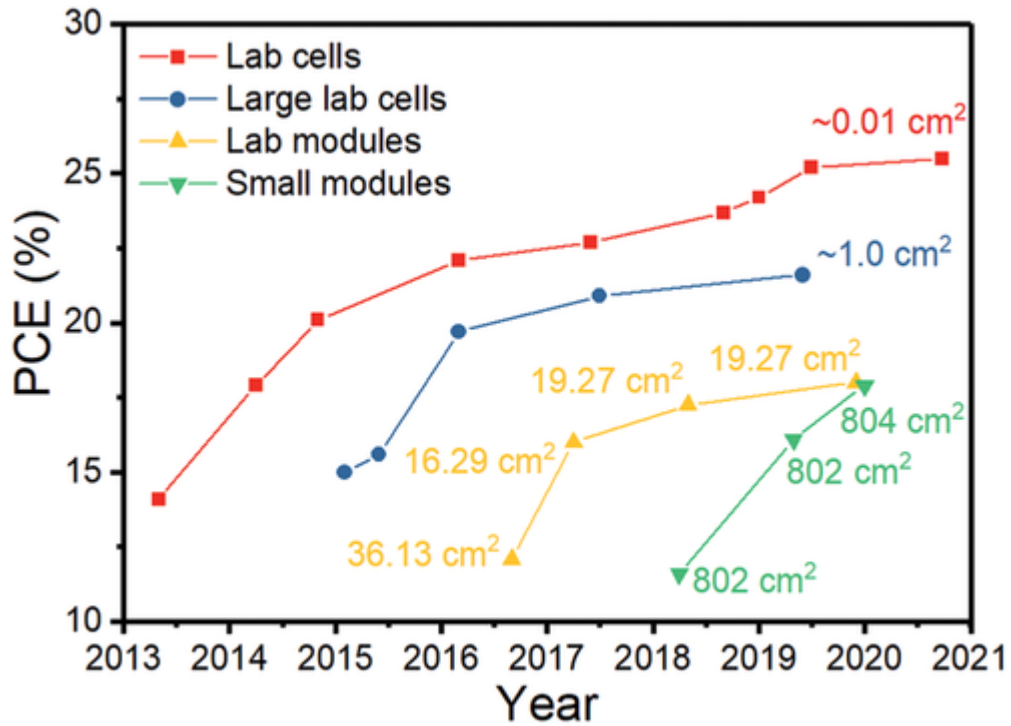


Figure 9: Certified PCE for champion PSCs and perovskite solar modules. Lab cells ($\sim 0.01 \text{ cm}^2$); large lab cells ($\sim 1.0 \text{ cm}^2$); lab modules ($10\text{-}200 \text{ cm}^2$); small modules ($800\text{-}6500 \text{ cm}^2$)³¹

For most types of solar cell technologies, the absolute PCE value decreases by $\sim 0.8\%$ when the device area increases by an order of magnitude, caused by added series resistance (R_s), from sheet resistance of the transparent electrode, increasing linearly as the area increases.³²⁻³⁴ The PCE loss of perovskite solar modules far exceeds this rate due to non-uniform deposition of all functional layers, with perovskite being the most important and challenging, as shown in figure 9.³¹ Table 2 presents data on the performance of PSCs fabricated using scalable methods, including the structural information, PCE, and device area, highlighting the significant loss in PCE for non-conventional deposition techniques and large pixel sizes.

Table 2: Literature survey of demonstrated scalable coating methods, accompanied by the perovskite structure, and device area.

Deposition Method	Structure	Substrate	PCE (%)	Area (cm ²)	Date	Ref.
Inkjet Printing	MAFACsRb Perovskite	Glass	16.09	802	2020	113
Slot-Die Coating	ITO/TiO ₂ /MAPbI ₃ xClx/spiro-OMeTAD/Au	Glass	10	168.75	2018	108
Spray Coating	CsFA Perovskite	Glass	13.82	112	2021	115
Doctor Blading	FTO/TiO ₂ /MAPbI ₃ /spiro-OMeTAD/Au	Glass	4.3	100	2015	116
Slot-Die Coating	FA0.83Cs0.17PbI ₃	Glass	19.54	65	2021	117
Doctor Blading	ITO/PTAA/MAPbI ₃ /C60/BCP/Cu	Glass	14.6	57.2	2018	118
Blade Coating	MA0.6FA0.4PbI ₃	Glass	19.7	50.1	2021	119
Blade Coating	FTO/c-TiO ₂ /m-TiO ₂ /FA1-x-yMAxCs _y (I1-xBr _x) ₃ /spiro-OMeTAD/Au	Glass	11.59	50	2020	120
Slot-Die Coating	ITO/ZnO/MAPbI ₃ /P3HT/Ag	Glass	4.6	47.3	2015	121
Spray Coating	FTO/TiO ₂ /MAPbI ₃ xClx/PTAA/Au	Glass	15.5	40	2016	111
Slot-Die Coating	FTO/NiO _x /(FAPbI ₃) _{0.95} (MAPbI ₃) _{0.05} /G-PCBM/BCP/Ag	Glass	14.17	36	2019	122
Doctor Blading	ITO/PTAA/MAPbI ₃ /C60/BCP/Cu	Glass	15.3	33	2018	118
Doctor Blading	FTO/TiO ₂ /MAPbI ₃ xClx/spiro-OMeTAD/Au	Glass	13.3	11.09	2017	123
Slot-Die Coating	FTO/ZnO/MAPbI ₃ /carbon	Glass	17.61	10.6	2017	124
Doctor Blading	FTO/TiO ₂ /MAPbI ₃ /spiro-OMeTAD/Au	Glass	10.4	10.1	2015	116
Blade Coating	ITO/PTAA/MAPbI ₃ /PCBM/BCP/Ag	Glass	11.25	10.1	2019	125
Blade Coating	ITO/PTAA/MAPbI ₃ /PC61BM/BCP/Ag	Glass	15.38	10.1	2020	126
Slot-Die Coating	ITO/PEDOT:PSS/MAPbI ₃ /C60/PCBM/BCP/Al	Glass	8.3	10	2018	127
Blade Coating	FTO/c-ZnO-ZnS/m-TiO ₂ /MAPbI ₃ /Spiro-OMeTAD/Au	Glass	15.79	8	2019	128
Blade Coating	FTO/SnO ₂ /FA1-xCsxPbI ₃ /Spiro-OMeTAD/Au	Glass	16.69	8	2021	129
Slot-Die Coating	FTO/TiO ₂ /FA0.91Cs0.09PbI ₃ /(M4N)BF ₄ /Spiro-OMeTAD/Au	Glass	19.6	7.92	2020	130
Spray Coating	ITO/TiO ₂ /MAPbI ₃ xBrx/spiro-OMeTAD/Au	Glass	11.7	3.8	2016	131

Inkjet Printing	FTO/TiO ₂ /meso-TiO ₂ /MAPbI ₃ /spiro-OMeTAD/Au	Glass	17.7	2.02	2018	132
Doctor Blading	FTO/TiO ₂ /MAPbI ₃ xClx/spiro-OMeTAD/Au	Glass	17.3	1.2	2017	123
Blade Coating	FTO/c-TiO ₂ /CsPbI ₂ Br/spiro-OMeTAD/Au	Glass	12.52	1	2019	133
Spray Coating	FTO/TiO ₂ /MAPbI ₃ /spiro-OMeTAD/Au	Glass	13.1	1	2016	134
Vapor Deposition	FTO/TiO ₂ /C60/MAPbI ₃ /BAI/Spiro-OMeTAD/Au	Glass	14.1	1	2019	135
Doctor Blading	FTO/TiO ₂ /MAPbI ₃ /spiro-OMeTAD/Au	Glass	17.1	1	2018	136
Blade Coating	FTO/c-TiO ₂ /m-TiO ₂ /FA1-x-yMAxCSy(I1-xBrx) ₃ /spiro-OMeTAD/Au	Glass	17.77	1	2020	120
Doctor Blading	FTO/TiO ₂ /FA0.85MA0.15PbI ₂ .55Br0.45/PTAA/Ag	Glass	20	0.98	2017	137
Inkjet Printing	FTO/TiO ₂ /MAPbI ₃ /carbon	Glass	11.6	0.15	2014	138
Spray Coating	FTO/TiO ₂ /meso-TiO ₂ /FA0.9Cs0.1PbI ₃ /spiro-OMeTAD/Au	Glass	14.2	0.15	2016	134
Doctor Blading	FTO/TiO ₂ /MAPbI ₃ xClx/spiro-OMeTAD/Au	Glass	18.6	0.12	2017	123
Slot-Die Coating	ITO/ZnO/MAPbI ₃ /P3HT/Ag	Glass	11.9	0.1	2015	139
Doctor Blading	FTO/TiO ₂ /MAPbI ₃ /spiro-OMeTAD/Au	Glass	13.3	0.1	2015	116
Spray Coating	FTO/TiO ₂ /MAPbI ₃ /spiro-OMeTAD/Au	Glass	16	0.1	2016	134
Inkjet Printing	FTO/TiO ₂ /MAPbI ₃ /spiro-OMeTAD/Au	Glass	11.3	0.09	2016	140
Doctor Blading	FTO/TiO ₂ /MAPbI ₃ /spiro-OMeTAD/Au	Glass	18.7	0.09	2018	136
Doctor Blading	ITO/MAPbI ₃ /C60/BCP/Cu	Glass	20	0.08	2018	141
Slot-Die Coating	ITO/PEDOT:PSS/(BA) ₂ (MA) ₃ Pb ₄ I ₁₃ /PCBM/PEIE/Ag	Glass	14.9	0.078	2019	142
Doctor Blading	ITO/PEDOT:PSS/MAPbI ₃ /PCBM/C60/BCP/Al	Glass	15.1	0.0725	2015	143
Spray Coating	PET/ITO/TiO ₂ /MAPbI ₃ xClx/spiro-OMeTAD/Au	PET	8.1	0.065	2015	144
Slot-Die Coating	ITO/SnO ₂ /MAPbI ₃ /spiro-OMeTAD/Au	Glass	18	0.06	2018	145
Doctor Blading	ITO/PEDOT:PSS/MA0.6FA0.4PbI ₃ /PCBM/Ca/Al	Glass	11.5	0.04	2015	146
Inkjet Printing	FTO/TiO ₂ /meso-TiO ₂ /MAPbI ₃ xClx/spiro-OMeTAD/Au	Glass	12.3	0.04	2014	147

Inkjet Printing	FTO/TiO ₂ /MAPbI ₃ /spiro-OMeTAD/Au	Glass	17	0.04	2018	148
Inkjet Printing	FTO/TiO ₂ /meso-TiO ₂ /MAPbI ₃ /spiro-OMeTAD/Au	Glass	18.6	0.04	2018	132
Doctor Blading	ITO/PEDOT:PSS/MAPbI ₃ /PCBM/Bis-C60/Ag	Glass	12.2	0.0314	2015	149
Spray Coating	ITO/PEDOT:PSS/MAPbI ₃ xClx/PCBM/LiF/Al	Glass	9.9	0.025	2016	134
Spray Coating	ITO/PEDOT:PSS/MAPbI ₃ xClx/PCBM/Ca/Al	Glass	11.1	0.025	2014	150
Doctor Blading	ITO/PTAA/MA0.6FA0.38Cs0.02PbI ₂ .975Br0.025/C60/BCP/Cu	Glass	19.3	—	2017	151

PET – polyethylene terephthalate, BCP - Bathocuproine

Two scalable deposition methods are briefly introduced: blade coating and slot-die coating. A comprehensive description of these techniques, along with their underlying fundamental equations, can be found in sections 2.3.1.2 and 2.3.1.3, respectively. For a deeper discussion of the principles governing these methods relevant to PSC deposition, refer to the aforementioned sections.

Blade coating, depicted in figure 10, is a method of film deposition that utilizes a coating tool to spread a solution over a substrate surface, leveraging the principles of meniscus coating. The resulting films are influenced by factors such as the shape of the meniscus, the flow dynamics within the meniscus, and the evaporation rate of the solvent.¹⁵² Blade coating is a relatively simple, efficient, and cost-effective method that can be adapted for large-scale production through the use of a roll-to-roll process.^{32, 107, 143} Additionally, the nature of the coating process offers wider surface coverage compared to spin-coating and improved uniformity for large-area devices.¹⁵³

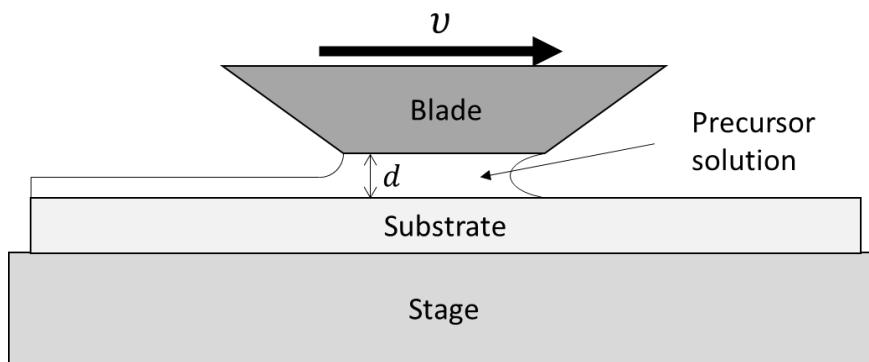


Figure 10: Schematic of blade coating thin films from a side angle, displaying the precursor solution meniscus between blade and substrate.

Slot-die coating, depicted in figure 11, is a technique in which a coating solution is applied to a substrate via a coater with an upstream and downstream die. The solution is dispensed from a distribution chamber and flows through a feed slot between the dies. The properties of the resulting film are influenced by various factors, such as coating speed, flow rate, coating gap, and viscosity of the solution. This technique demonstrated scalability by the production of a flexible perovskite solar module with an active area of 40 cm^2 , through the integration of slot-die coating into a roll-to-roll process.¹³⁹ Although slot-die coating is a mature, scalable deposition method, it remains challenging to control the film quality over large-areas in perovskite solar modules, highlighting the need for ongoing research in fluid dynamics and slot-die design for this technology.

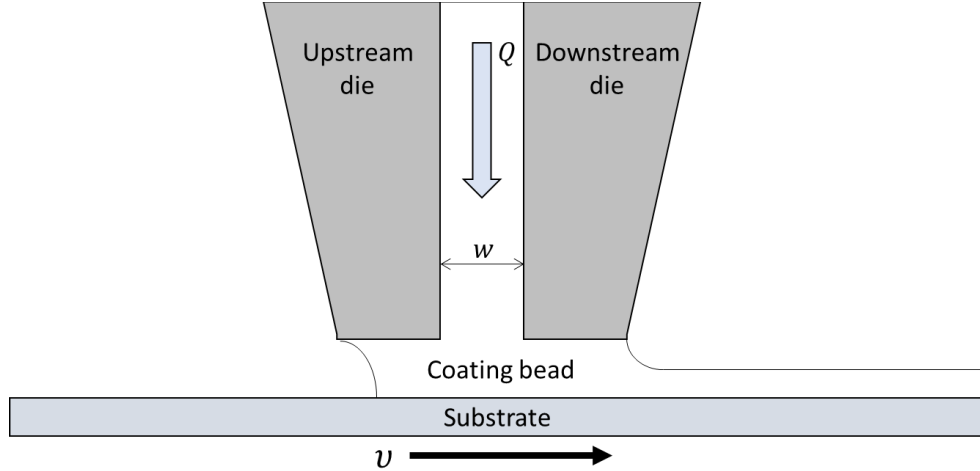


Figure 11: Schematic of slot die coating thin films from a side angle, displaying the coating bead formation.

2.3.1 Perovskite film formation

Perovskite formation is the combination of nucleation and crystal growth processes.^{154, 155} Perovskite film formation is conventional modeled via the formation of colloidal particles from a solution. In colloidal particle formation, a monomer is defined as the minimal building unit of a crystal and can either form crystal particles or dissolve back into the solution, depending on the level of supersaturation.¹⁵⁵ In the classical theory of nucleation, a nucleus is considered a sphere of condensed phase where its free energy is defined by thermodynamic terms below:

$$\Delta G(r) = 4\pi r^2 \gamma + \frac{4}{3} \pi r^3 \Delta G_v \quad (18)$$

where r is the radius of the nucleus, γ is the surface energy per unit area, and ΔG_v is the free energy per unit volume of a crystal. This term is defined by the difference between free energy of a monomer in the crystal and in solution, shown below:

$$\Delta G_v = -\frac{RT \ln S}{V_m} \quad (19)$$

where V_m is the molar volume of the monomer in crystal, T is the temperature, R is the gas law constant, and S is the level of supersaturation ($[M]/[M]_0$, $[M]_0$ is equilibrium concentration of the bulk solid). The first term in equation 18 represents the surface energy contributions to the free energy of a nucleus, while the second term represents the bulk free energy contributions to the free energy of a nucleus. $G(r)$ is plotted in figure 12. There exists a critical radius (r_c) where a nucleus with radius smaller than r_c will redissolve into solution, to decrease the free energy. Thus, the critical radius is the minimum size of nuclei that can resist dissolution and grow further.

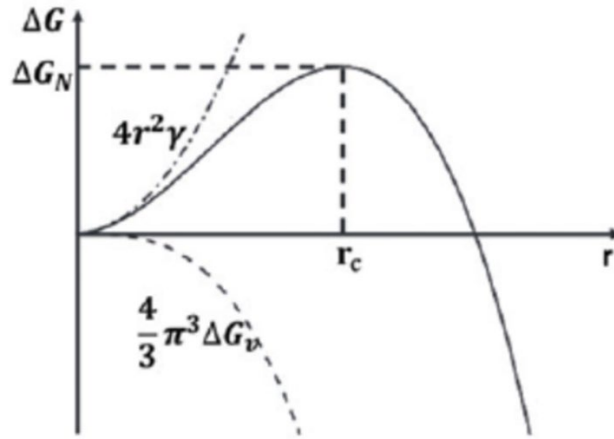


Figure 12: Plot of the Gibbs free energy

The reaction rate for the formation of nuclei can be written in the Arrhenius form, where the formation energy of nuclei (ΔG_N) is equal to $\Delta G(r_c)$, as follows:

$$\frac{dN}{dt} = A \exp \left[\frac{-\Delta G_N}{k_B T} \right] = A \exp \left[-\frac{16\pi\gamma^3 V_m^2}{3k_B^3 T^3 N_A^2 (\ln S)^2} \right] \quad (20)$$

As shown, the nucleation rate is strongly dependent on the level of supersaturation, temperature, and surface free energy. By manipulating these parameters, it is possible to control the nucleation rate and subsequently influence the quality of the resulting perovskite film.

The growth of particles in solution is driven by mass transport of monomers from the bulk solution onto the particle surface (Fick's first law) and the reaction of monomers on the surface as shown below:

$$J = 4\pi r^2 D \frac{d[C]}{dx} = 4\pi D r ([M]_b - [M]_s) \quad (21)$$

$$J = 4\pi r^2 k ([M]_s - [M]_r) \quad (22)$$

where J is the monomer flux, D is the diffusion coefficient, $[M]_b$ is the bulk concentration of the solution, $[M]_s$ is the concentration at the surface of the particle, $[M]_r$ is the solubility of the spherical particle of radius r .

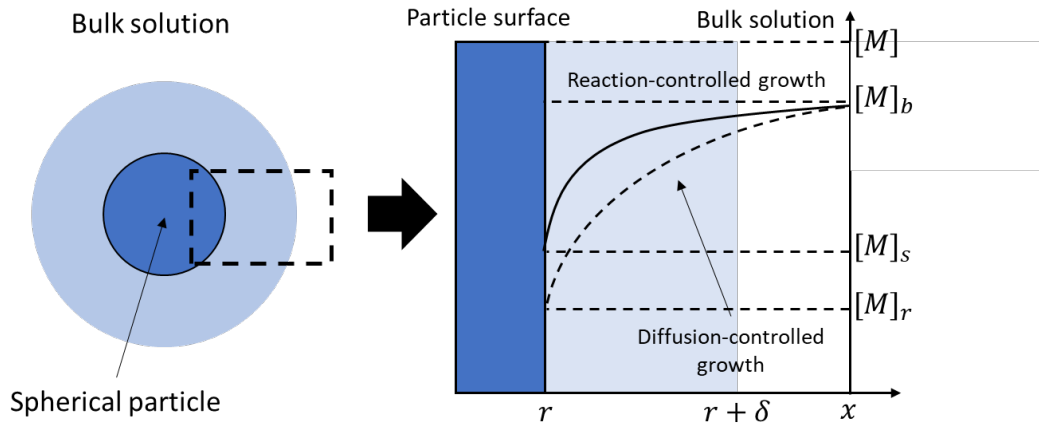


Figure 13: Schematic illustration of diffusion layer structure neat the surface of a nanocrystal (left) and plot for the monomer concentration as a function of distance x (right). Shaded area represents the diffusion layer.

Due to the Gibbs-Thomson effect, larger particles have lower solubility, therefore, they grow at faster rates. According to equations 21 and 22, the overall particle growth rate is determined by either diffusion or surface reaction, respectively. On account of steady state solute diffusion, diffusion-controlled growth facilitates uniform size particles.

The overall nucleation and crystal growth processes for perovskites are generally depicted by the LaMer plot, which describes the concentration of perovskite precursors changing as a function of time for isothermal evaporation of solvent.¹⁵⁵ This plot is shown in figure 14 and displays three stages in the process. In the first stage, monomers accumulate in the solution. Monomer concentration increases until it reaches supersaturation, signifying the transition to phase II. The process of nucleation reduces the precursor concentration in the bulk solution and will continue until the precursor in solution can no longer achieve supersaturation. This critical point signifies the transition to phase III where spontaneous nucleation is no longer present and diffusion-controlled crystal growth becomes the dominant process.

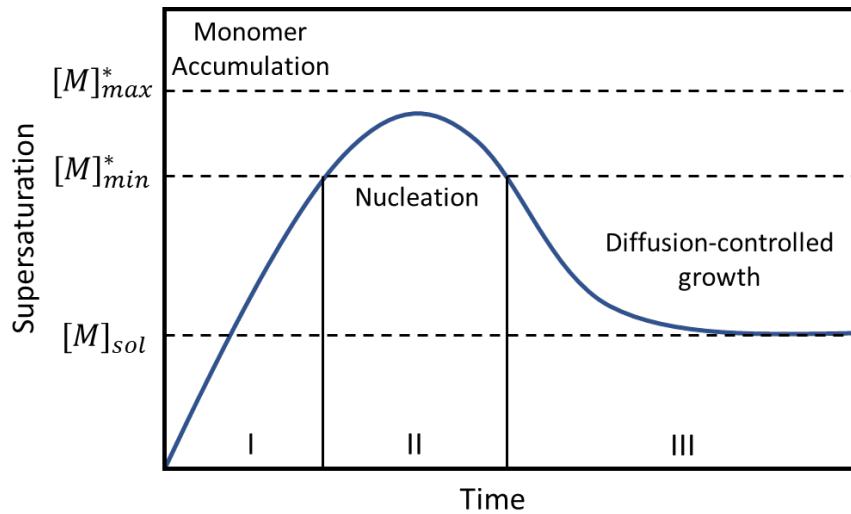


Figure 14: LaMer diagram depicting three stages in the formation of uniform colloidal particles.

The diffusion-controlled growth of crystals in phase III can also be described by the process of Ostwald ripening. This process is characterized by the preferential dissolution of smaller particles and subsequent growth of larger particles. The driving force for this process is the difference in chemical potential between smaller and larger particles, with smaller particles being energetically more unstable than larger particles, shown in equation 23.¹⁵⁶⁻¹⁵⁸

$$\mu = \mu_0 + \frac{2\gamma V_m}{r} \quad (23)$$

where, μ is surface chemical potential on the surface, μ_0 is the chemical potential for a flat surface, γ is surface energy, V_m is the mole volume of a particle and r is the particle radius. As a result, the concentration of dissolved precursors near small particles is always higher than that near large particles, causing mass transport towards the large particle via Fick's first law.

As discussed, the formation of perovskite films is affected by the use of different solvents, additives, and precursor compositions. The complexity of film formation, due to the presence of multiple factors, leads to a range of experimental phenomena that can be challenging to reconcile with theoretical predictions. In general, strategies that focus on suppressing crystal growth and promoting rapid nucleation generally result in more consistent and reliable coating processes.

2.3.1.1 Deposition - Solvents

The choice of solvent is a crucial factor in determining the morphology of the perovskite absorber layer. The solvent is the medium used to dissolve the perovskite precursor materials, and the chemical properties of the solvent can greatly impact the coordination between the solvent and the perovskite precursors. Consequently, selecting the appropriate solvent serves as the most direct method to influence precursor solubility, which in turn has significant implications for film quality, as previously discussed. For example, the use of organic solvents like dimethylformamide (DMF) or dimethylsulfoxide (DMSO), which have lone pair electrons, can form Lewis acid-base adducts with the Lewis acid Pb^{2+} . The utilization of a combination of solvents in perovskite ink formulation has been demonstrated to promote fast nucleation and suppress crystal growth through the synergistic interaction of their unique properties.

The Lewis basicity of a solvent, as quantified by its Donor Number (D_N), plays a crucial role in its ability to dissolve perovskite precursors. Solvents with high D_N , such as DMF, DMSO, N-methyl-2-pyrrolidone (NMP), N,N-dimethylacetamide (DMA), and γ -butyrolactone (GBL), are commonly utilized for this purpose.^{98, 159-174} However, it should be noted that the solubility of the precursor also depends on the coordination between the

solvent and solute, which can be influenced by both the D_N and polarity of the solvent. Additionally, the evaporation rate of the solvent system is not solely determined by its boiling point, vapor pressure, and viscosity, but also by its D_N and polarity.¹⁷⁵ The D_N serves as an example of how a single material property cannot fully predict the interaction between a solvent and perovskite precursors, highlighting the complex and interconnected nature of the various parameters that can be used to manipulate the overall performance of the solvent system.

Deng et al. chose to define solvents as either NVCS and VNCS.¹⁷⁶ They highlighted the ability to utilize the relationship between donor number and vapor pressure to promote fast nucleation, via VNCSs, and retard crystallization, via NVCSs. A summary of this relationship is shown in figure 15.

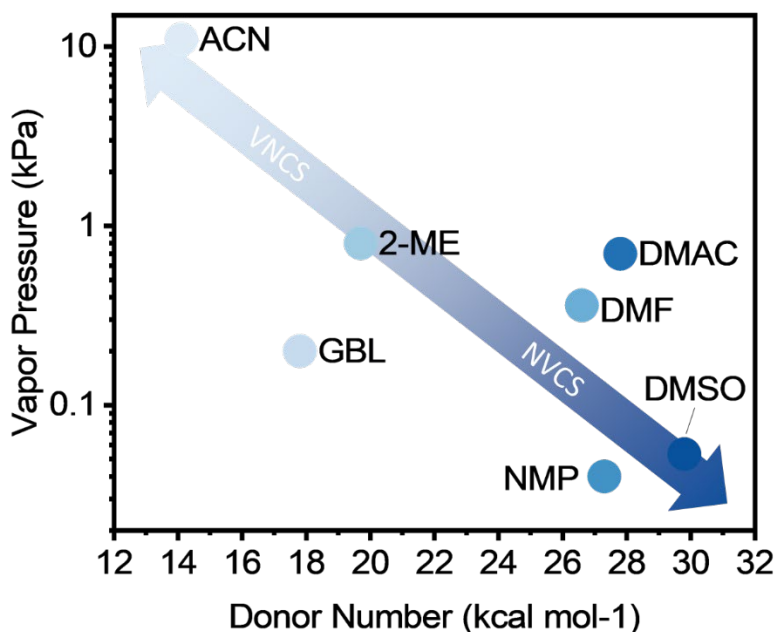


Figure 15: Plot of vapor pressure and Donor number for commonly used perovskite solvents. Plot credit: Deng et al.¹⁷⁶

As the production of PSCs continues to progress towards industrial scale, the physical properties of the precursor solution become increasingly significant in determining the outcome of the film formation process. The challenge is mainly focused on the regulation of the process time window, which requires the precise control of the coordination ability, volatility, and viscosity of the solvent.^{118, 123, 177, 178}

The intricate interactions inherent in perovskite precursor chemistry enable the generation of a vast array of potential precursor solvents. A table summarizing the PV characteristics of PSCs synthesized using various solvent systems is presented below.

Table 3: Literature survey of commonly used perovskite solvents, highlighting their characteristics performance metrics and year when published.

Solvent(s)	V _{oc} (V)	J _{sc} (mA cm ⁻²)	FF (%)	PCE (%)	Date	Ref
DMF/DMSO	1.13	25.92	82.02	24.02	2019	179
DMF/DMSO	1.01	20.82	72	15.14	2018	180
DMF/NMP	1.1	23.98	76.9	20.19	2018	161
DMF/GBL	0.92	8.74	76	6.16	2014	166
HMPA/DMSO	1.08	22.53	80.1	19.5	2016	170
DMF/DMA	1.02	22.49	70	16.05	2017	165
GBL/DMSO	1.02	21.8	78.7	17.6	2016	177
DMF/DMSO 2D	1.11	18.89	49.53	10.41	2018	181
DMF/DMSO 2D	1.08	19.45	58.22	12.37	2018	136
DMAC (2D)	1.13	14.61	73.08	12.15	2019	182
GBL	0.86	12.93	67	7.47	2016	183
NMP	0.76	8.78	56	3.77	2016	183
DMA	1.02	21.47	63.4	13.9	2014	174
DMSO	1.07	22.84	76.11	18.62	2016	184
DMSO	1.02	20.71	64	13.5	2014	185
2-ME	0.97	19.32	81.6	15.32	2017	186
ACN/MA	1.1	22.2	77	19	2017	187
ACN/MA	1.05	21.06	72	15.9	2017	141
ACN/THF/MMA	1.13	23.83	80.9	21.8	2020	188
ACN/DMF	1.15	22.69	75.33	19.7	2016	189
2-ME/ACN/DMSO	1.13	23	81.8	21.3	2019	176
GBL/EtOH	0.88	18.8	62	11	2016	190

GBL/EtOH/AcOH	0.88	21.2	71	15.1	2016	190
H						
GBL/PrOH/AcOH	0.9	17.2	72	14	2016	190
H						
GBL/EtOH/AcOH	0.89	21.1	73	14.5	2016	190
H						
GBL/EtOH/AcOH	3.35	5.1	69	11.9	2016	190
H						
H ₂ O	1.08	22.4	70	16.7	2020	191
H ₂ O/DMF	1.03	20.06	85	18	2015	192
H ₂ ODMF/DMSO	1.09	22.1	80.8	20.1	2018	193

Extensive research to investigate the effects of various properties on the deposition and formation of perovskite thin films. However, it is important to exercise caution in the selection of solvents used in the process, as certain physical or chemical properties may lead to downstream issues that hinder the optimization of post-deposition strategies for perovskite.

2.3.1.2 Deposition – Blade Coating

Both blade and slot-die coating methods are liquid-film based deposition techniques, where the precursor solution is transferred to the substrate in the form of a semi-wet liquid film. There are two regimes in blade coating: the evaporation regime and Landau-Levich regime. The correlation between blade speed and film thickness can be utilized to determine the regime of film deposition, as illustrated in figure 16.¹⁵²

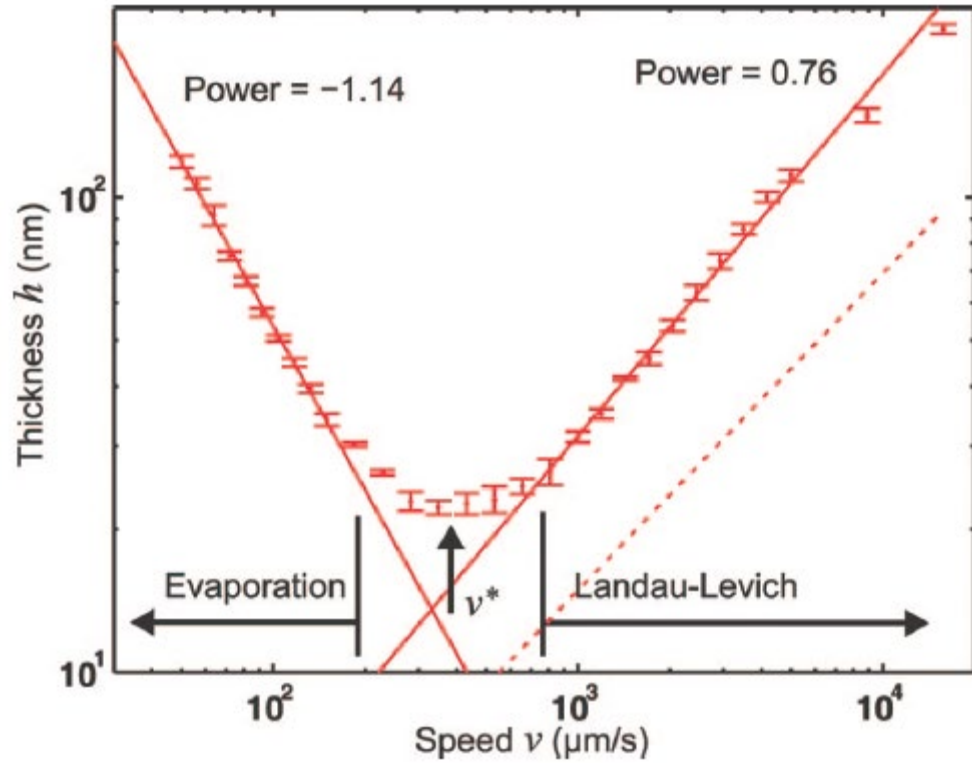


Figure 16: Measured film thickness h as a function of deposition speed. Two regimes are identified as a function of v^* : evaporation and Landau-Levich.¹⁵²

The film thickness reaches a minimum around a blade speed denoted v^* . When $v < v^*$, the deposition is in the evaporation regime. Le Berre et al. suggested that film thickness of colloidal solutions can be predicted through the application of a mass balance around the meniscus, under the assumption of negligible Marangoni effects (which is common for colloidal solutions).^{152, 194} The model predicts that film thickness increases as blade speed decreases, with the slope being influenced by factors such as precursor concentration, evaporation rate, fluid density, and film width, as depicted below:

$$h = \frac{[M]_{s,mass} Q_{evap}}{\rho L} v^{-1} \quad (24)$$

where h is the film thickness, $[M]_{s, mass}$ is the monomer mass concentration in the solution, ρ is the monomer density, L is the width of the film, Q_{evap} is the flow rate of solvent leaving the box,

When $v > v^*$, viscous forces become strong enough to drag out a liquid film from the meniscus, transitioning to the Landau-Levich regime.¹⁹⁵ Applying Landau, Levich, and Derjaguin's work, Le Berre et al. developed this model for predicting film thickness in the Landau-Levich regime for blade coating systems:

$$h = 1.34 \frac{[C]_{bulk}}{\rho} \frac{l}{\cos \theta_1 + \cos \theta_2 - \frac{l^2}{2\kappa^{-2}}} C_S^{2/3} \quad (25)$$

where $\kappa^{-1} = \gamma/\rho g^{1/2}$ is the capillary length (γ , surface tension; ρ , density of precursor solution) and $Ca = \eta v/\gamma$ is the capillary number (η , liquid viscosity). Additionally, θ_1 , θ_2 , and l are geometric parameters related to the back meniscus. Landau-Levich depositions theoretically should result in perovskite thin films with a narrower distribution of domain sizes and fewer defects compared to evaporation depositions, making it the more favorable method for achieving consistent films.

Mallajosyula et al. expanded upon Le Berre et al.'s study by investigating the effect of substrate temperature and solvent volume on not only thickness, but film uniformity and crystallinity as well.¹⁹⁶ Ernst et al.¹⁹⁷ combined models developed by Le Berre et al. and Davis et al.¹⁹⁸ to predict film thickness and found that the predictions matched well with experimental data.

A limitation of current models is that they fail to consider the differential evaporation rates of multiple solvents in multi-solvent systems, which is a frequent practice in perovskite film fabrication. Additionally, although film thickness plays a role

in determining the performance of a perovskite film as a solar material, current models lack the capability to accurately predict the crystallinity and uniformity of the film from the physical properties of precursor solutions. Further advancements in modeling are needed to address this limitation.

2.3.1.3 Deposition – Slot die coating

The diverse substrate materials, rheological properties of precursor solutions, and complex set of competing forces that act on the coating bead (capillary, viscous, inertial, gravitational) during slot-die coating result in a wide range of experimental phenomena that are not fully understood and cannot be uniformly explained by a single theory, despite its effectiveness in fabricating various products over decades.¹⁹⁹ A major concern in slot die coating processes is how to determine the operating limits to set the appropriate range of operating parameters (coating speed, coating gap, liquid viscosity, flow rate, surface tension, etc.). The most common concepts to describe operating limits are low-flow limit, minimum wet thickness, coating window, and maximum wetting speed. Ruschak established operating limits for a capillary model using equations 26 and 27.²⁰⁰ Ruschak’s work, in collaboration with other existing studies, serves as a guide for the perovskite community to achieve consistent and large scale manufacturing of PSCs.

$$-\frac{\sigma_u(1 + \cos\theta)}{h_u} + 1.34Ca^{2/3}\frac{\sigma_d}{t} \leq \Delta p \leq \frac{\sigma_u(1 - \cos\theta)}{h_u} + 1.34Ca^{2/3}\frac{\sigma_d}{t} \quad (26)$$

$$0 \leq \frac{1}{t} \leq \frac{1.49}{h_d}Ca^{-2/3} \quad (27)$$

where, equations 26 and 27 set the limits of vacuum pressure and wet thickness, respectively. Here, σ_u and σ_d are the surface tensions at the upstream and downstream menisci, respectively. Δp represents the vacuum pressure between the upstream and

downstream menisci (i.e. the pressure outside the upstream meniscus). Ca is the capillary number, $\frac{\mu U}{\sigma_d}$, based on the downstream surface tension. μ is the viscosity of the coating fluid.

As the PSC technology continues to advance towards large-scale production, the need for scalable deposition techniques such as slot die and blade coating will become increasingly vital. Therefore, a deeper understanding of slot die modeling is crucial and requires immediate attention in order to facilitate the advancement of PSC industry.

2.3.2 Drying

Post-deposition drying of perovskite wet films is a critical step in the production of perovskite solar cells. Improper drying can result in the formation of dendritic structures, which can negatively impact the surface coverage and create shunted paths within the solar cell. Various methods have been proposed for achieving this, including anti-solvent extraction²⁰¹, heating^{143, 202, 203}, forced laminar air flow drying^{204, 205}, vacuum-assisted drying²⁰⁶⁻²⁰⁸, or a combination of these approaches.²⁰⁹ The ideal method would promote rapid supersaturation while simultaneously suppressing or not contributing to rapid crystal growth. Anti-solvent extraction has been the most widely-used technique for spin-coating applications, however, its translation to roll-to-roll applications is not straightforward and may not be the most ergonomic option.

Forced laminar air flow drying involves an air knife (or air jet) blown over the solvent surface to reduce the boundary layer and enhance both convective heat transfer and mass transfer, as shown in figure 17. Higher velocity and higher air temperatures both provide enhanced evaporation. The heat and mass transfer analogy gives a relation between convective heat transfer and convective mass transfer, where the resulting mass

transfer coefficient can be used to estimate the solvent evaporation rate, as shown below.²¹⁰

$$\frac{\dot{m}_{evap}}{A_{film}} = h_m(\rho_{A,S} - \rho_{A,\infty}) \quad (28)$$

where \dot{m}_{evap} is the rate of solvent mass evaporated, A_{film} is the film surface area, h_m is the convective mass transfer coefficient, and $\rho_{A,S}$ is the mass density of solvent vapor at the film surface and $\rho_{A,\infty}$ is the mass density of solvent vapor far from the surface. Ding et al. showed that perovskite film thickness is inversely proportional to air knife pressure and had beneficial qualities for larger grains and more crystalline films.²¹¹ The wealth of knowledge on laminar flow drying have resulted in precise quantitative modeling for predictive perovskite thin film formation.²⁰⁵ It is a facile, reproducible, and low-cost technique to dry PSCs.

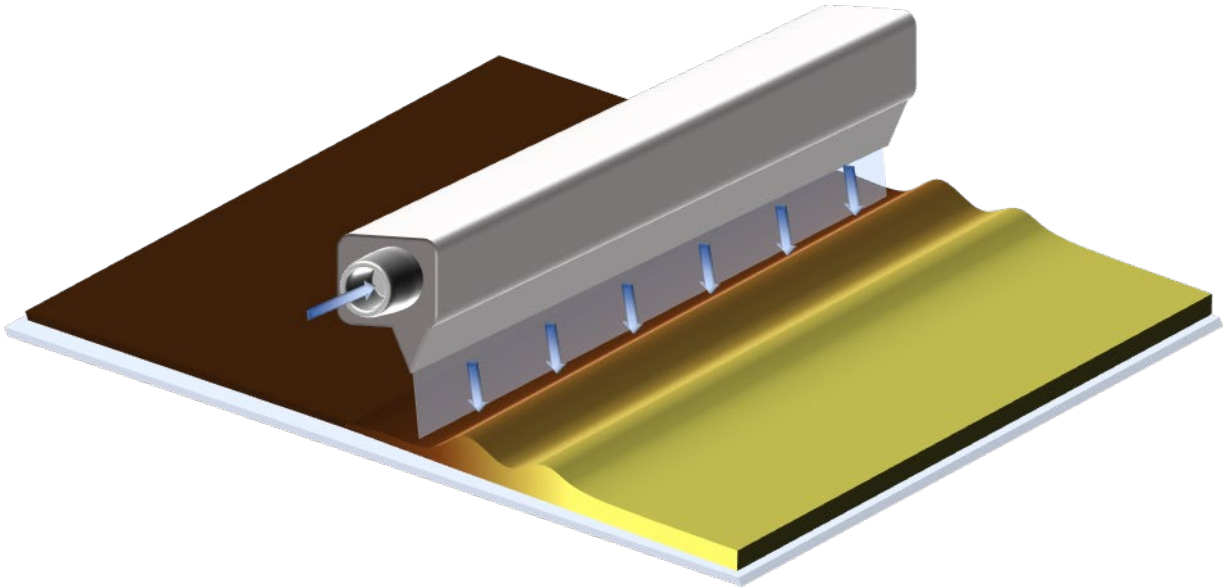


Figure 17: Illustration of forced laminar air flow drying of a perovskite thin film.

2.3.3 Annealing

Thin-film synthesis typically involves a thermal annealing step to convert from precursors to final material phases, to obtain the desired crystalline phase, or to improve

materials structural/electrical properties. Conductive thermal annealing, the primary annealing method in PSC fabrication, is not suitable for roll-to-roll due to lengthy annealing times and/or large production line requirements.³² Convective ovens are the natural substitute, however, they too face the same challenges. As an illustration, if a roll-to-roll line with a web speed of 30 m/min had a dwell time of 10 minutes, then it would need a 300 m oven.

The consequences of such extended web length in a roll-to-roll line are not only limited to increased footprint and cost but can also negatively impact yield through elevated web tension demands and misalignment issues. A drawback of using a convective oven for plastic substrates is the need to maintain the operating temperature below the temperature at which the plastic would undergo deformation under tensile stress. The combination of these stressors can severely negatively impact conductivity of the TCO layer on top of the plastic where an increase in surface resistivity of 40 ohm per square can decrease efficiency by 70%.^{212, 213} It is evident that advances are necessary in the realm of scalable annealing techniques for PSCs..

Radiative thermal processes have been utilized extensively in roll-to-roll manufacturing for drying, annealing, and sintering applications. Belt infrared (IR) furnaces have been used for several decades in the manufacture of silicon solar cells, where thick films are dried, polymer binders are decomposed and metal materials are sintered.²¹⁴ IR heating elements, capable of rapidly reaching temperatures exceeding 800 degrees Celsius and featuring high processing speeds of several meters per minute, have been adapted for implementation in roll-to-roll production processes. These elements have been successfully utilized to demonstrate the feasibility of high-throughput sintering

of metal on polymer substrates.²¹⁵ Similarly, the use of microwaves has also been adapted to sintering metals on polymer substrates.²¹⁶ The use of radiative techniques, such as IR heating and microwave heating, has been shown to reduce dwell times in comparison to traditional convection ovens.

RTA is a manufacturing process which provides a way to rapidly heat samples to high temperatures on a short timescale using high intensity near-IR light sources. This process was primarily utilized in the manufacture of semiconductors, but has recently been explored for the manufacture of perovskites. Ouyang et al. observed a significant decrease in overall processing time, with a reduction of an order of magnitude, when compared to hotplate annealing methods.²¹⁷

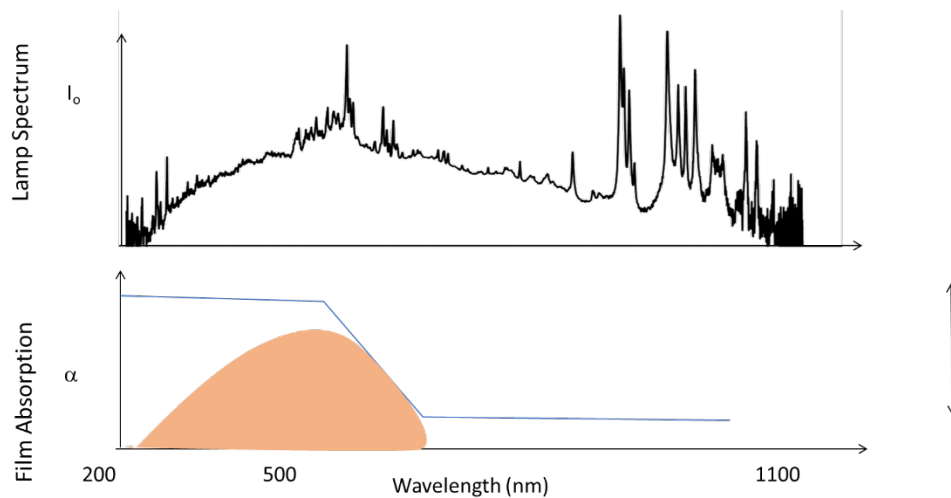


Figure 18: (top) Emission profile of the IPL lamp showing intensity as a function of wavelength from the Xenon source material. (bottom) Illustration of an absorption profile of a visible light absorbing film, with the shaded region highlighting the amount of energy absorbed by the film.

The IPL process involves the absorption of light energy from a broad-spectrum, rapid pulse emitted by a xenon bulb onto a thin film, as shown in figure 18. The use of a thin film with high absorptivity within the IPL spectrum allows for the absorption of

radiative energy and its rapid conversion into thermal energy. This process results in the uniform irradiation of a relatively large surface area, making it suitable for the heating of large-area PSCs. IPL lamps can be tuned to utilize energies spanning the UV, visible, and into the IR regions. The technology has been utilized in processing polymers, metals, metal oxides and semiconductors since the 1970's but recently has found industrial applications for materials in PVs.^{218, 219} Two advantages of IPL are short processing times and compatibility with low heat-tolerant, transparent substrates.

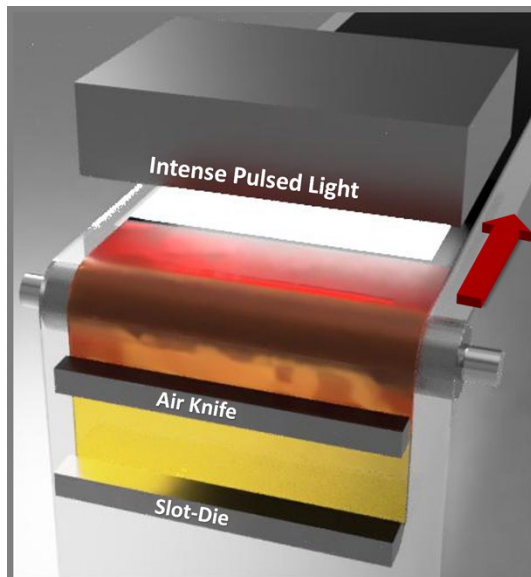


Figure 19: Schematic of the processing of the individual layers of the perovskite device by slot die deposition, air knife drying and IPL annealing. Flexible plastic is depicted as the substrate for the devices. The fabrication process for a single layer, from start to finish, has been demonstrated in a 2 m length of the process path.

The IPL process has been established for films of interest to the PSC with several research groups demonstrating the process in manufactured devices with efficiencies of over 16%.¹⁰¹ Figure 19 illustrates a hypothetical roll-to-roll manufacturing platform utilizing IPL. Table 4 shows the range of IPL processing parameters used on various thin

films including the transport layer, perovskite layer, and metal contact. Additionally, the IPL process has been demonstrated on multiple layers for a single perovskite device.²²⁰

The stability of organometal halide perovskite films is known to be compromised upon exposure to ultraviolet (UV) radiation. However, a study was conducted to assess the effect of exposure to intense pulsed light (IPL) lamps. The results of the study showed no significant change in photovoltaic (PV) performance after exposure to IPL. This outcome was attributed to the low irradiance in the UV spectrum and the brief duration of the exposure.²²¹

Table 4: Examples of IPL processing of thin films used in PSCs from literature.

Layer	Energy Density (J/cm ²)	Pulse Duration (μs)	Number of Pulses	Substrate	PCE (%)	Ref
TiO ₂	12.3	2000	10	Glass	16.7	222
				PEN	12.3	
TiO ₂	17.3	2000	5	PET	8.1	144
SnO ₂	11.7	2000	5	Glass	12.0	220
SnO ₂	4.6	2000	10	Glass	15.3	223
MAPbI ₃	25	2000	5	Glass	16.5	101
MAPbI ₃		1150	1	Glass	11.3	224
MAPbI ₃				Glass	8.9	225
MAPbI ₃	0.89-1.78	1125-1982	6	Glass	11.75	226
MAPbI ₃	33	2000	1	Glass	12.3	227
MAPbI ₃	8	2700	1	Glass	NA	228
MAPbI ₃	6.9	20000	1	Glass	11.26	221
MAPbI _{3-x} Cl _x	3.99	250	1	Glass	11	224
Triple Cation		2000	1	Glass	12.0	220
MAPbI ₃	6.8			Glass	15.04	102
MAPbI ₃		20000	1	Glass	11.42	229
Mixed Cation PVSK and SnO ₂				PET	18.8	230
Cu	20.1	2000	1	PET	NA	231

Cu	8	2000	3	PET	NA	²³²
Ag	1.75	500	1	Polymer	NA	²³³

The first reported application of IPL processing on perovskite materials was conducted on a sequentially deposited PbI_2 and methylammonium iodide film, resulting in a significant phase transition from cubic particles to a dense perovskite film.²²⁷ It was observed that IPL provided better penetration of the mesoporous TiO_2 . Although the higher energy densities led to improved crystallization, excessive energy or prolonged pulses lead to thermal degradation to the perovskite films.^{221, 224} The duration of the pulse has also been shown to influence the crystallization of perovskite materials, with longer pulses resulting in larger grain sizes, surpassing those obtained through hot plate annealing.²²¹ The best outcomes in IPL annealing of perovskite materials are obtained when there is visible light absorption in the transitional stage (referenced later in figure 28), emphasizing the importance of cohesive coordination throughout deposition, drying, and annealing stages.

CHAPTER 3 – EXPERIMENTAL METHODS

3.1 Techno-economic analysis, roll-to-roll production of PSCs via radiative thermal processes.

A detailed, bottom-up techno economic model was developed which calculates the COGS for roll-to-roll solar cell manufacturing only. The completed product in this example is fully operational interconnected solar cells sandwiched in a plastic roll that is ready for integration into a module. The form factor of the modules will require another manufacturing platform similar to current manufacturing in silicon panel manufacturing. The complete model is provided in the spreadsheet “COGS” available in Appendix 2. This spreadsheet includes separate tabs for the following: a list of assumptions, costs for materials, equipment, utilities and labor.

A Monte Carlo simulation is used to estimate uncertainty in cost projections for materials, utilities, labor, maintenance, and equipment. The simulation utilized a random number generator parametrized to a stationary probability distribution assuming 10% standard deviation from the initial price projections at 1 GW, 2 GW, 3 GW, and 4 GW production rates. The simulation discretely calculated costs for each component in ink formulations (PbI₂, ethanol, DMF, chlorobenzene, etc.), ITO/PET substrate, labor, utilities, maintenance, and depreciation. The data was generated from 10⁵ Monte Carlo steps. The full data set for the Monte Carlo analysis is included in the COGS spreadsheet.

3.1.1 Assumptions

The assumptions in the model are related to the factory and final product performance. For this analysis the module PCE is 18%, the factory uptime is 85% and the product yield is 90%. The other assumptions related to utilities, labor and equipment for the model are covered in the appropriate sections.

3.1.2 Materials Costs

The cost of raw materials for an industrial roll-to-roll process typically consume a large portion of the COGS. As demand causes a material to transition from specialty to commodity, the price of the material decreases. Some of the chemicals used during PSC fabrication are specialty chemicals. It is common knowledge that the price of a chemical decreases when the production rate increases based upon various factors such as reduced overhead and increased efficiencies. To accurately project the prices of these chemicals at scale, a rate of consumption is required for each raw material and it is assumed that material contracts will be based on yearly consumption, a standard practice in high volume manufacturing.

A simple means to effectively forecast the cost of a bulk material is to apply a power law relationship²³⁴

$$P = aQ^b \quad (29)$$

where P is the forecasted price (\$/unit), a is the cost of a single unit (\$/unit), Q is the quantity of material and the exponent b is the index of learning. It is often easier to relate b to the learning rate by the equation $LR=1-2^b$, where LR describes the percent reduction in cost for every doubling of product produced. In this analysis, quotes were obtained at varying scales and a learning rate computed from this data. The quoted costs for the

materials, learning rates, a and b for each of the materials is located in the “Learning Rate” tab. The unit price for each of the materials is tabulated at yearly production rates between 500,000 to 50,000,000 m²/year. The cost of the ITO coated PET is a key driver in the cost analysis and was therefore evaluated at three learning rates.

3.1.3 Equipment and Facilities Costs

The equipment costs in this model were quoted from several different manufacturers and were sized for a 1.5 m wide web operating at speeds up to 40 m/min. These costs are detailed in the “Equipment” tab. A flat rate of \$1,000 per m² was used for warehouse space, and \$10,000 per m² for the manufacturing space which includes costs for installation of equipment, plumbing, electrical, etc. Straight line depreciation was used for the equipment and facilities, using a 10-year and 20-year depreciation respectively, and a 5% salvage value was used for the equipment. The estimation of the facilities footprint includes the space required for equipment, inbound materials, and finished product storage. A yearly maintenance rate of 4% was assumed for each piece of the equipment.²³⁵

The individual equipment specifications have been designed to run at speeds up to 40 m/min as a single line, but to improve the robustness of the analysis, the plant is modelled to operate at web speeds of 10 m/min. This also allows for alternative factory configurations such as separating depositions into four separate roll-to-roll lines or running the lines at 40 m/min resulting in a lowered capital expenditure (CAPEX)

3.1.4 Utility Costs

The cost of utilities are estimated for each of the thin film layers and includes the deposition, drying, and annealing of the inks. For each process, the energy required to pump ink, move air for drying, and pulse the IPL was converted to electrical energy.

Electricity cost of \$0.0999 per kW-hr was assumed for this analysis, which is the average cost of electricity for the year 2020 worldwide.²³⁶

3.1.5 Labor

A major advantage of a complete in-line, roll-to-roll manufacturing process is that there is limited handling during the process. The labor required is mainly associated with loading materials (substrates and inks) as well as equipment maintenance and other in-process adjustments. For this calculation, it is assumed that two operators will be used to load/unload PET rolls, one operator for each coating station, quality assurance (QA) and maintenance personnel and a supervisor for a total of 9 operators per shift on the line. Table 5 details the position and assumed hourly wage according to the Bureau of Labor Statistics. An overhead rate of 50% is used to account for personnel not directly involved in the COGS, such as engineers, purchasing agents, management and etc.

Table 5: Labor assumptions for 1 GW production line used in this techno-economic analysis

Position	Position Code	Number	Mean Hourly Wage
Supervisor	17-2112	1	\$44.55
Prepress Technician	51-5111	2	\$20.45
Printing Press Operator	51-5112	4	\$18.80
Maintenance	49-9040	1	\$26.60
QA	19-2031	1	\$40.46

3.2 Fabrication of Flexible PSCs via RTA

3.2.1 Device fabrication

Materials match the items purchased in [10]. The device architecture used is as follows:

PET/ITO/PTAA/PFN/PVSK/C₆₀/BCP/Ag. The precursor perovskite ink consisted of 1.2M MAI, 1.2 M PbI₂, and 0.06M methylammonium chloride (MACl) in mixed solvent (DMF/DMSO/NMP = 0.91:0.07:0.02 v/v/v). Further details about deposition of PTAA, poly[(9,9-bis(3'-(N,N-

dimethylamino)propyl)-2,7-fluorene)-alt-2,7-(9,9-dioctylfluorene)] (PFN), C60, BCP, and Ag can be found in [10].

3.2.2 RTA of perovskite thin films

RTA conducted in a commercial Ulvac MILA-3000 minilamp annealer.

Temperature profile ramped to 50°C, held for 3 seconds, ramped to 75°C, then shut off.

Perovskite thin films were treated with a laminar airflow, to promote supersaturation, followed by RTA. Conductive annealing was performed on a hotplate. All anneals were performed at <19% relative humidity air.

X-ray diffraction (XRD) patterns were measured by a Bruker D8 Discover X-ray diffractometer. Top-view scanning electron microscope (SEM) images were recorded using a JEOL 7000 field-emission SEM. J–V curves were measured by a Class AAA solar simulator with a Xe-arc lamp and AM1.5G filter from PV measurement.

Illumination intensity was calibrated with an NREL-certified Si reference cell.

3.3 IPL-annealed mixed cation perovskites with robust coating window towards scalable manufacturing of commercial PSCs

Materials

Unless noted otherwise, all materials were purchased from Sigma Aldrich without further purification. PbI₂ (99.99%, trace metals basis) for perovskite precursor was purchased from TCI Chemical. N,N-Dimethylformamide (DMF, 99.8%) and Diiodomethane (CH₂I₂, 99%) were purchased from Alfa Aesar. Methylammonium iodide (MAI), formamidinium iodide (FAI), and methylammonium bromide (MABr) were purchased from Greatcell Solar. Ag pellets (99.999%) were purchased and Kurt J. Lesker Co.

3.3.1 Device Fabrication

ITO-PET substrates (VDI LLC, 50 ohm/in²) were cut into 6"x8" pieces, cleaned with isopropyl alcohol (IPA), then dried with a N₂ air gun. Substrates were treated with UV-Ozone treatment for 15 minutes immediately before sequential deposition of poly[bis(4-phenyl)(2,4,6-trimethylphenyl)amine (PTAA), PFN, perovskite, and SnO₂ via blade coating under a humidity-controlled atmosphere (RH ~15-30%).

3.3.1.1 HTL

60 µL PTAA solution (8mg/mL in toluene) was blade coated with a blade gap of 100µm at a coating speed of 10 mm/s then heated at 100°C for 10 min. 60 µL of PFN (0.4 mg/mL in methanol) was blade coated with a blade gap of 100 µm at a coating speed of 10 mm/s.

3.3.1.2 Perovskite ink

Perovskite solution prepared by measuring 0.461 g PbI₂, 0.080 g MAI, 0.068 g FAI, 0.015 g MABr, and 0.003 g PEAI. These powders were then dissolved by addition, in sequential order, 400 µL 2-ME, 600 µL ACN, 60 µL NMP, 38 µL CH₂I₂, 19 µL dichloromethane (CH₂Cl₂). 70 µL of the perovskite solution was blade coated with a blade gap of 150 µm at a coating speed of 10 mm/s. The film is dried ~1 second after deposition via an air knife installed ~1" from the blade edge (Air knife pressure set to 10-15 psi).

IPL annealing was conducted using Xenon S-2210 High-Energy Pulsed Light system with LH-150 lamp housing with a height-controlled stage underneath lamp aperture. For hotplate-annealed samples, the film post drying is transported directly to a hotplate (~5-10 seconds). For IPL-annealed samples, the film post drying is transported to our IPL, height from IPL aperture is set to 6", then the film is irradiated (30–60 seconds).

3.3.1.3 ETL

60 μL of SnO_2 solution (2% in anhydrous EtOH) was deposited on perovskite with a blade gap of 100 μm at a coating speed of 10 mm/s then annealed at 100°C for 2 to 3 min.

3.3.1.4 Thermal Evaporation – BCP and Ag

5 nm of BCP and 100 nm of Ag were thermally evaporated through a 0.1 cm^2 shadow mask. The final device architecture is PET-ITO/PTAA/PFN/Perovskite/ SnO_2 /BCP/Ag.

3.4 JV Characterization

JV curves were obtained using an Autolab PGSTAT128-N potentiostat and a height-controlled superstrate simulator equipped with an AM 1.5G filter from a Newport LCS-100 lamp with irradiance set using a KG-3 filtered Si diode calibrated by the National Renewable Energy Laboratory.

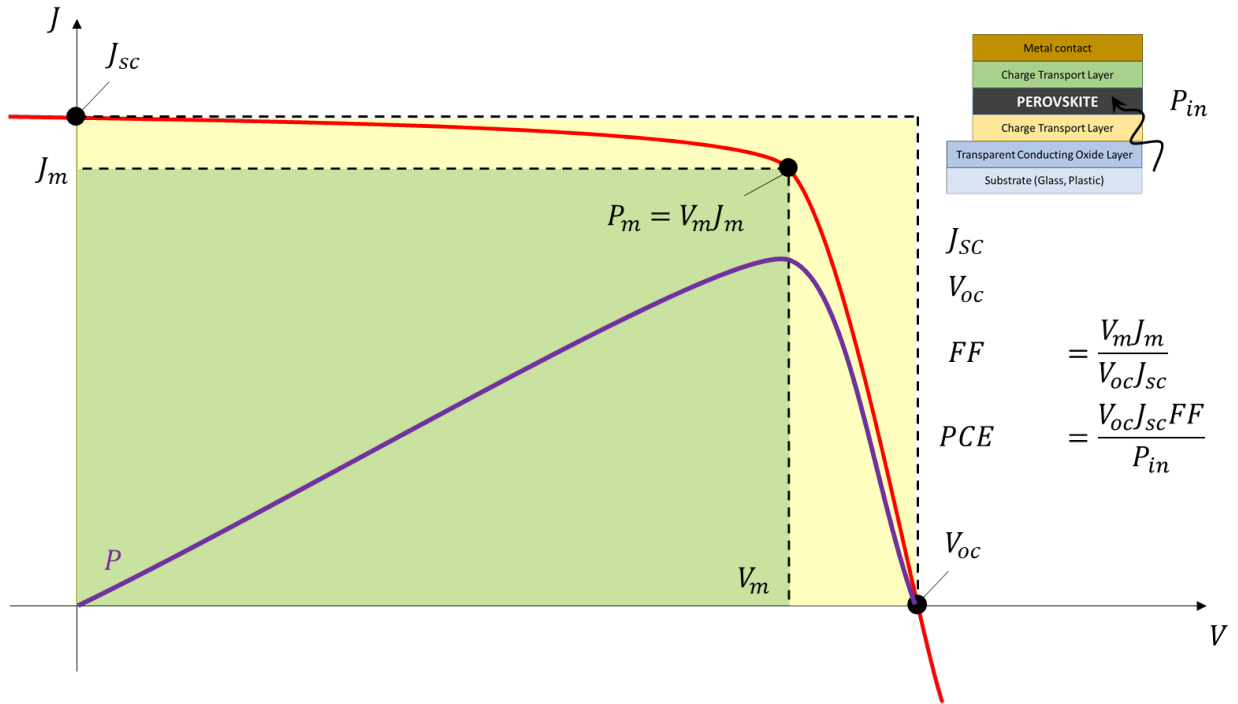


Figure 20: An example of a JV Curve for a solar cell device under test, highlighting the relevant parameters of J_{sc} , V_{oc} , FF, and PCE. Device schematic in the upper right corner represents a cross-sectional perovskite solar cell under illumination.

Linear sweep voltammetry is a critical characterization tool in PVs, delivering the short-circuit current density (J_{sc}), open circuit voltage (V_{oc}), fill factor (FF), and PCE. Linear sweep voltammetry is run by a potentiostat that measures current as the potential is varied linearly at predetermined step sizes. The resulting IV curve is the superposition for the IVE curve of the solar cell diode in the dark with the light generated current.²³⁷

The short-circuit current density (J_{sc}) is the maximum current that may be drawn from the solar cell and occurs when the applied voltage across the cell is zero. For an ideal solar cell with less than or equal to moderate resistive losses, the short-circuit current density and light-generated current density are identical.

Solar cells are also characterized by their open circuit voltage (V_{oc}). This is the maximum potential difference a solar cell can have and is measured when there is zero current density of the solar cell. It can be described as:

$$V_{oc} = \frac{nkT}{q} \ln \left(\frac{J_L}{J_0} + 1 \right) \quad (30)$$

in which k is the Boltzmann's constant, T is the temperature, q is the electronic charge, J_L is the light-generated current density, and J_0 is the dark saturation current density.

Multiplying the voltage by the current density gives the power density. The maximum power point is the solar cell's maximum operating power and is used to calculate the fill factor (FF) which describes the squareness of the J-V curve and is used to describe losses in efficiency. The fill factor is defined as:

$$FF = \frac{V_M J_M}{V_{oc} J_{sc}} \quad (31)$$

where J_m and V_m are the current and voltage generated at the maximum power point respectively and J_{sc} and V_{oc} are the short circuit current density and open circuit voltage, respectively.

The efficiency of the solar cell is then related to the fill factor by:

$$\eta = \frac{V_{oc} J_{sc} FF}{P_{in}} \quad (32)$$

where η is the efficiency, J_{sc} is the short circuit current density, V_{oc} is the open circuit voltage, FF is the fill factor, and P_{in} is the incident light power density. The Standard Test Condition (STC) for solar cells is the Air Mass (AM) 1.5 spectrum with an incident

power density of 1000 W/m² and a temperature of 25 °C. The AM 1.5 spectrum corresponds to the sun being at an angle of elevation of 42°.

3.5 UV-Vis Spectrometry

The optical properties of “wet”, transitional, and “dry” perovskite films were analyzed using UV-Vis spectrometry. UV-Vis measurements were collected using a PerkinElmer Lambda 950 UV-Vis spectrometer.

3.6 X-Ray Diffraction (XRD) measurements

Perovskite crystallinity and phases were studied using a Bruker AXS D8 Diffractometer equipped with a position sensitive detector and X-ray source of CuK α (λ = 0.1548 nm). XRD patterns were measured at scan speeds of 2 s/step. Step size of 0.02°, and a 2 θ range from 7-60°.

3.7 Scanning Electron Microscope (SEM)

Scanning electron microscopy (SEM) images were taken using a FEI Nova NanoSEM 600 with an accelerating voltage of 1.5 kV and a working distance of 5-6 mm.

3.8 Nomenclature

PV	photovoltaic	c-Si	crystalline silicon
PCE	power conversion efficiency	PSC	perovskite solar cell
LCOE	levelized cost of energy	CdTe	cadmium telluride
GaAs	gallium arsenide	CIGS	copper indium gallium selenide
VNCS	volatile non-coordinating solvents	IPL	Intense Pulsed Light
DSSC	dye-sensitized solar cells	TCO	transparent conducting oxide
FTO	fluorine-doped tin oxide	ITO	indium-doped tin oxide
HTL	hole transport layer	ETL	electron transport layer
CTL	charge transport Layer	MAPbI ₃	methylammonium lead triiodide
MAI	methylammonium iodide	FAI	formamidinium iodide
ΔG_{mix}	Gibbs free energy of mixing	Cs	cesium
Br	bromine	I	iodine
PEAI	phenethylammonium iodide	CH ₂ I ₂	diiodomethane

Pb	lead	HOMO	highest occupied molecular orbital
NiO _x	nickel oxide	MoO ₃	molybdenum oxide
PTAA	poly[bis(4-phenyl)(2,4,6-trimethylphenyl)amine]	r	radius of a particle
γ	surface energy per unit area	ΔG_v	free energy per unit volume of a crystal
k_B	Boltzmann's constant	μ	surface chemical potential on the surface
DMF	dimethylformamide	DMSO	dimethylsulfoxide
NMP	N-methyl-2-pyrrolidone	DMA	N,N-dimethylacetamide
GBL	γ -butyrolactone	D _N	Gutmann's donor number
IR	infrared	GW	gigawatt
TiO ₂	titanium dioxide	ZnO	zinc oxide
PET	polyethylene terephthalate	CAPEX	capital expenditure
t _{wet}	wet film thickness	ρ_s	density of solids
ρ_l	density of liquids	%s	percent solids by volume
Δp	pressure drop (slot die)	\dot{V}	volumetric flow rate (slot die)
L	land length (slot die)	l	Slot length (slot die)
a	gap width (slot die)	\dot{m}_{evap}	rate of solvent mass evaporated (drying)
A _{film}	Film surface area (drying)	h _m	convective mass transfer coefficient (drying)
$\rho_{A,S}$	Mass density of solvent vapor at film surface (drying)	$\rho_{A,\infty}$	Mass density of solvent vapor for from surface (drying)
ACN	acetonitrile	P _{blower}	power required by blower (drying)
\dot{m}_{air}	mass flow rate exiting air knife (drying)	v _{air,exit}	exit velocity from the air knife (drying)
η_{blower}	blower efficiency (drying)	C _{p,air}	specific heat of air (drying)
τ_{dry}	Time to dry (drying)	V _{web}	speed of the web (drying)
L _{dry}	distance traveled before dried (drying)	E _{dry}	energy requirement per film area (drying)
QA	quality assurance	BCP	Bathocuproine
MACl	methyammonium chloride	PFN	poly[(9,9-bis(3'-(N,N-dimethylamino)propyl)-2,7-fluorene)-alt-2,7-(9,9-dioctylfluorene)]
MABr	methyammonium bromide	XRD	X-ray diffraction
SEM	scanning electron microscope	CH ₂ Cl ₂	dichloromethane
J _{sc}	short circuit current density	V _{oc}	open-circuit voltage
FF	fill factor	TW	terawatt
MW	megawatt		

CHAPTER 4 – TECHNO-ECONOMIC ANALYSIS

4.1 Introduction

This chapter describes a technoeconomic analysis of the cost benefits of manufacturing PSCs at GW-scale, utilizing innovative IPL annealing techniques. The analysis takes into account the potential cost savings that can be achieved through economies of scale and the utilization of rapid annealing. It considers the cost of goods sold (COGS) for a roll-to-roll manufacture of perovskite films referencing the flow chart in figure 21. Application of fundamental engineering and economic analyses of materials and energy inputs details cost of materials, utilities, labor, and equipment for IPL annealing. The analysis operates under the assumption that solution-phase depositions are carried out in three stages: deposition (slot die), drying (air knife), and annealing (IPL).

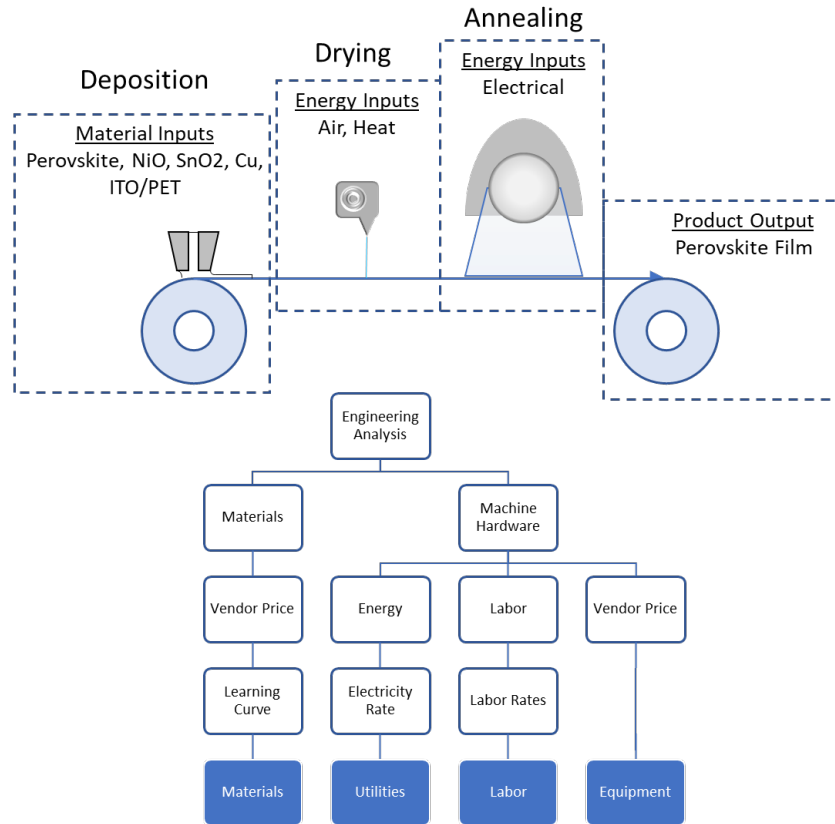


Figure 21: Flow chart explaining the overall methodology of the techno-economic analysis. The process under investigation includes the deposition, drying and post-processing using IPL of the four layers (SnO₂, perovskite, NiO and Cu). A fundamental engineering analysis of each process informs the design of the equipment, utilities and labor. All of these including the material inputs are considered for the overall roll-up of the cost of goods sold.

3.3.1 Slot Die

The deposited wet layer thickness (t_{wet}) that is related to the percent solids by volume (%s), dry thickness (t_{dry}), and ratio of the density of solids (ρ_s) to solvent (ρ_l) per equation 33.

$$t_{wet} = \frac{t_{dry} \rho_s}{\%s \rho_l} \quad (33)$$

A coating thickness of 50 nm to 500 nm can be achieved using a slot die combined with very dilute solutions. Thus, the viscosities of the coating solutions are

small, resulting in a very low pumping head requirement. Estimation of the pumping power is a very straightforward application of planar Poiseuille flow where the pressure drop across the slot die is determined by:

$$\Delta p = \frac{12\dot{V}\mu L}{a^3 l} \quad (34)$$

where \dot{V} is the volumetric flow rate, μ is the ink viscosity, L is the land length, a is the gap width and l is the slot length. The pumping power is the product of the volumetric flow rate and pressure drop. \dot{V} can be estimated from the wet film thickness (t_{wet}).

The inks used in the development of the thin films have viscosities on the order of 1-10 g/cm·s. Typical land lengths used in a slot die are approximately 25 mm with a gap width of 10-20 mm and the slot length covers the width of the web, which in this case is 1.5 m. The pumping power for the slot die is calculated in the “Utilities” tab.

3.3.2 *Drying*

In the drying analysis, the goal is to develop a tool to estimate the cost to evaporate the solvents used to produce the desired thin film. The options of evaporation methods have been narrowed to high velocity air jets/knives and heating the air jet stream. These two methods provide significant ability to tune the drying rate and temperature of the solvent surface. Several solvents that have been previously used in PSC fabrication were selected for the analysis. In the results section, the specific solvent is shown to have little impact on the final costs. Hence, specific solvents will not be specified in the analysis. The model developed allows for the estimation of the energy use involves the following simplifying assumptions: interaction of two solvents was not considered (modeled as the more volatile evaporates first and then second), evaporative

cooling effect on the liquid surface was not taken into account, diffusion of the solvent through the remaining solid layer is not considered, the heat and mass transfer analogy is valid (small solvent vapor concentration in the air), and the air is assumed to be dry. Several of these assumptions are supported by the thickness of the wet and dried films being very thin. Energy use for drying is calculated in the “Evaporation” tab.

The drying process involves an air jet blown over the solvent surface to reduce the boundary layer and enhance both convective heat transfer and mass transfer. Higher velocity and higher air temperature both provide enhanced evaporation. The outline of the solution method for the drying problem was to obtain a convective mass transfer coefficient. Correlations for impinging jets are found in literature^{210, 238}, and used to calculate an average convective heat transfer coefficient. The correlation for the array of slot jets accounts for the effect of air velocity and temperature exiting the jet, jet width, separation between slot jets, and height above the film surface. The heat and mass transfer analogy gives a relation between convective heat transfer and convective mass transfer and the resulting mass transfer coefficient was used to estimate the solvent evaporation rate. The mass transfer coefficient was used in equation 35 to solve for the rate of evaporation of the solvent per film area.

$$\frac{\dot{m}_{evap}}{A_{film}} = h_m(\rho_{A,S} - \rho_{A,\infty}) \quad (35)$$

where \dot{m}_{evap} is the rate of solvent mass evaporated, A_{film} is the film surface area, h_m is the convective mass transfer coefficient, and $\rho_{A,S}$ is the mass density of solvent vapor at the film surface and $\rho_{A,\infty}$ is the mass density of solvent vapor far from the surface. Both the vapor pressure and binary diffusion coefficient of the solvent play a role in calculating the evaporation rate. As an example, the vapor pressure at 25°C and binary diffusion

coefficient in air are given for a selection of solvents (Table 6, see below). Solvents with higher vapor pressures and diffusion coefficients are ones that evaporate more quickly.

Table 6: Binary diffusion coefficient and vapor pressure of selected solvents used in PSC manufacturing.

Solvent	Chemical Formula	Binary Diffusion Coefficient in Air (m ² /s) at 25°C	P _{vap} (Pa) at 25°C
ACN	C ₂ H ₃ N	1.30 x 10 ⁻⁵	11714
ethanol	C ₂ H ₅ OH	1.15 x 10 ⁻⁵	7869
water	H ₂ O	2.60 x 10 ⁻⁵	3141
chlorobenzene	C ₆ H ₅ Cl	7.30 x 10 ⁻⁶	1597
DMF	C ₃ H ₇ NO	9.74 x 10 ⁻⁶	529

The rate of energy required to dry the solvent layer due to kinetic energy added to accelerate air as it moves through a jet nozzle or air knife²³⁹ was calculated by assuming air is initially stagnant and accelerated to the nozzle exit velocity. A factor to account for the inefficiencies of accelerating air by a blower is included to account for the conversion of the electrical energy to the blower to kinetic energy in the air. The mass flow rate was calculated using the density of air, the exit velocity from the air slot jet/knife, and cross-sectional area of the slot jet knife exit. The power required by the blower is given below.

$$P_{blower} = \frac{\dot{m}_{air} \left(\frac{V_{air,exit}^2}{2} \right)}{\eta_{blower}} \quad (36)$$

where \dot{m}_{air} is the mass flow rate exiting the air knife, $V_{air,exit}$ is the exit velocity from the air knife, and η_{blower} is blower efficiency.

Evaporation rates can be increased by heating the air exiting the air knife. The equation to calculate the electrical power to heat the air is given.

$$P_{heater} = \dot{m}_{air} C_{p,air} (T_{air,exit} - T_{amb}) \quad (37)$$

Table 7: Concentrations of solvent in air at 10 m/min web speed (approximately 1 GW production).

Solvent	Mass/Area (g/m ²)	PPM solvent (steady-state)
water	2.29	6500
chlorobenzene	0.237	217
DMF	0.321	458
DMSO	0.093	123
ethanol	2.13	4750
1-methoxy, 2-propanol	24.1	2290

Of importance to the COGS analysis is the length to dry which impacts the footprint and the energy which impact the utilities. The time to dry the solvent layer, t_{dry} was calculated from

$$\tau_{dry} = \frac{m_s}{\dot{m}_{evap}} \quad (38)$$

where m_s is the mass of solvent applied for a given layer and \dot{m}_{evap} is the rate of solvent evaporation. For comparison between a volatile solvent (ACN) and less volatile solvent (DMF), the drying times for a 10 mm layer of solvent was calculated using the model as shown in Figure 22, for various air velocities over the wet surface and at two temperatures for the air blown over the surface. In this simple model, the evaporation rate is a constant value and models the situation for much of the drying process when the liquid solvent is the dominant species in the liquid layer and diffusion through the liquid layer is not a limiting factor.

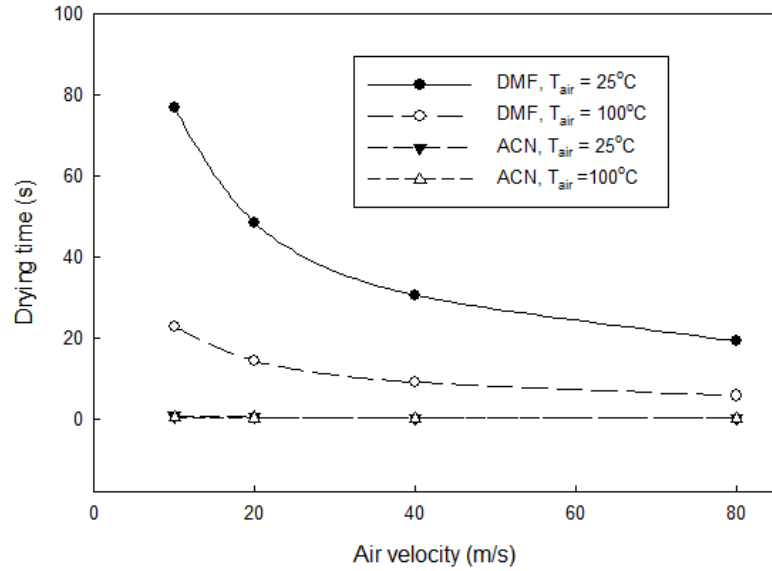


Figure 22: The drying time for a solvent thickness of 10 mm for DMF and ACN is shown as a function of air velocity over the film surface and for two air temperatures. This relationship is used to estimate drying for different solvent systems based on their physical properties.

The distance the film travels until it becomes dry is L_{dry} and calculated by

$$L_{dry} = \tau_{dry} V_{web} \quad (39)$$

where V_{web} is the web speed.

Finally, the energy requirement per film area required to dry a given layer, E_{dry} is calculated using:

$$\frac{E_{dry}}{A_{film}} = \frac{n(P_{blower} + P_{heater})\tau_{dry}}{L_{dry}W_{film}} \quad (40)$$

where A_{film} is the area of the film, P_{blower} and P_{heater} are the power requirements for the blower and heater (covered in the supporting information), n is the number of air knives used and W_{film} is the width of the film.

3.3.3 IPL

As discussed, the IPL process has been utilized on numerous thin films related to PSCs (Table 1) where the energy density per pulse varies between 2 and 20 J/cm², with lower pulse energy and counts required for polymer substrates. The energy requirements to adequately process these films are dependent on the type of substrate and properties of the film itself; however, not all electrical energy delivered to the lamps is absorbed by the thin films. Therefore the energy use and subsequent electrical costs for the IPL are measured as the energy input to the IPL.

The IPL technique requires less energy to thermally process films on a plastic substrate as opposed to a glass substrate due to the differences in thermal mass.²⁴⁰ The thermal response within films and underlying substrates due to IPL processing was analyzed using finite element analysis. In previous work, it was established that the energy required to anneal a perovskite thin film on a glass substrate was on the order of 10 J/cm² delivered over a 2 ms pulse.²⁴¹ From that analysis, the thermal response of the perovskite film exceeded 700°C for a short duration (Figure 23). At 3 mm thick, the glass substrates act as a large thermal mass effectively removing heat from the thin film. On the other hand, a plastic substrate 0.1 mm (4 mil) thick will result in temperatures in the film about 2.5 times as high and would destroy the film. Thus, lower energy is required to heat the perovskite thin films appropriately. Figure 23 demonstrates that different temperature responses may be produced by varying the pulse energy and duration to achieve desired annealing.

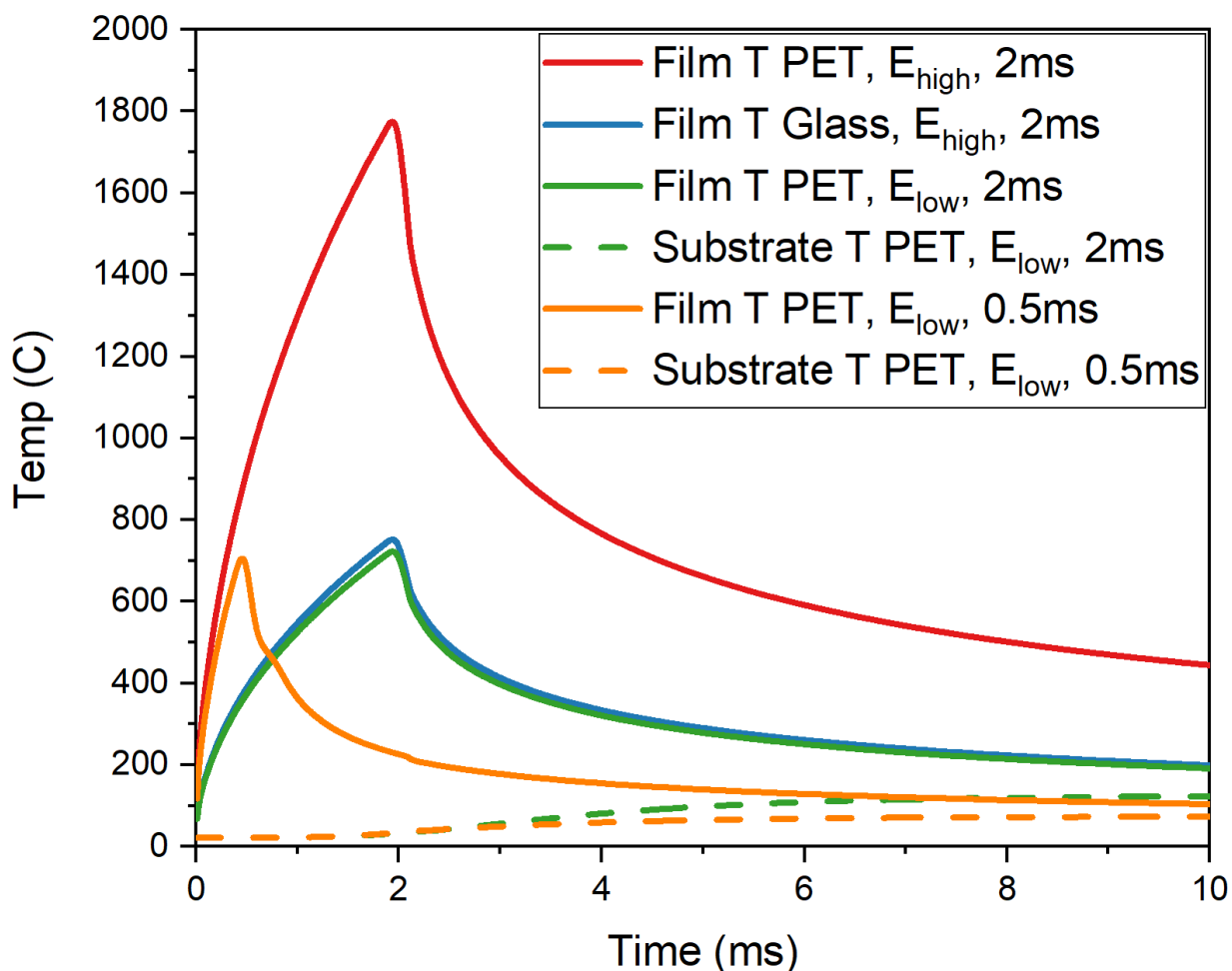


Figure 23: Comparison of thermal response to IPL intensity and pulse duration for two substrates. Solid lines denote temperature for the perovskite film and dashed lines for temperature in the substrate, either glass or PET. The legend denotes high (E_{high}) or low (E_{low}) pulse intensity and pulse length of 2 ms or 0.5 ms being applied.

Of concern is the ITO layer, which under strains of just a few percent will crack leading to a reduced conductivity.²⁴² The ITO layer is approximately 500 nanometer thick, which is less than one percent of the substrate thickness and despite the fact the Young's modulus is considerably higher than PET, the bulk of the applied load is carried by the PET substrate. Deformation within the PET substrate caused by the web tension can lead to crack deformation in the ITO. These defects are exacerbated as Young's

modulus for PET drops with increasing temperature. Therefore, it becomes important to further reduce the temperatures that the PET is subjected. This can be accomplished by reducing the combination of pulse strength and pulse duration, where similar peak temperatures within the perovskite film can be achieved with 0.5 ms pulse (Figure 23, orange line). The resulting temperature increase within the PET film is less than 100 °C, which should decrease the overall strain and limit damage to the brittle ITO.

It is possible that the IPL process may not be required for each layer individually. For example, the majority of the IPL energies lie below the band gap of SnO₂, the material chosen for the ETL. This yields an opportunity to anneal both films after deposition of the perovskite material. Additionally, since both the metal oxide layers are an order of magnitude thinner than the perovskite material, it may also be advantageous to use a single IPL process after the deposition of the HTL on top of the perovskite. However, the cost of equipment and energy use for the IPL process will be included for each of the layers for this analysis.

The estimation of the IPL parameters used in this analysis comes from previously published works, where the substitution of glass with PET reduces the energy required as discussed above. Thus, the energy densities are reduced to achieve similar thermal responses and multiple pulses are considered. Multiple pulses should improve the probability of consistently yielding highly crystalline perovskite material by maintaining an elevated temperature throughout the IPL procedure. Additionally, the total energy consumed by the lamps during IPL annealing is reduced when using multiple low-intensity pulses compared to a single, high-intensity pulse.²⁴³ Using multiple pulses also reduces variation in the films as the web continuously travels through the lamp and

minimizes the impact of irradiance non-uniformity. Finally, a shorter pulse duration as used for the analysis, will lead to a lower temperature within the substrate and less chance for degradation. Table 5 describes the intense light energy used for this analysis (note, the energy is given per unit film area).

Table 8: IPL conditions for the different layers in a roll-to-roll processed perovskite *PV* used for this techno-economic analysis.

Layer	Total IPL (kJ/m ²)	IPL per pulse (kJ/m ²)	# of pulses
SnO ₂	200	40	5
MAPbI ₃	35	12	3
NiO	81	20	4
Cu	90	30	3

4.2 Equipment Costs

The analysis was developed to compare the costs of implementing IPL as a viable thermal annealing processing step within a roll-to-roll manufacturing platform. The promise of roll-to-roll processing of solar cells is related to the throughput. Web speeds of over 100 m/min have been achieved within the film industry. At these achievable web speeds, a single tool could produce nearly one GW per month or the equivalent of a year's worth of production at a major c-Si manufacturing plant. Therefore, in order to establish the true opportunities for roll-to-roll manufacturing of PSCs, it is most advantageous to design roll-to-roll manufacturing capable of high production speeds. To establish the costs at scales above one GW, it was necessary to determine material costs at larger volumes and costs of appropriately sized equipment incorporating IPL, since previous analysis stop at one GW production.

Table 9: Equipment requirements for the Roll-to-Roll line per 1 GW production used in this techno-economic analysis.

Stations	Number required	Cost per item (\$M)	Equipment cost (\$M)	Web length per station (m)	Total line length (m)
Roll-to-roll (wind/unwind, controls, dancers, alignment, etc.)	1	0.62	0.62	5.0	5.0
Corona discharge	1	0.25	0.25	0.5	0.5
Slot die	4	0.35	1.40	1.0	4.0
Single/multi-array of air knives	4	0.10	0.40	1.0	4.0
IPL	4	3.00	10.5	1.0	4.0
Laser scribe	3	0.10	0.30	0.5	1.5
Lamination	1	0.25	0.25	5.0	5.0
Total	-----	-----	13.72	-----	24.0

The materials costs dominate and are 93.02% of the overall production cost as shown in Figure 24. The overall equipment costs are approximately one third of the processing costs. The overall costs of the equipment and web length for each piece of equipment required for the roll-to-roll deposition per one GW production line is tabulated in Table 7. It is estimated that the equipment cost per one GW production line is \$14M and that the total tool length is about 24 meters. The individual equipment specifications have been designed to meet a 4 GW production rate using a single line. Since these equipment costs are dwarfed by the materials costs, a single line will be used at 25% capacity for this analysis. This serves to improve the robustness of the operations by guaranteeing production rates as equipment fluctuations occur. Using this reduced production rate per line also allows for some leeway into the design of the manufacturing line, where it may be possible to design a layout in which a line is dedicated to a single

layer, requiring 4 lines. Or, one single station line composed of a slot die, air knife and IPL could be utilized to subsequently deposit and process each of the layers further reducing the floor space and startup costs.

For this analysis the evaporation is accomplished using a convective air knife and annealing is done using IPL. The drying and annealing of solution phase films have historically been accomplished in ovens that dominate the roll-to-roll manufacturing line. The replacement of these ovens with the air knife and IPL processes has the advantage of a much shorter web section, less equipment costs, and an overall shorter footprint. The evaporation by air knives for a single layer has been accomplished in less than 10 seconds and the IPL annealing process can be accomplished in less than 1 second.²⁴⁴ At a web speed of 10 m/min this would require an overall tool length of about 2 m. Most of the cost is associated with the IPL stations, making up 75% of the equipment costs. The cost of building the first IPL system was estimated adapting multiple S-2210's from Xenon Corporation that typically sell for \$105k each. Engineering and testing charges would bring the selling price for the first system to \$3 million. The IPL equipment has been established in high speed UV-curing in the DVD industry for example; however, some engineering work to adapt it to the high speed wide area roll-to-roll application proposed here will be required. A typical linear lamp spanning the 1.5 meter width of the web would process approximately 25-50 mm in the down web direction per pulse. Adding multiple lamps and engineering the optics of the lamp housing would increase the per pulse processing area. Judicious design of the optics can yield a non-linear increase in per pulse area, for example 4 lamps can increase the area by a factor of 8. This would serve to reduce the total number of lamps required and yield lamp frequencies that can be

supported by capacitor discharges. The process should be designed such that moving web is exposed to 3-5 flashes per unit area, which will decrease the stitching. A fair amount of engineering is required in the initial systems to design a robust system that matches the operational requirements for the process. As more lines are added to the manufacturing plant, this equipment becomes more standardized and the costs would be expected to drop. However, these costs are still less than a typical oven that can cost between \$10-\$20M dollars.

Assuming that the web is 1.5 m wide and allowing for 2 m on either side of the web, the total manufacturing footprint is approximately 108 m² and rounding up, four lines would require ~500 m². Applying a cost of \$10,000 per m² for manufacturing space results in a cost of \$5M. The estimate of \$10,000 per m² for manufacturing space is on the high side but has little impact on the overall COGS. To estimate the storage footprint, it is assumed that one month of inbound and outbound materials storage will be maintained. The required storage space is estimated at 10,000 m² at a cost of \$1,000 per m². The building, as expected, is dominated by space for storage of materials. The total cost for manufacturing and storage space yields an estimated cost of \$15 M.

A 4 GW production plant would have a total cost of \$71M, or about \$18M per 1GW production. A 4 GW plant size is an arbitrary choice but was chosen as this is where the COGS curve becomes relatively flat. In comparison the cost of a c-Si solar cell facility is estimated at \$120M for 1 GW yielding a significant cost savings using a roll-to-roll manufacturing process.²⁴⁵

4.3 Utilities

To make a comparison of the utility requirements for traditional ovens to IPL it is necessary to compute the energy requirement of the traditional oven. The main considerations for this calculation are the energy to heat the material, the energy to maintain safe processing and the losses through the insulation.

Substrate

The calculation of the heat required (\dot{Q}) to heat a substrate is simply:

$$\dot{Q} = \dot{m}C_p\Delta T \quad (41)$$

where \dot{m} is the mass flow rate of the substrate, C_p is the heat capacity of the substrate and ΔT is the change in substrate temperature. At a 1 GW production, the speed of the web is 10 m/min and using a 1.5m wide and 4 mil web the volumetric flow rate (\dot{V}) is 2.5×10^{-5} m³/sec. The density of PET is assumed to be 1200 kg/m³ yielding \dot{m} 0.0035 kg/sec. The oven temperature is assumed to be at 100 °C, and the ambient temperature 25 °C, to yield a ΔT of 75 °C. This yields a \dot{Q} of 3.1 kW. The substrate must also be cooled back to this temperature before the next deposition, so the overall heat transfer to the substrate is 6.2 kW.

Airflow

Sufficient airflow is required to maintain safe operation of the ovens. The National Fire Protection Association has placed a limit of solvent in a continuous operational oven at 25% the lower explosion limit (LEL). The LEL for the solvents used in analysis range between 1.6 and 3.3. Converting the LEL to a concentration (C) is done as follows:

$$C = \frac{LEL * 10,000}{MW} 24.45 \text{ ml/mmole} \quad (42)$$

The multiplication of the LEL is to convert it to ppm and MW is the molecular weight of the solvent in mg/mole. The mass of solvent per m² added is found in the spreadsheet and the mass rate multiplied by the web area speed 0.25 m²/sec (\dot{m}_{sol}). The determination of the volumetric flow rate of the air (\dot{V}_{air}) is:

$$\dot{V}_{air} = \frac{\dot{m}_{sol}}{0.25 \cdot C} \quad (43)$$

This \dot{V}_{air} can then be applied to equation 35 using a density of 1.275 kg/m³, a heat capacity of 1 kJ/kg and a DT of 75 °C.

The deposition of the first layer has been assumed to be a water based dispersion, and in this case an LEL is not an issue. However, in an operational plant, the RH of the exhaust stream should be less than the saturation density (r_{sat}). Assuming again that the outside temperature is 25 °C, the r_{sat} of air is 23.8 g/m³. Assuming that the plant is operating in a high humidity environment of 60%, then the maximum RH of the additional water should be less than 40%. This places a limit of 9.52 g/m³ of additional water added. The mass of water can be found in the spreadsheet.

Table 10, see below lists the details of the calculation of the heat added in the airflow stream.

Table 10: Air flow heat calculation for each layer.

	Solvent	LEL (%)	Max C (g/m ³)	Airflow (m ³ /sec)	Heat (kW)
SnO ₂	Water	NA	9.52	0.35	33.5
MAPI	DMF	2.2	1.84	0.58	55.7
NiO	CB	3.3	4.38	0.22	21.5
Cu	PM	1.6	1.09	10.4	995

Losses

The losses from the oven (\dot{Q}_{loss}) are computed by:

$$\dot{Q}_{loss} = UA\Delta T \quad (44)$$

where the U-value is the thermal conductivity (k) divided by the thickness (t) of the insulation, is the A is the surface area of the oven, and DT is the same as above. A k of 0.025 W/m²-K and a t of 50 mm is assumed for the insulation. The surface area of the oven is assumed to be 300 m² (dwell time of 10 minutes at 10 m/min and web width of 1.5 m). This results in losses of 11.25 kW.

The overall utilities costs in this analysis are approximately 13% of the non-materials costs (see Figure 24). The IPL annealing represents more than half but is still less than \$0.01 per m². The energy requirement for the IPL to process the perovskite layer is estimated to be 0.01 kW-hr/m². In comparison, at 1 GW, the energy consumption is 0.119 kW-hr/m² using a conventional thermal oven (see supplementary information for details). Table 7 compares the energy consumption of the IPL and traditional ovens for each of the thin film layers. There is clearly an advantage in the energy costs when using the IPL over a traditional oven. The biggest cost savings is from the exhaust requirements for the solvents being used. Remediating the exhaust containing solvents is required for both processes, but for the traditional oven, the airflow supplied to the oven must be heated and is a relatively significant utilities cost. The layer that does not show a difference in utilities is SnO₂ layer. Water, the solvent used in this layer, will require a

lower air flow rate; however, even in this case it would be expected that some air flow is necessary to keep the exhaust flow from being saturated.

Table 11: Comparison of energy usage per layer using IPL vs. traditional oven annealing based on the results of the techno-economic analysis.

Layer	IPL (kW-hr/m²)	Oven (kW-hr/m²)
SnO ₂	0.056	0.056
MAPbI ₃	0.010	0.119
NiO	0.022	0.043
Cu	0.025	0.388
TOTAL	0.113	0.607

The energy savings of the IPL process provides a significant cost savings (> 80%) associated with the annealing step. This savings along with the shorter web length in the annealing step will also affect the overall operating expenditures of manufacturing. Long web sections affect the yield through breakage and misalignment, both of which will increase the labor to deal with the associated downtime.

4.4 Total Costs

The cost of roll-to-roll production of the perovskite modules in this analysis does not include the final stages of manufacturing that would include the encapsulation of the module, framing and or addition of the junction box. This is somewhat analogous to the manufacture of c-Si PVs, which typically assumes that the cell is a material input to the module. In the case of the c-Si production, the size of the cell and modules are bound by small aspect ratios due to considerations in manufacturing and installation. In a roll-to-roll manufacturing technique the width of a roll would be about 1.5 meters, whereas the length can be considered infinite. Thus, the costs from this analysis are for a perovskite

coated film which can be compared to the costs to produce a c-Si solar cell. The comparison is not quite one-to-one as tabbing of PSCs is accomplished during roll-to-roll and costs ~\$0.01 per watt for the production of a c-Si module.²⁴⁶

Each one GW production requires approximately 6 million m² of solar cell area and would require a modest web speed of 9.7 m/min, which is well within the limits of roll-to-roll technologies. The IPL and other processing equipment is also capable of managing these throughputs. The overall cost of production follows the standard asymptotic relationship in which the COGS is dominated by the material costs at higher production capacity (Figure 24). The curves bound the COGS of the PSCs assuming conservative and modest learning rates for the materials and will be discussed in more detail in the following paragraphs. The small bumps in the curve are caused by the addition of the extra equipment and labor at each 1 GW production increment. From this analysis, the graph of COGS starts to flatten out at around 3 and 4 GW. This demonstrates that the scales at which roll-to-roll becomes competitive with prevailing technologies far exceeds the capacities (\$0.30/W, at ~100MW) considered to date.²⁴⁷ This has some major implications towards the capital and operation expenses that will be discussed in Equipment Costs and Utilities sections below.

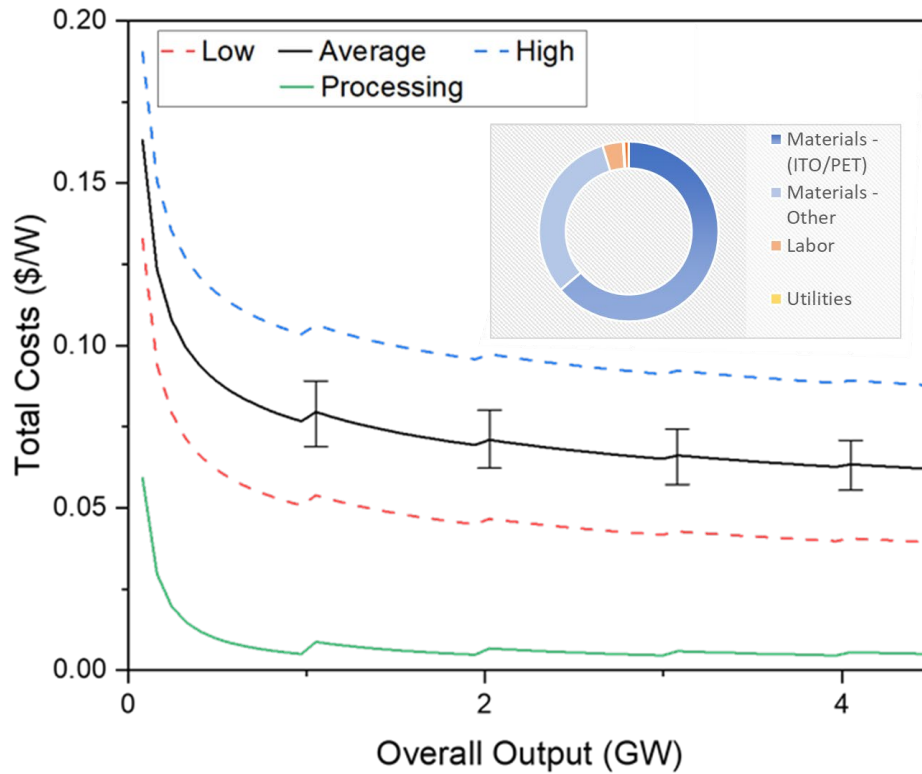


Figure 24: Manufacturing costs of PSCs based on annual output. The curves bound the upper and lower cost estimates using a modest and conservative learning rates applied to the ITO coated PET. The bars on the average curve includes 95% confidence intervals from the Monte-Carlo analysis. The lowest curve shows the costs associated with processing (equipment, labor, utilities, & depreciation). (inset) Contribution to overall costs at 2 GW production using the average learning rate applied to the ITO coated PET.

4.5 Conclusion

The primary advantage of the IPL technique for perovskite thin films lies in its capacity to deliver rapid, non-contact, and cost-effective annealing. As explored in this chapter, the compatibility of IPL with roll-to-roll processing significantly amplifies the benefits for large-scale perovskite technologies. The IPL technique's capability to anneal perovskite thin films makes it an ideal candidate for roll-to-roll integration, offering numerous advantages.

Firstly, IPL annealing does not impact the structural or electrical properties of the underlying ITO/PET substrates. Reduced temperatures and strain within the substrate,

coupled with a shorter film path, are expected to minimize downtime caused by fluctuations in process parameters. Additionally, IPL operates with lower energy consumption, effectively eliminating the thermal losses associated with traditional ovens. This enables reduced dwell times for perovskite annealing, from minutes down to microseconds. Furthermore, IPL has been shown to anneal metal oxide films on plastic substrates, a feat not yet achieved using conventional ovens.

The adoption of IPL technology has a direct and positive influence on the cost of goods sold, both in terms of capital expenditure (CAPEX) and operating expenditure (OPEX). The initial investment for implementing IPL is nearly 30% less than that of a traditional oven, with additional cost savings expected as the scale of operations increases. The associated operating expenses are projected to be around 80% lower for IPL, while simultaneously improving yields through shorter web lengths. These cost savings make the utilization of IPL an attractive option, reducing the overall cost of goods sold and energy payback times, further enhancing the competitive advantage for roll-to-roll fabricated perovskite solar cells.

CHAPTER 5 – FABRICATION OF FLEXIBLE PEROVSKITE SOLAR CELLS VIA RAPID THERMAL ANNEALING

5.1. Introduction

Transitioning from rigid glass to flexible plastic substrates, e.g. PET, for roll-to-roll manufacturing becomes a challenge due to temperature requirements in perovskite annealing stages achieving or even exceeding thermal limitations of the plastic substrates. Techniques have been developed to reduce the necessary annealing temperature for perovskite films, including the modification of precursor chemistry, application of post-deposition treatments, utilization of tailored annealing methods, or a combination of these approaches.^{176, 248-250} Currently, most laboratory-scale depositions use conductive annealing methods, which test the mechanical limitations of substrate materials in high-throughput scenarios. Therefore, alternative methods are required to realize high-throughput production of PSCs. The combination of RTA with a rapid drying step has the potential to greatly reduce the processing time by several orders of magnitude, to mere seconds. The reduction of processing time would lead to a decrease in the length of the web, thereby reducing capital and operational costs and ultimately lowering the overall cost of the module.

5.2 Process Schematic

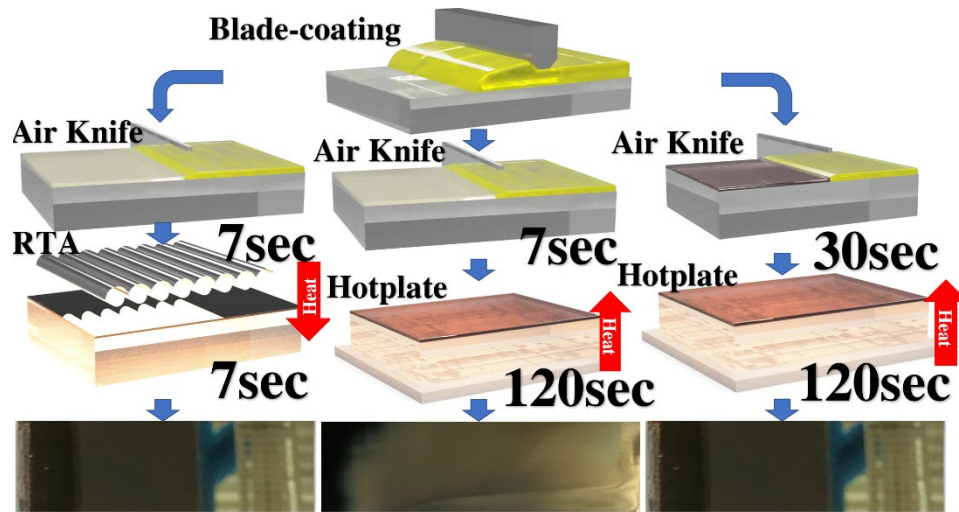


Figure 25: Schematic illustrating procedures to synthesize perovskite thin films using both conductive annealing and RTA. Images of perovskite thin film post-conductive annealing and post-RTA annealing are included.

A stepwise schematic of the perovskite film formation is shown in figure 25 for both conductively annealed and RTA perovskite films. Conventional perovskite fabrication methods utilize physical solvent removal to achieve supersaturation then apply heat to achieve crystal growth. Typically, the air knife step is assumed to achieve the supersaturation prior to the annealing; however, it would be advantageous to reduce the evaporation time without using heated air.

5.3 Characterization of Rapid Thermal Annealed Perovskite Films

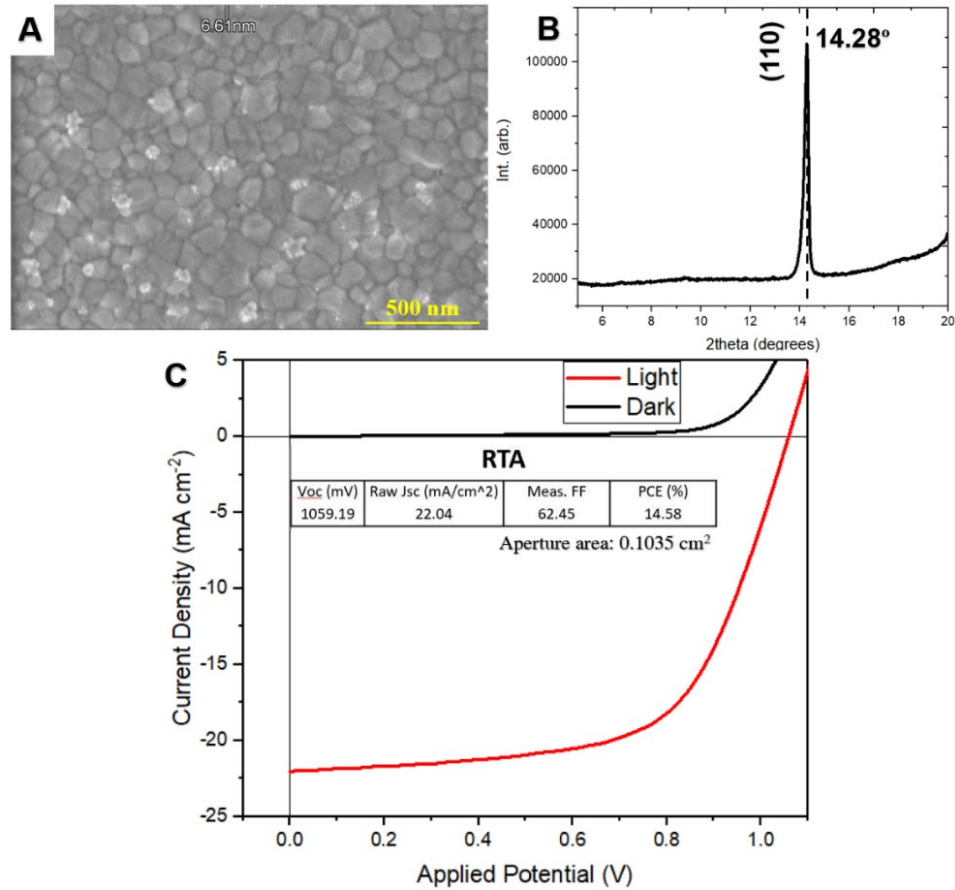


Figure 26: (A) SEM image (B) XRD pattern of perovskite film and (C) JV curve of champion device annealed with RTA.

Currently, air knives used post-deposition are time consuming. The level of supersaturation in the film can be tracked by a color change from yellow to deep brown.¹²⁵ To achieve this level of supersaturation requires multiple air knife passes totaling 25 to 40 seconds depending upon deposition area. To reduce the overall processing time, the films were treated with a single 7 second air knife pass then, prior to supersaturation, heated the films using both a conductive and RTA technique. Perovskite films annealed conductively appeared hazy and did not produce photoactive cells (figure 25). Perovskite films annealed via RTA had a mirror finish (figure 25), were highly crystalline and uniform, (figure 26A&B) and were photoactive (figure 26C). It is likely

that the ramp of temperature in the RTA completes the supersaturation, but further investigation is required to verify this.

Additionally, annealing of perovskite films via RTA took 7 seconds compared to 120 seconds for conductive annealing. This order of magnitude improvement in annealing time is extremely significant for high-throughput manufacturing of PSCs. For context, 120 seconds corresponds to 60 m for a R2R line operating at 30 m min^{-1} . The CAPEX and manufacturing costs for equipment at this scale become a primary motivator not to pursue the technology emphasizing the need for more efficient annealing methods like RTA.

For comparison, devices were made using multiple passes of the air knife (30 seconds) to achieve the supersaturation of the film and then conductively annealed. These devices yielded a PCE of $\sim 14.60\%$ indicating that performance is not sacrificed for processing speed.

5.4 Utility of radiative annealing methods for low heat-tolerant flexible substrates

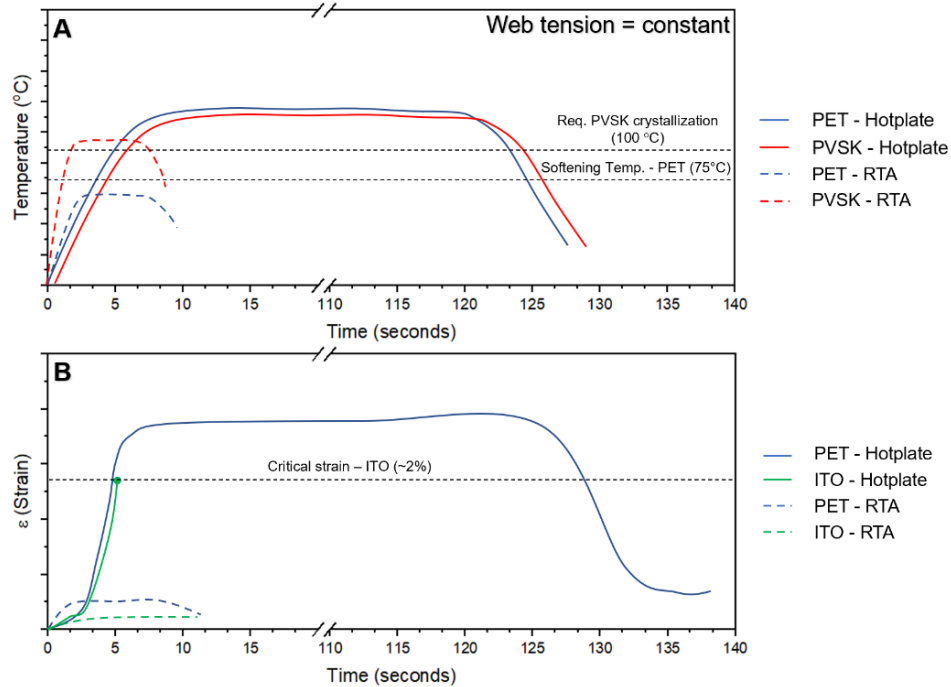


Figure 27: (A) Temperature profile tracking temperature of both PET and PVS on a R2R line annealed by either conduction or RTA. (B) Strain vs time tracking the strain in both PET and ITO on a R2R line annealed by either conduction or RTA. Critical tensile strain for RTA is ~2%.

The amount of heat transferred to the substrate is a concern for flexible solar cells, especially with the mismatch in modulus of a thin ITO layer. Often, temperatures required to anneal PSC layers exceed softening temperatures of flexible plastic (67°C for PET), whereas, perovskite crystallinity increases across annealing temperatures ranging from 100°C to 250°C.²⁵¹ During conductive annealing, heat is transferred to the perovskite film through the plastic substrate. As a result, the temperature of the perovskite thin film and plastic substrate are coupled as sketched in figure 27A. As mentioned, webs on R2R lines are kept under tension. The combination of thermal and mechanical stressors on the web may exceed the critical tensile strain for ITO during

conventional conductive annealing leading to ITO failure (figure 27B).²⁴² RTA circumvents this issue by heating the perovskite film directly via incident radiation on the surface. Additionally, the absorptivity of perovskite is high across much of the IR spectrum reducing the amount of radiation transmitted to the underlying substrate.²⁵² This decouples the temperature of perovskite and substrate reducing the thermal limitations of the system (Figure 27A). As a result, the annealing time and amount of strain in the substrate are severely reduced (Figure 27B).

5.5 Conclusion

Rapid Thermal Annealing (RTA) offers numerous advantageous properties for high-throughput manufacturing of perovskite photovoltaics. Notably, the requirement for supersaturation is relaxed in RTA compared to conductive annealing, increasing process robustness. This approach significantly reduces post-deposition processing time, from 150 seconds down to just 14 seconds. By focusing heat transfer directly onto the perovskite film, RTA minimizes excessive heating of temperature-sensitive substrates, a crucial aspect for plastic substrates under tension. Importantly, a device efficiency of 14.58% is sustained even at these shorter time scales. With successful integration into roll-to-roll production lines, RTA holds immense potential for the high-throughput manufacturing of flexible perovskite photovoltaics.

CHAPTER 6 – IPL-ANNEALING MIXED-CATION PEROVSKITE WITH ROBUST COATING WINDOW

6.1 Introduction

Roll-to-roll manufacturing is a robust technique with great potential to process high-throughput PSCs, addressing many problems of scale.²⁵³ However, the production capacity of a roll-to-roll line is limited by the slowest step. Encouraging results have been demonstrated for high-throughput processing of NiO²⁵⁴, SnO₂²⁵⁵, Cu²⁴⁰, and perovskite^{100, 256} layers by intense pulsed light (IPL) annealing, with opportunities for further refinement. The success for roll-to-roll manufactured perovskites lies in the art of understanding how the coating window changes within a wide range operating parameters including ink formulation, additives, deposition methods, and annealing techniques.^{257, 258}

As mentioned earlier, the LaMer model of nucleation and growth is used to predict and describe perovskite film formation, which is solubility driven.²⁵⁹ Common perovskite precursors form adducts in solution, according to the Lewis theory for acid-base reactions, causing precursor solubility to correlate strongly with Gutmann's donor number.²⁶⁰ Utilizing a combination of Gutmann's donor number and vapor pressure, evaporation kinetics and growth mechanisms can be controlled. Segmenting solvents into VNCS and NVCS to allow users to mix solvents in formulations that amplify their respective merits (quick evaporation, high crystallinity/large grain size). In general, consistent perovskite film formation happens when the three stages of solvent evaporation, transitional phase formation, and annealing occur as independently as possible. The modular nature of

perovskite deposition allows for application of multiple different techniques to enhance the film post-deposition; however, changes to solvent chemistry and/or compositional engineering must have synergy from deposition to annealing all while remaining cost competitive.

Utilizing conventional methods, the combination of thermal and mechanical stressors in PSC manufacturing can severely compromise functionality within the substrate during operation. Several roll-to-roll compatible annealing techniques, including hot air blowing²⁶¹, flash infrared²⁶², rapid thermal²¹⁷, and microwave annealing²⁶³, have been investigated for fabrication of PSCs with promising results. However, electromagnetic absorption by flexible plastic substrates, from these radiative sources, can result in the same substrate instabilities observed in conventional annealing methods. Intense pulsed light (IPL) annealing has drawn widespread attention for its ability to rapidly anneal light absorbing materials (~1ms) without affecting transparent substrates.^{101, 220} Successful integration of IPL annealing in high-throughput roll-to-roll manufacturing lines can reduce oven energy requirements by 80% and reduce the annealing footprint by two orders of magnitude over conventional methods.²⁶⁴ While optimized IPL annealing promotes thin-film densification and grain growth, PSCs manufactured with this method lag behind the state-of-the-art PCEs by ~7-8%. Understanding the interactions between IPL annealing and properties of the perovskite film will help devices approach the state-of-the-art at much higher manufacturing throughputs.

Stability/durability is presently the largest technical risk for perovskite PV with much research devoted to understanding and mitigating chemical reactions of perovskite with the environment by incorporation of additives and variation of precursor species.^{21, 265}

Tunable mixed cation perovskites overcome many issues with phase instability and show promise for high performance and stable devices.⁸¹ Lab-scale mixed cation PSCs have achieved impressive efficiencies; however, research to increase the efficiency at scale (large-area) is crucial to advance the technological readiness of perovskite modules.²⁶⁶

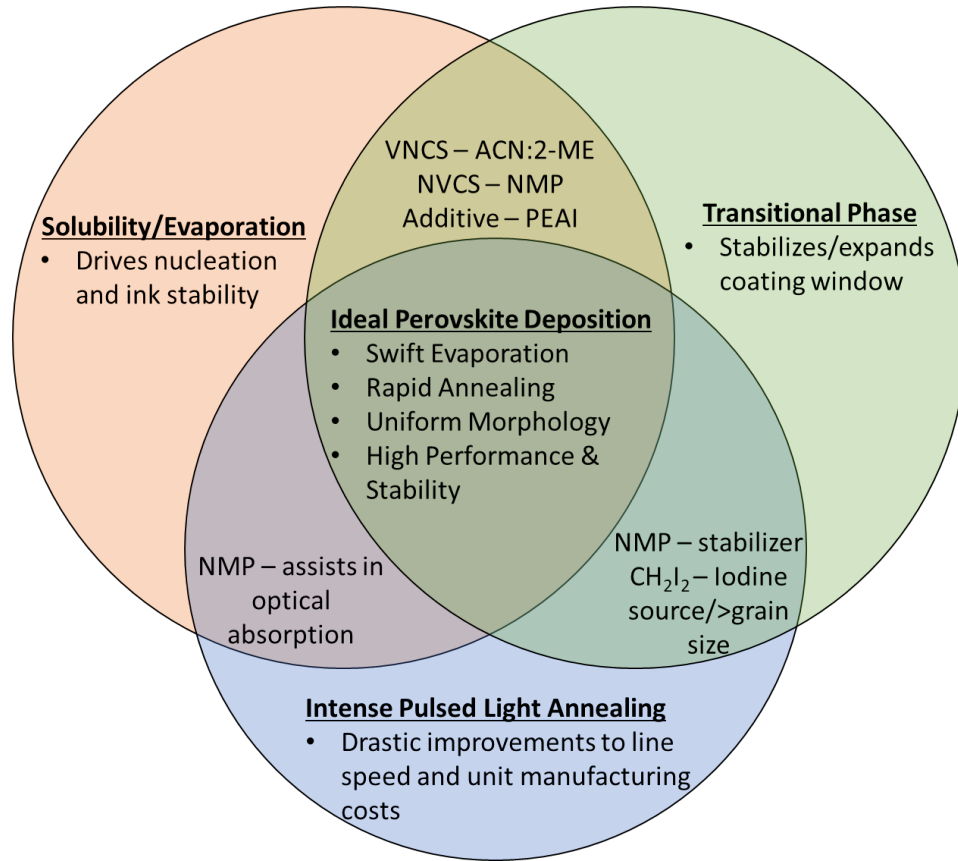


Figure 28: Venn diagram to visualize the approach to designing high-throughput, functional perovskite solar films. Categories of solubility/evaporation of the ink, transitional phase formation, and IPL annealing all are interconnected in the manufacturing process to realize the solar technology.

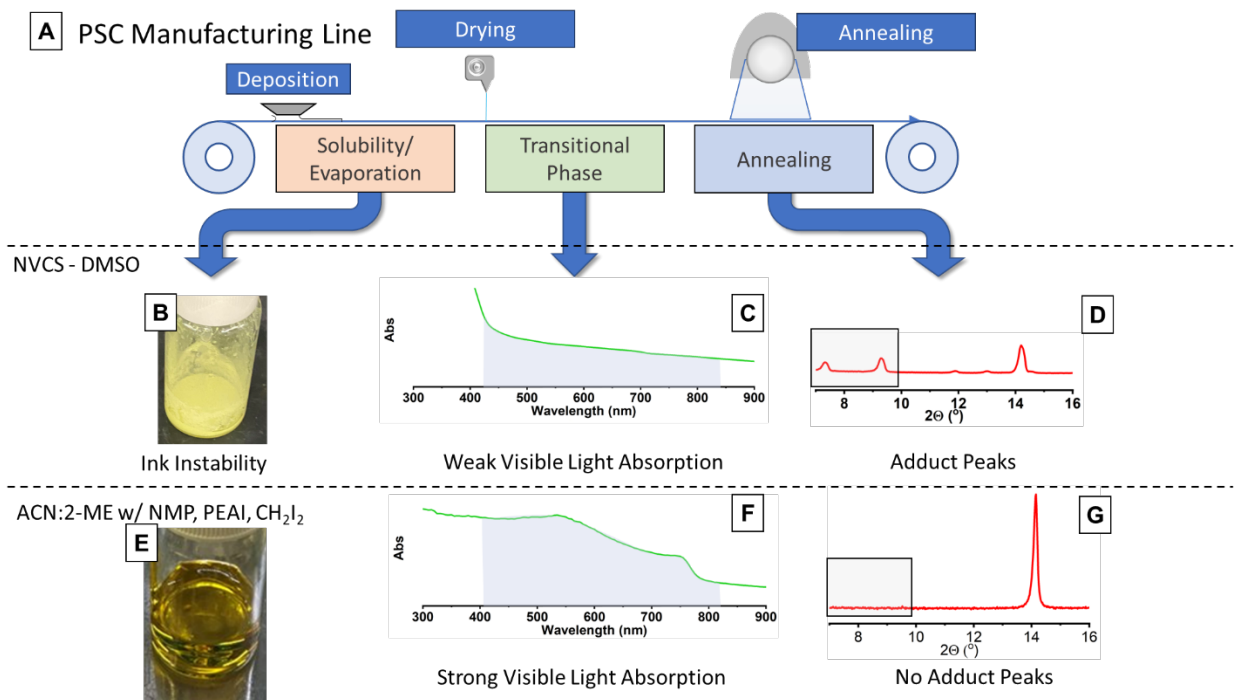
In this work, we discuss a classical roll-to-roll manufacturing perspective for scalable PSC manufacturing that can be applied as a framework to study and develop commercially competitive perovskite solar technologies at scale. We find perovskite thin-film coating fits in a three-parameter processing space where parameters can be evaluated

based upon their merits for solubility/evaporation, transitional phase formation, and IPL annealing (figure 28). The term ‘transitional phase formation’ is a process term referring to a pseudo-stable stage occurring between drying and annealing in a perovskite roll-to-roll manufacturing line that, through a variety of methods to regulate this step, correlate strongly with process robustness. The distinction from the community’s general “intermediate” definition is made to expand the discussion beyond just adduct stabilization of the processing window to consider implications on the processing window for stoichiometric ratios of cationic and anionic species, solubility vs. vapor pressure, optical absorption profiles relevant for photonic annealing methods, and also the adduct stabilized intermediate.

Figure 28, is a useful Venn Diagram that highlights the complex tunability of this process as, for example, compositional variations of the precursor must consider the impact on downstream process stages such as the deposition method, drying parameters and annealing parameters. The solvents and additives listed in the intersecting regions of figure 28, above affect all segments of the diagram but are grouped according to their primary functions in the process. This emphasizes the need for a synergistic approach across all parameters, as exemplified by the multiple roles of NMP in the system. Through this approach, we demonstrate a mixed-cation perovskite ink with a robust coating window that is IPL compatible and on par with our hotplate-annealed standards, having overall PCE’s around 16% on flexible plastic substrates. Our work highlights unique complexities for scale-up of different perovskite compositions and how levers of compositional engineering and post-deposition treatments can be used to overcome manufacturing limitations.

6.2 Process Schematic

A process schematic is illustrated in figure 29, below to help visualize perovskite thin-film formation. This chapter is divided into three sections where process parameters are discussed based upon their impacts to (1) Solubility/Evaporation, (2) Transitional Phase Formation, and (3) IPL Annealing. We discuss our approach to study compositional engineering through the lens of developing scalable manufacturing techniques with the end goal of commercially competitive perovskite solar technologies.



6.3 Solubility/Evaporation

Solvent engineering of the perovskite precursor ink has broad implications for both the film-forming process and film quality. The previously discussed LaMer curve is the

classical description for nucleation and crystal growth from solutions and has widely been applied to model perovskite film formation.²⁶⁷ The density of nucleation sites depends upon the degree of solution supersaturation, which is related to both the solute concentration and solubility. Solute concentration increases as the solution dries, but solubility of perovskite precursors correlates most strongly with the donor number of a solvent system.²⁶⁰ Frequently used perovskite solvents, like DMF and DMSO, have high donor numbers, but slow evaporation kinetics due to low vapor pressure. In our experience, air knife solvent removal methods alone proved insufficient with these solvents as dendritic-like structures formed rendering the film unusable.

Deng et. al. demonstrated that a high vapor pressure, mixed solvent system of 0.6 ACN:0.4 2-ME fabricated high quality MAPbI₃ perovskite films at fast speeds.²⁶⁸ Solubility of mixed cation perovskite components were tested by dissolving precursors in solvents, listed in table 9, then monitoring particulate formation over time. Inks that did not exhibit particulate formation within a week were deemed soluble. Inks that exhibited particulate formation within a week were deemed slightly soluble. Precursors that did not dissolve or formed particulates within 1-2 hours were deemed insoluble. The results are summarized in table 12 with images of stable/non-stable inks in figure 29. MAPbI₃ perovskites dissolve easily into the ACN:2-ME mixture while other cationic and anionic species had more difficulty. Additionally, the perovskite wet film transitioned to the transitional stage within 1-2 seconds using air knife solvent removal methods, well within the acceptable coating window necessary for synergy between solubility/evaporation and transitional phase formation illustrated in figure 29. Incorporation of Br into a mixed perovskite system stabilizes the perovskite and regulates perovskite crystallization but is

highly insoluble in this solvent system. Under operation, FAPbI₃, MAPbBr₃, and MAPbI₃ films were observed with very rough surface morphology and non-uniform surface coverage that suggest there is large particle agglomeration in the pseudo-stable ink that rapidly nucleate during drying. Given the demonstrated success of these other additives for perovskite crystallization and stability, other methods to stabilize the solutes in solution are needed.

Table 12: Results from solubility tests for multiple different perovskite formulations in different solvent systems

	MAPbI₃	FAPbI₃	MAPbBr₃
ACN:2-ME	Soluble	Slight	Insoluble
DMF	Soluble	Soluble	Soluble
DMSO	Soluble	Slight	Soluble
NMP	Soluble	Soluble	Soluble

The approach of utilizing VNCS for fast deposition and NVCS for large grains with high crystallinity is applied to mixed cation systems utilizing high donor number, low vapor pressure solvents of DMSO and NMP. DMSO only slightly improved the solubility of FAPbI₃ and MAPbBr₃ perovskites, whereas NMP dissolved the precursors very quickly. The merits of both fast evaporation and highly crystalline perovskite films are shown in figure 29 as a adduct-stabilized perovskite without PbI₂, confirmed via XRD patterns, is formed using only air knife solvent removal methods. The application of NMP as a NVCS highlights the interconnection between solubility/evaporation and transitional phase formation illustrated in figure 28.

Adding cations that form 2D perovskites have been shown to increase the solubility of perovskite precursors.²⁶⁹ Incorporation of the 2D cation PEAI improved the ink stability and resistance to atmospheric contaminants, such as water and oxygen, that form insoluble complexes with perovskite precursors. Extended shelf life of the precursor ink was observed when using the PEAI additive. Thus, a formulation utilizing the solvent system ACN:2-ME with NMP and PEAI for ink stability was adopted. In the next section, the utility of the NMP to assist with the crystallization will also be described, hence the interrelationship of formulation and processing illustrated in figure 28.

6.4 Transitional phase formation

Perovskite thin-film fabrication has been plagued by inconsistency due to very narrow coating windows highlighted by the extremely time-sensitive anti-solvent dripping approach for solvent removal in spin coating methods.²⁷⁰ The best method to expand this acceptable coating window is to incorporate additives and solvents that help stabilize the perovskite film prior to IPL annealing.²⁷¹

In the current study, two non-volatile coordinating solvents, DMSO and NMP, were considered as stabilizers prior to IPL annealing. IPL annealing is a method to decouple the film temperature and substrate temperature, however, the absorption profile of the DMSO:perovskite adduct indicates that much of the radiant energy is transmitted rather than absorbed, shown in figure 29c. Ghahremani et al managed to overcome this limitation using sequential step IPL annealing, however, it complicates the process, making DMSO not ideally compatible for IPL annealing.¹⁰⁰ Both DMSO and NMP coordinate strongly with perovskite precursors and form an adduct with demonstrated, beneficial qualities towards perovskite film formation. However, DMSO results in lower ink stability, as

described in the solubility/evaporation section, and issues for the transitional phase stabilization, shown in optical images in figure 29b. The strong coordinating affinity of DMSO to perovskite precursors readily dissolves these materials, however, it can be difficult to remove the solvent from the film without heating to temperatures above the glass transition temperature of the substrate.²⁷² The presence of DMSO adducts in the IPL-annealed perovskite film is observed in XRD patterns at ~ 7.4 and 9.4 , shown in figure 29d.

NMP has a lower vapor pressure than DMSO, but has been shown to improve the perovskite film formation.¹⁶¹ Additionally, the NMP:MAPbI₃ adduct absorbs strongly throughout the visible light spectrum, shown in figure 29f making it promising for IPL compatibility. This highlights the synergistic qualities NMP possesses for transitional phase stabilization, and optical absorption, illustrated in figure 29e. The resulting perovskite films, post-drying, possessed a smooth, mirror-like finish suggesting that there is low surface roughness and uniform surface coverage. Based on the promising results this ACN:2-ME + NMP ink was studied for solar cell performance using a hot-plate annealing process for optimization. The results from the NMP optimization experiment are summarized in figure 30 with PCE peaking at 16.5% with 6 mol% NMP. Additionally, the coating window for NMP-stabilized perovskite transitional phase allows for high-quality film formation across a range of times between transitional phase formation and annealing. After achieving the transitional stage, annealing can start after 1 second or 5-10 minutes with little impact on performance. The combination of IPL compatibility and larger coating window results in a more robust perovskite manufacturing process with improvements to process speed and manufacturing yields.

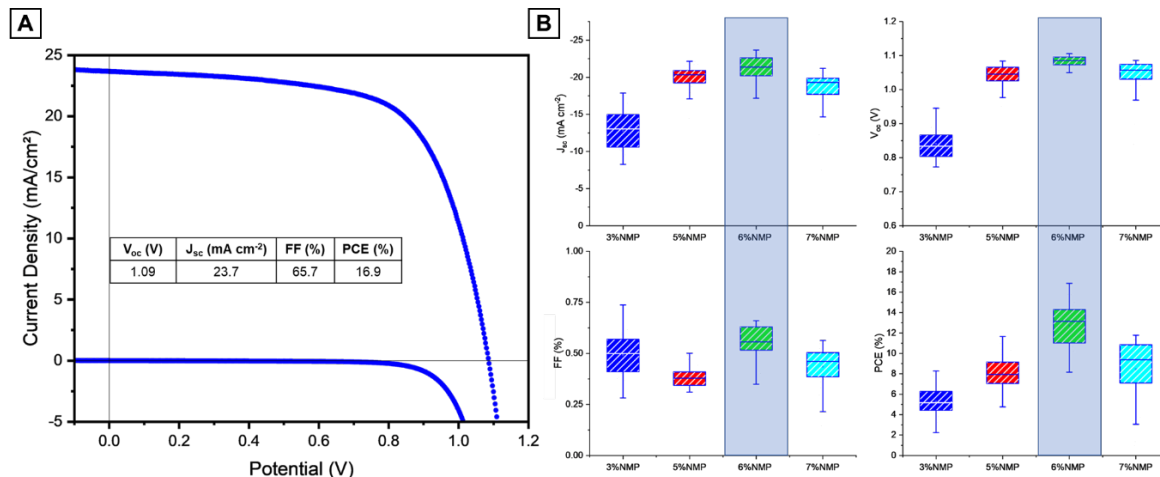


Figure 30: (a) JV performance data of the champion 6% NMP hotplate-annealed sample, light and dark currents. (b) Device performance statistics of short circuit current density (J_{sc}), open circuit voltage (V_{oc}), fill factor (FF), and power conversion efficiency (PCE) at different NMP concentrations in ACN:2-ME. Highest efficiencies achieved when NMP concentration reaches 6%. Each condition tested >15 devices.

6.5 IPL Annealing

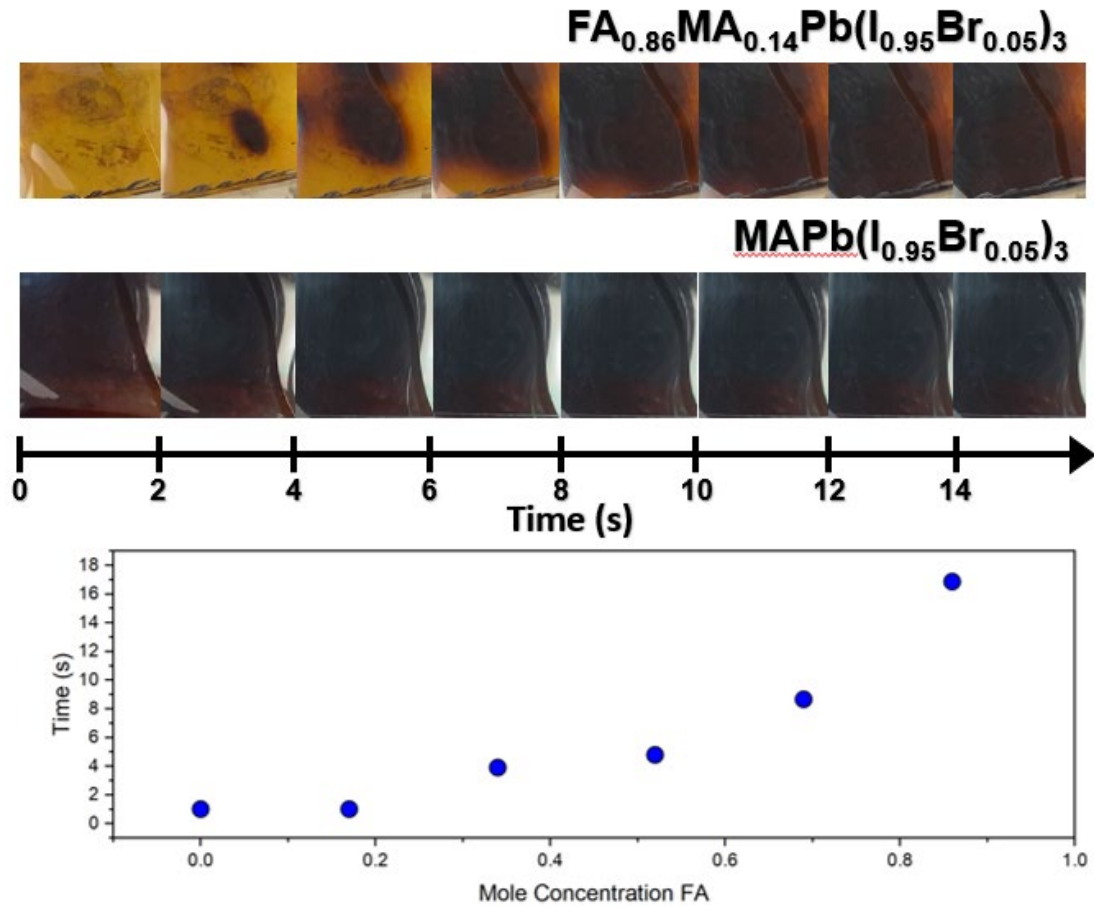


Figure 31: Images of $\text{FA}_{0.86}\text{MA}_{0.14}\text{Pb}(\text{I}_{0.95}\text{Br}_{0.05})_3$ and $\text{MAPb}(\text{I}_{0.95}\text{Br}_{0.05})_3$ at different times during hotplate annealing. A plot of color conversion time vs ratio of FA to MA.

Up until this point, a hotplate annealing technique has been used as a control to investigate impacts of film drying and transitional phase stabilization on device performance. Hotplate annealing is a much slower process, allowing for qualitative interpretation of the film formation. A color change is observed from yellow to brown/black when the perovskite film is converted to the photoactive phase, in most cases. Figure 31 shows that the time required to achieve conversion is highly dependent upon the ratio of $\text{FA}^+:\text{MA}^+$ cations. Density functional theory (DFT) calculations and experimental evidence suggest that the rate of formation of FAPbI_3 is slower than the rate of formation

of MAPbI₃ and are supported by observations in this work.²⁷³ As much of the crystallization kinetics are governed by an Arrhenius-like relation, changes in reaction rates on a hotplate are observed in reaction rates for IPL. Therefore, IPL annealing conditions must be tailored to the FA⁺:MA⁺ ratio, accordingly.

A major advantage of IPL for scalable manufacturing is the rapid, time-saving nature of the annealing process; however, this can be counterproductive to the optoelectronic properties of the perovskite layer as slower crystal growth and long annealing times (~minutes) yield more crystalline films and higher efficiency perovskite. As such, there is a large discrepancy in J_{sc}, V_{oc}, FF and PCE between hotplate-annealed perovskite devices and IPL-annealed perovskite devices (shown in Figure 32). Unfortunately, solvent systems with acceptable coating windows for hotplate annealing cannot simply be reoptimized using the IPL parameter space. To be IPL compatible, the film must be visible light absorbing, have a tolerable solvent concentration at the moment of irradiation (prevent rapid volatilization of solvent), and possess the desired PV properties post-IPL annealing. A combination of compositional engineering and tailoring IPL parameters are required to maintain functionality at the higher speeds.

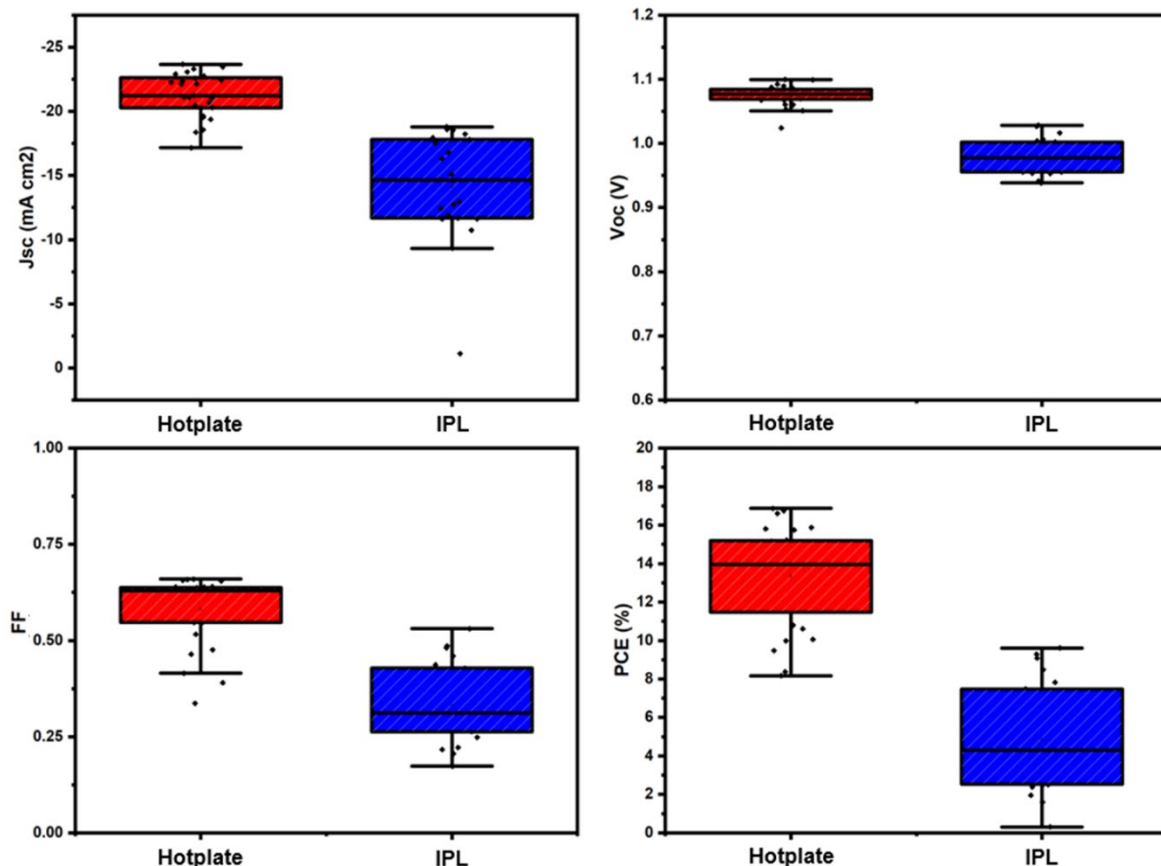


Figure 32: Comparison of performance metrics for Hotplate- and IPL-annealed PSCs. Pixel size is 0.125 cm².

The IPL parameter space is dependent upon voltage across the lamp, pulse duration, number of pulses, and delay between pulses. With four parameter nodes and numerous conditions (voltage: 1500-2500 V, pulse duration: 100-2000 μ sec, pulse delay: >100 msec, number of pulses: 3-5), it is imperative to identify relevant parameters to constrain the parameter space before using time consuming analytical techniques. Qualitative feedback on IPL optimization was rapidly gathered through visual inspection of the film surface post-IPL annealing as there is a drastic color change from the reddish-brown (figure 33a) to a dark black/brown (figure 33b) in the film. When the film is too thin and/or the IPL annealing is insufficient, the final film will still resemble the transitional phase (figure 33a).

When the film is too thick and/or the IPL annealing is excessive, the final film shows cracking or appears ablated (figure 33c&d). Approximately optimized IPL conditions will not show these signs and maintain a mirror finish with uniform surface coverage (Figure 33b). Probing this space, optimal IPL annealing parameters were within these ranges: 1700-1900 V, 300-500 μ sec pulse duration, 500 msec pulses delay, and 3 pulses.

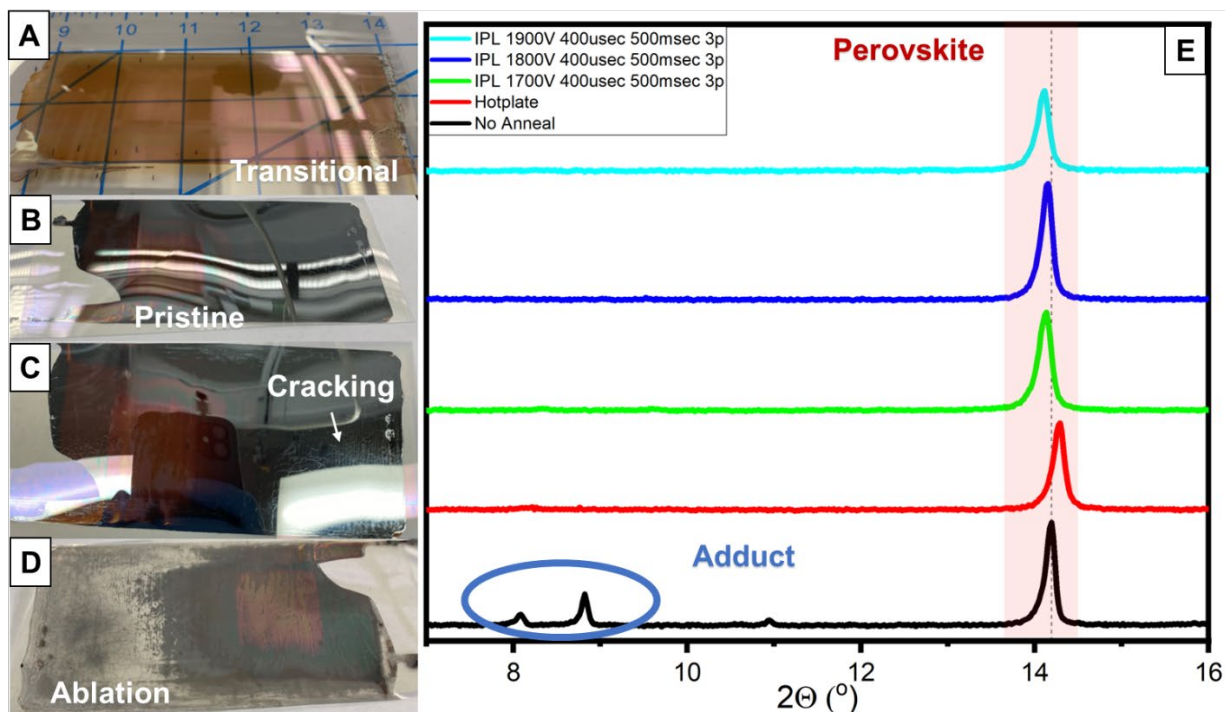


Figure 33: (a-d) Optical images highlight qualitative approach to observe pros/cons of IPL-annealed perovskite solar films. (e) XRD patterns of neat, hotplate-annealed, and three different IPL conditions at increasing voltages. This highlights the flexibility of IPL parameter space to be tailored for a given application.

Upon approaching optimized IPL parameters, further refinement results in marginal changes, indistinguishable via optical evaluation, necessitating the implementation of alternative analytical techniques for more precise characterization. Therefore, XRD patterns of IPL-annealed perovskites were compared against the transitional film (no anneal) and hotplate-annealed samples (figure 33e). If the NMP-perovskite adduct is still present post-annealing, then low-angle peaks ($<10^\circ$) are observed (figure 33e, black).

When the adduct peaks are not observed post-IPL annealing, it confirms the NMP-stabilized perovskite has been converted to the crystalline perovskite phase via IPL annealing (figure 29g; figure 33e, not black). Additionally, the IPL process did not result in detectable formation of PbI_2 , a common indicator of degradation. The three different IPL annealing conditions shown in figure 33e are similar suggesting that perovskite conversion is acceptable across a range of IPL conditions. With this range of acceptable values, lower constraint of 1700 V, 400 μsec pulse duration, 500 msec pulse delay, and 3 pulses was selected as the IPL annealing condition for energy conservation.

In previous works, we have shown that, diiodomethane (CH_2I_2), interacts with IPL to fill iodine vacancies within the perovskite, reduce surface tension of the precursor chemistry, and improve overall device performance of PSCs.^{101, 102} This work exemplifies an additives ability to effect solubility/evaporation, transitional phase formation, and IPL annealing. Incorporating this additive into our chemistry did not affect the solution solubility or color of the transitional film to an observable level, highlighting the interconnection between solubility/evaporation and downstream IPL annealing, illustrated in figure 34. SEM images indicate that the CH_2I_2 additive drastically increased the perovskite domain size by $\sim 2\text{X}$, shown in figure 34a-b. Additionally, XRD patterns of the resulting film show no signs of degradation and/or residual adduct present after IPL annealing (figure 34c). Xu et. al. also demonstrated that the addition of the CH_2I_2 promoted the vertical grain growth and there were no visible voids established using an energy density higher than what was employed in this work.¹⁰²

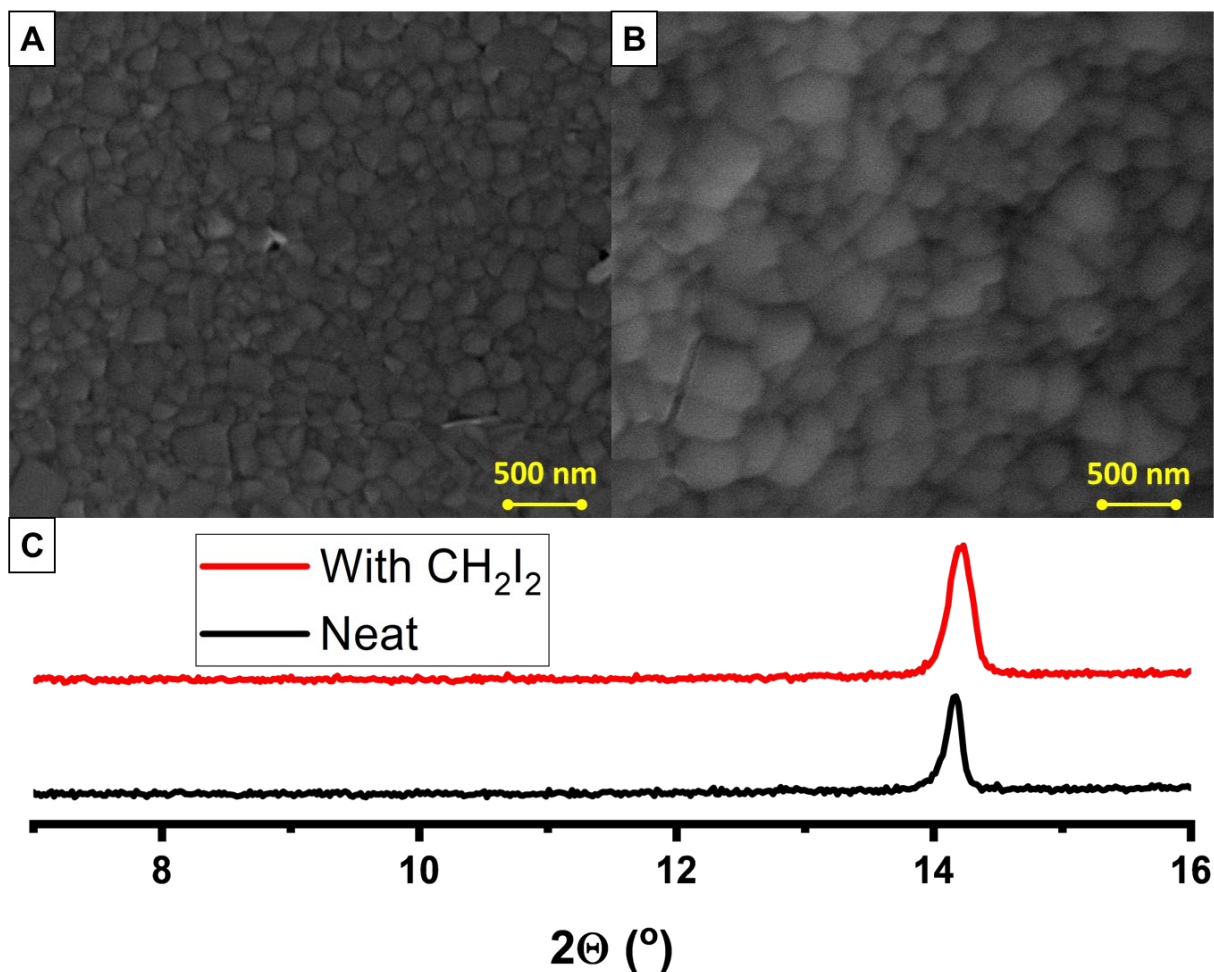


Figure 34: (a) SEM image of the neat perovskite film after IPL annealing. (b) SEM image of the perovskite film with CH_2I_2 additive after IPL annealing. (c) XRD pattern of the resulting perovskite film after IPL annealing with the CH_2I_2 additive and without the CH_2I_2 additive (Neat).

Following the encouraging results from both IPL annealing conditions and CH_2I_2 additive, the merits of both optimized IPL annealing conditions and the CH_2I_2 additive were measured by their impact to the overall PCE vs hotplate-annealed samples. The statistical data is shown in figure 35 and were obtained from 14 and 20 devices, respectively. Hotplate-annealed PSCs had slightly higher V_{oc} and J_{sc} but observed lower fill factors than IPL-annealed PSCs. Champion device of 16.68% PCE for IPL-annealed

samples are shown in figure 35a. IPL-annealed PSCs had a tighter distribution across the sample set, suggesting that the technique is more reproducible.

In another experiment, the transitional perovskite film was coated directly with the SnO₂ and the two film stacks were then annealed using the IPL process conditions of 1700 V, 400 msec pulse duration, 500 msec pulse delay, 3 pulses. The resulting devices had a significantly lower J_{sc} (~25% less) and a slightly lower FF (~12% less). The reduction in performance is likely due to annealing occurring outside of the time-sensitive processing window and sensitivity of the transitional perovskite state to solvents. The use of a single annealing process of a multiple stack would be an advantage, but more work is required to optimize.

To identify whether the hotplate annealing of SnO₂ was affecting the perovskite layer, PSCs in which the SnO₂ was processed using IPL were fabricated. The IPL parameters were identical for perovskite and SnO₂ layers and no optimization of IPL parameters for the SnO₂ layer was done. The champion device PCE was higher for the IPL-annealed SnO₂ sample; however, hysteresis was observed which would indicate a non-optimized process.

A combination of optimized IPL annealing conditions and the CH₂I₂ additive resulted in IPL-annealed devices that were as/more efficient than hotplate-annealed devices, previously unachievable as shown in figure 32. The drastic increase in processing speed causes a significant reduction in unit manufacturing costs, making this solvent system enticing for high-throughput, low-cost roll-to-roll manufacturing. The technoeconomic analysis by Martin et. al. showed that the capital expenditures for IPL

would be 30% less, for the same throughput, and operating expenses would be 80% less than traditional ovens.²⁶⁴

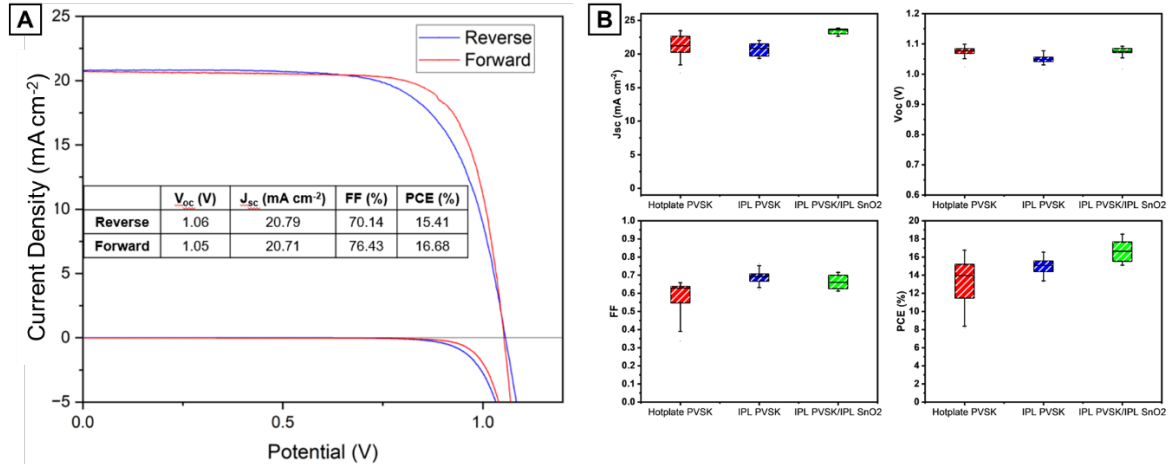


Figure 35: (a) JV performance data of the champion IPL-annealed PSC using the optimized ink formulation, light and dark currents. Optimized ink formulation: $FA_{0.4}MA_{0.6}PbI_{0.95}Br_{0.05}$ in 0.6 ACN:0.4 2-ME (v:v) with 6% NMP (mol%), 3 mg/mL PEAI, 38 $\mu\text{L/mL}$ CH_2I_2 . (b) Comparison of the performance data of PSCs with Hotplate-annealed perovskite layer, IPL-annealed perovskite layer, and IPL-annealed perovskite and SnO_2 layers. IPL-annealed samples match hotplate-annealed samples and are processed in <30 seconds. The IPL parameters used for IPL-annealed samples were 1700V, 500 μsec duration, 500 msec delay, 3 pulses.

6.6 Conclusion

Roll-to-roll manufacturing presents promising solutions to commercialization challenges, however, translating lab-scale perovskite deposition techniques to a continuous platform introduces complexity. Approaches to address these issues individually often results in solutions that fail to fully address the complex and interrelated problems imposed by commercialization. This manuscript details a unique approach, referenced in figure 28, to these challenges utilizing a combination of compositional engineering and post-

deposition treatments to satisfy the constraints rendered by high-throughput roll-to-roll manufacturing.

The transition to mixed-cation perovskite systems create solubility concerns with impacts to perovskite nucleation and crystal growth. A stable ink with quick evaporation was achieved utilizing a mixture of VNCS (ACN:2-ME), NVCS (NMP), and additives (PEAI). The NMP stabilized adduct had a robust coating window and absorbed across optical wavelengths, advantageous for IPL compatibility. Finally, IPL parameters were tailored to the process and incorporation of CH_2I_2 , as an iodine source, resulted in 2x increase in perovskite domain size vs neat when IPL-annealed. The result is perovskite thin-film depositions executed in <30 seconds for a mixed cation system with a champion PCE of 16.7% on flexible plastic substrates, comparable to state-of-the-art, flexible, high-throughput PSCs. While this efficiency is lower than some literature reports, it distinguishes itself by first using ITO-PET growth substrates, second doing four critical layers via blade coating (PTAA, PFN, absorber, SnO_2), and third using IPL to rapidly anneal the absorber. This demonstration of our approach to scalable perovskite thin film coating for IPL annealing has broad applications for development of commercial perovskite solar technologies. Stability remains a barrier to commercialization, and, although mixed cation perovskites exhibit enhanced stability compared to MAPbI_3 perovskites, further analysis is needed. IPL has been used in roll-to-roll manufacturing, however, there are currently no commercial applications of IPL processing of perovskites. The main challenges yet to be addressed for commercialization are demonstration of IPL annealing in a perovskite module and additional durability testing under realistic operating

conditions. To our knowledge, this is one of the fastest fabrication methods for perovskite solar films and has the potential for faster capacity than silicon PV.

CHAPTER 7 – CONCLUSIONS

Despite the significant advancements made in PSC technology, commercialization is still faced with considerable challenges, including stability, module efficiency, and scalability. Commercialization efforts often only partially resolve existing issues and/or create new challenges. This study proposes a comprehensive approach to PSC development based on the evaluation of materials and methods for both parameters of perovskite film formation and technical challenges facing PSC commercialization.

Radiative annealing methods demonstrate the ability to anneal perovskite thin films and are well suited for roll-to-roll integration. A technoeconomic analysis of IPL indicates that the technique directly impacts the cost of goods sold through both the CAPEX and operating expenditures. CAPEX of implementing IPL is nearly 30% less than a traditional oven and with further increases in scale, more costs savings will be realized. Associated operating expenditures are expected to be ~80% less for IPL, while simultaneously improving yields via shorter web lengths. Cost-savings for IPL utilization reduces cost of goods sold and energy payback times further improving the cost advantages for roll-to-roll fabricated PSCs.

IPL annealing of perovskite does not affect the structural or electrical properties of underlying ITO/PET substrates. Lower temperatures, and therefore strain, in the substrate coupled with a shorter film path should reduce downtime attributed to

fluctuations in process parameters. IPL also operates at a lower energy consumption by eliminating the thermal losses from large, traditional ovens. Dwell times to anneal perovskite are significantly reduced from minutes to microseconds. Additionally, IPL can anneal metal oxide films on plastic substrates which has not been demonstrated in conventional ovens.

RTA addresses many issues for high-throughput manufacturing of PSCs. RTA expands the acceptable processing window, compared to conductive annealing, and shortens the post-deposition processing time from 150 seconds to 14 seconds. The focused heat transfer prevents excessive heating of temperature-sensitive substrates, crucial for substrates under tension. Despite the shorter processing time, a device efficiency of 14.58% was maintained. This technology has been successfully implemented in roll-to-roll production lines and holds significant potential for large-scale production of flexible perovskite PVs.

A combination of compositional engineering, scalable deposition methods, and IPL annealing were utilized to address the significant challenges facing PSC of stability, scalability, and manufacturing. The transition to mixed-cation perovskite systems, necessary to improve stability, create solubility concerns with impacts to perovskite nucleation and crystal growth. A stable ink with quick evaporation was achieved utilizing a mixture of VNCS (ACN:2-ME), NVCS (NMP), and additives (PEAI). The NMP stabilized adduct had a robust coating window and absorbed across optical wavelengths, advantageous for IPL compatibility. Finally, IPL parameters were tailored to the process and incorporation of CH_2I_2 , as an iodine source, resulted in 2x increase in perovskite domain size vs neat when IPL-annealed. The result is perovskite thin-film depositions

executed in <30 seconds for a mixed cation system with a champion PCE of 16.7% on flexible plastic substrates, comparable to state-of-the-art, flexible, high-throughput PSCs. While this efficiency is lower than some literature reports, it distinguishes itself by first using ITO-PET growth substrates, second doing four critical layers via blade coating (PTAA, PFN, absorber, SnO₂), and third using IPL to rapidly anneal the absorber. To our knowledge, this is one of the fastest fabrication methods for perovskite solar films and has the potential for faster capacity than silicon PV. This approach to commercialization of scalable perovskite thin film coating for IPL annealing has broad applications for development of commercial perovskite solar technologies.

CHAPTER 8 – RECOMMENDATIONS

The extensive body of literature on PSCs creates a complex landscape, making it difficult to accurately predict relationships between optoelectronic properties and compositional engineering, pre- and post-deposition treatments, doping, ambient conditions, deposition methods, solvents, molar compositions, drying conditions, and annealing parameters. To streamline the commercialization path for PSCs, a perovskite database using large statistical experiments and learning models could provide valuable insights on the relationships related to optoelectronic properties.

For IPL, the amount of radiant energy absorbed by a thin film is a function of the absorption profile of the sample and the emission profile from the light source, which is wavelength dependent. Components within a PSC have demonstrated sensitivity to UV light, present within the broad IPL spectrum, damaging the device's performance. Volatilization of A-site organic cationic species from the perovskite crystal structure is a leading mechanism for instability in the perovskite layer, with increased reaction rates around grain boundaries. A method to improve the quality of a perovskite thin film is to conduct the deposition under a vapor layer saturated in A-site cations. IPL has demonstrated the ability to sinter perovskite films via vaporization and redeposition at grain boundaries. Under the assumption that perovskite solar modules are encapsulated, it is reasonable to assume that the volatilized cationic species released during degradation

will create a pseudo-saturated vapor space around the perovskite film. IPL, with a combination of wavelength filtering and light blocking, could be utilized to irradiate a degraded perovskite solar module, re-sintering the damaged perovskite film, and recover the device performance. A potential remediation tool utilizing IPL for perovskite solar modules would significantly improve commercialization efforts by addressing issues for stability, manufacturing, and bankability.

REFERENCES

- (1) IEA. World Energy Outlook 2022. *IEA* **2022**.
- (2) UNEP. Emissions gap report 2022. *UN environment programme* **2022**.
- (3) SEIA. Solar Industry Research Data. *SEIA* **2022**.
- (4) (FERC), U. F. E. R. C. Energy infrastructure update for August 2022. **2022**, 4.
- (5) Deloitte. 2023 renewable energy industry outlook. **2023**.
- (6) IEA. Renewables. *IEA* **2021**.
- (7) Feldman, D.; Dummit, K.; Zuboy, J.; Margolis, R. *Fall 2022 Solar Industry Update*; National Renewable Energy Lab.(NREL), Golden, CO (United States), 2022.
- (8) NREL. Top 6 Things You Didn't Know About Solar Energy. **2016**.
- (9) Lighthouse, P. Altermatt Lecture: The Solar Spectrum. *PV Lighthouse* **2023**.
- (10) Park, N.-G.; Segawa, H. Research Direction toward Theoretical Efficiency in Perovskite Solar Cells. *ACS Photonics* **2018**, 5 (8), 2970-2977. DOI: 10.1021/acsp Photonics.8b00124.
- (11) Jean, J.; Brown, P. R.; Jaffe, R. L.; Buonassisi, T.; Bulović, V. Pathways for solar photovoltaics. *Energy & Environmental Science* **2015**, 8 (4), 1200-1219, 10.1039/C4EE04073B. DOI: 10.1039/C4EE04073B.
- (12) Eperon, G. E.; Leijtens, T.; Bush, K. A.; Prasanna, R.; Green, T.; Wang, J. T.-W.; McMeekin, D. P.; Volonakis, G.; Milot, R. L.; May, R. J. S. Perovskite-perovskite tandem photovoltaics with optimized band gaps. **2016**, 354 (6314), 861-865.
- (13) Wei, Q.; Yang, D.; Yang, Z.; Ren, X.; Liu, Y.; Feng, J.; Zhu, X.; Liu, S. F. J. R. a. Effective solvent-additive enhanced crystallization and coverage of absorber layers for high efficiency formamidinium perovskite solar cells. **2016**, 6 (62), 56807-56811.
- (14) Lin, Q.; Armin, A.; Nagiri, R. C. R.; Burn, P. L.; Meredith, P. J. N. P. Electro-optics of perovskite solar cells. **2015**, 9 (2), 106-112.
- (15) Dong, Q.; Fang, Y.; Shao, Y.; Mulligan, P.; Qiu, J.; Cao, L.; Huang, J. J. S. Electron-hole diffusion lengths > 175 μm in solution-grown $\text{CH}_3\text{NH}_3\text{PbI}_3$ single crystals. **2015**, 347 (6225), 967-970.
- (16) Shi, D.; Adinolfi, V.; Comin, R.; Yuan, M.; Alarousu, E.; Buin, A.; Chen, Y.; Hoogland, S.; Rothenberger, A.; Katsiev, K. J. S. Low trap-state density and long carrier diffusion in organolead trihalide perovskite single crystals. **2015**, 347 (6221), 519-522.
- (17) Hsu, D. D.; O'Donoghue, P.; Fthenakis, V.; Heath, G. A.; Kim, H. C.; Sawyer, P.; Choi, J.-K.; Turney, D. E. Life Cycle Greenhouse Gas Emissions of Crystalline Silicon Photovoltaic Electricity Generation. *Journal of Industrial Ecology* **2012**, 16 (s1), S122-S135, <https://doi.org/10.1111/j.1530-9290.2011.00439.x>. DOI: <https://doi.org/10.1111/j.1530-9290.2011.00439.x> (accessed 2023/01/19).
- (18) Snath, H. J. Present status and future prospects of perovskite photovoltaics. *Nature materials* **2018**, 17 (5), 372-376. DOI: 10.1038/s41563-018-0071-z.
- (19) Smith, B. L.; Woodhouse, M.; Horowitz, K. A.; Silverman, T. J.; Zuboy, J.; Margolis, R. M. *Photovoltaic (PV) Module Technologies: 2020 Benchmark Costs and Technology Evolution Framework Results*; National Renewable Energy Lab.(NREL), Golden, CO (United States), 2021.

- (20) Schwab, A. *Bioenergy Technologies Office Multi-Year Program Plan. March 2016*; Bioenergy Technologies Office, 2016.
- (21) Dunfield, S. P.; Bliss, L.; Zhang, F.; Luther, J. M.; Zhu, K.; van Hest, M. F.; Reese, M. O.; Berry, J. J. A. E. M. From defects to degradation: A mechanistic understanding of degradation in perovskite solar cell devices and modules. **2020**, *10* (26), 1904054.
- (22) Conings, B.; Drijkoningen, J.; Gauquelin, N.; Babayigit, A.; D'Haen, J.; D'Olieslaeger, L.; Ethirajan, A.; Verbeeck, J.; Manca, J.; Mosconi, E. J. A. E. M. Intrinsic thermal instability of methylammonium lead trihalide perovskite. **2015**, *5* (15), 1500477.
- (23) Pei, F.; Li, N.; Chen, Y.; Niu, X.; Zhang, Y.; Guo, Z.; Huang, Z.; Zai, H.; Liu, G.; Zhang, Y. J. A. E. L. Thermal Management Enables More Efficient and Stable Perovskite Solar Cells. **2021**, *6* (9), 3029-3036.
- (24) Purohit, Z.; Song, W.; Carolus, J.; Chaliyawala, H.; Lammar, S.; Merckx, T.; Aernouts, T.; Tripathi, B.; Daenen, M. J. S. R. Impact of Potential-Induced Degradation on Different Architecture-Based Perovskite Solar Cells. **2021**, *5* (9), 2100349.
- (25) Brecl, K.; Jošt, M.; Bokalič, M.; Ekar, J.; Kovač, J.; Topič, M. J. S. R. Are Perovskite Solar Cell Potential-Induced Degradation Proof? **2022**, *6* (2), 2100815.
- (26) Bowring, A. R.; Bertoluzzi, L.; O'Regan, B. C.; McGehee, M. D. J. A. E. M. Reverse bias behavior of halide perovskite solar cells. **2018**, *8* (8), 1702365.
- (27) Sanehira, E. M.; Tremolet de Villers, B. J.; Schulz, P.; Reese, M. O.; Ferrere, S.; Zhu, K.; Lin, L. Y.; Berry, J. J.; Luther, J. M. J. A. E. L. Influence of electrode interfaces on the stability of perovskite solar cells: reduced degradation using MoO_x/Al for hole collection. **2016**, *1* (1), 38-45.
- (28) Christians, J. A.; Zhang, F.; Bramante, R. C.; Reese, M. O.; Schloemer, T. H.; Sellinger, A.; van Hest, M. F.; Zhu, K.; Berry, J. J.; Luther, J. M. J. A. E. L. Stability at scale: challenges of module interconnects for perovskite photovoltaics. **2018**, *3* (10), 2502-2503.
- (29) Rolston, N.; Bush, K. A.; Printz, A. D.; Gold-Parker, A.; Ding, Y.; Toney, M. F.; McGehee, M. D.; Dauskardt, R. H. J. A. E. M. Engineering stress in perovskite solar cells to improve stability. **2018**, *8* (29), 1802139.
- (30) Dailey, M.; Li, Y.; Printz, A. D. J. A. o. Residual Film Stresses in Perovskite Solar Cells: Origins, Effects, and Mitigation Strategies. **2021**, *6* (45), 30214-30223.
- (31) Li, D.; Zhang, D.; Lim, K.-S.; Hu, Y.; Rong, Y.; Mei, A.; Park, N.-G.; Han, H. A Review on Scaling Up Perovskite Solar Cells. **2021**, *31* (12), 2008621. DOI: <https://doi.org/10.1002/adfm.202008621>.
- (32) Li, Z.; Klein, T. R.; Kim, D. H.; Yang, M.; Berry, J. J.; van Hest, M. F. A. M.; Zhu, K. Scalable fabrication of perovskite solar cells. *Nature Reviews Materials* **2018**, *3* (4), 18017. DOI: 10.1038/natrevmats.2018.17.
- (33) Galagan, Y.; Coenen, E. W.; Verhees, W. J.; Andriessen, R. J. J. o. M. C. A. Towards the scaling up of perovskite solar cells and modules. **2016**, *4* (15), 5700-5705.
- (34) Ono, L. K.; Park, N.-G.; Zhu, K.; Huang, W.; Qi, Y. Perovskite Solar Cells—Towards Commercialization. *ACS Energy Letters* **2017**, *2* (8), 1749-1751. DOI: 10.1021/acsenergylett.7b00517.
- (35) Fassel, P.; Lami, V.; Bausch, A.; Wang, Z.; Klug, M. T.; Snaith, H. J.; Vaynzof, Y. J. E.; science, e. Fractional deviations in precursor stoichiometry dictate the properties, performance and stability of perovskite photovoltaic devices. **2018**, *11* (12), 3380-3391.
- (36) Park, B.-w.; Kedem, N.; Kulbak, M.; Lee, D. Y.; Yang, W. S.; Jeon, N. J.; Seo, J.; Kim, G.; Kim, K. J.; Shin, T. J. J. N. c. Understanding how excess lead iodide precursor improves halide perovskite solar cell performance. **2018**, *9* (1), 3301.

- (37) Dong, Q.; Shang, W.; Yu, X.; Yin, Y.; Jiang, C.; Feng, Y.; Bian, J.; Song, B.; Jin, S.; Zhou, Y. J. A. E. L. Critical role of organoamines in the irreversible degradation of a metal halide perovskite precursor colloid: mechanism and inhibiting strategy. **2021**, *7* (1), 481-489.
- (38) Zhu, J.; Kim, D. H.; Kim, J. D.; Lee, D. G.; Kim, W. B.; Chen, S. W.; Kim, J. Y.; Lee, J. M.; Lee, H.; Han, G. S. J. A. E. L. All-in-one Lewis base for enhanced precursor and device stability in highly efficient perovskite solar cells. **2021**, *6* (10), 3425-3434.
- (39) Im, J.-H.; Lee, C.-R.; Lee, J.-W.; Park, S.-W.; Park, N.-G. 6.5% efficient perovskite quantum-dot-sensitized solar cell. *Nanoscale* **2011**, *3* (10), 4088-4093, 10.1039/C1NR10867K. DOI: 10.1039/C1NR10867K.
- (40) Kojima, A.; Teshima, K.; Shirai, Y.; Miyasaka, T. Organometal Halide Perovskites as Visible-Light Sensitizers for Photovoltaic Cells. *Journal of the American Chemical Society* **2009**, *131* (17), 6050-6051. DOI: 10.1021/ja809598r.
- (41) NREL. Champion Photovoltaic Module Efficiency Chart. *NREL* **2022**.
- (42) Sun, X.; Asadpour, R.; Nie, W.; Mohite, A. D.; Alam, M. A. A Physics-Based Analytical Model for Perovskite Solar Cells. *IEEE Journal of Photovoltaics* **2015**, *5* (5), 1389-1394. DOI: 10.1109/JPHOTOV.2015.2451000.
- (43) Gottesman, R.; Lopez-Varo, P.; Gouda, L.; Jimenez-Tejada, Juan A.; Hu, J.; Tirosh, S.; Zaban, A.; Bisquert, J. Dynamic Phenomena at Perovskite/Electron-Selective Contact Interface as Interpreted from Photovoltage Decays. *Chem* **2016**, *1* (5), 776-789. DOI: 10.1016/j.chempr.2016.10.002 (accessed 2023/01/20).
- (44) Zhang, Q.; Dandeneau, C. S.; Zhou, X.; Cao, G. ZnO Nanostructures for Dye-Sensitized Solar Cells. **2009**, *21* (41), 4087-4108. DOI: <https://doi.org/10.1002/adma.200803827>.
- (45) Wehrenfennig, C.; Eperon, G. E.; Johnston, M. B.; Snaith, H. J.; Herz, L. M. High Charge Carrier Mobilities and Lifetimes in Organolead Trihalide Perovskites. *Advanced materials* **2014**, *26* (10), 1584-1589. DOI: 10.1002/adma.201305172.
- (46) Leijtens, T.; Stranks, S. D.; Eperon, G. E.; Lindblad, R.; Johansson, E. M. J.; McPherson, I. J.; Rensmo, H.; Ball, J. M.; Lee, M. M.; Snaith, H. J. Electronic Properties of Meso-Superstructured and Planar Organometal Halide Perovskite Films: Charge Trapping, Photodoping, and Carrier Mobility. *ACS nano* **2014**, *8* (7), 7147-7155. DOI: 10.1021/nn502115k.
- (47) Yang, J.; Siempelkamp, B. D.; Mosconi, E.; De Angelis, F.; Kelly, T. L. Origin of the Thermal Instability in CH₃NH₃PbI₃ Thin Films Deposited on ZnO. *Chemistry of Materials* **2015**, *27* (12), 4229-4236. DOI: 10.1021/acs.chemmater.5b01598.
- (48) Tiwana, P.; Docampo, P.; Johnston, M. B.; Snaith, H. J.; Herz, L. M. Electron Mobility and Injection Dynamics in Mesoporous ZnO, SnO₂, and TiO₂ Films Used in Dye-Sensitized Solar Cells. *ACS nano* **2011**, *5* (6), 5158-5166. DOI: 10.1021/nn201243y.
- (49) Wang, K.; Olthof, S.; Subhani, W. S.; Jiang, X.; Cao, Y.; Duan, L.; Wang, H.; Du, M.; Liu, S. Novel inorganic electron transport layers for planar perovskite solar cells: Progress and prospective. *Nano Energy* **2020**, *68*, 104289. DOI: <https://doi.org/10.1016/j.nanoen.2019.104289>.
- (50) Leijtens, T.; Eperon, G. E.; Pathak, S.; Abate, A.; Lee, M. M.; Snaith, H. J. J. N. c. Overcoming ultraviolet light instability of sensitized TiO₂ with meso-superstructured organometal tri-halide perovskite solar cells. **2013**, *4* (1), 1-8.
- (51) Zheng, X.; Chen, B.; Dai, J.; Fang, Y.; Bai, Y.; Lin, Y.; Wei, H.; Zeng, Xiao C.; Huang, J. Defect passivation in hybrid perovskite solar cells using quaternary ammonium halide anions and cations. *Nature Energy* **2017**, *2* (7), 17102. DOI: 10.1038/nenergy.2017.102.
- (52) Wu, Y.; Yang, X.; Chen, W.; Yue, Y.; Cai, M.; Xie, F.; Bi, E.; Islam, A.; Han, L. Perovskite solar cells with 18.21% efficiency and area over 1 cm² fabricated by heterojunction engineering. *Nature Energy* **2016**, *1* (11), 16148. DOI: 10.1038/nenergy.2016.148.

- (53) Niu, G.; Guo, X.; Wang, L. Review of recent progress in chemical stability of perovskite solar cells. *Journal of Materials Chemistry A* **2015**, *3* (17), 8970-8980, 10.1039/C4TA04994B. DOI: 10.1039/C4TA04994B.
- (54) Docampo, P.; Ball, J. M.; Darwich, M.; Eperon, G. E.; Snaith, H. J. J. N. c. Efficient organometal trihalide perovskite planar-heterojunction solar cells on flexible polymer substrates. **2013**, *4* (1), 1-6.
- (55) Dualeh, A.; Tétreault, N.; Moehl, T.; Gao, P.; Nazeeruddin, M. K.; Grätzel, M. Effect of Annealing Temperature on Film Morphology of Organic-Inorganic Hybrid Perovskite Solid-State Solar Cells. *Advanced Functional Materials* **2014**, *24* (21), 3250-3258. DOI: 10.1002/adfm.201304022.
- (56) Cho, A.-N.; Park, N.-G. Impact of Interfacial Layers in Perovskite Solar Cells. **2017**, *10* (19), 3687-3704. DOI: <https://doi.org/10.1002/cssc.201701095>.
- (57) Cao, X.; Zhi, L.; Jia, Y.; Li, Y.; Zhao, K.; Cui, X.; Ci, L.; Zhuang, D.; Wei, J. A Review of the Role of Solvents in Formation of High-Quality Solution-Processed Perovskite Films. *ACS applied materials & interfaces* **2019**, *11* (8), 7639-7654. DOI: 10.1021/acsami.8b16315.
- (58) Siegler, T. D.; Dawson, A.; Lobaccaro, P.; Ung, D.; Beck, M. E.; Nilsen, G.; Tinker, L. L. The Path to Perovskite Commercialization: A Perspective from the United States Solar Energy Technologies Office. *ACS Energy Letters* **2022**, *7* (5), 1728-1734. DOI: 10.1021/acsenergylett.2c00698.
- (59) Katz, E. A. Perovskite: Name Puzzle and German-Russian Odyssey of Discovery. **2020**, *103* (6), e2000061. DOI: <https://doi.org/10.1002/hlca.202000061>.
- (60) Nam-Gyu Park, M. G., Trutomu Miyasaka. Organic-Inorganic Halide Perovskite Photovoltaics. *Springer Cham* **2016**. DOI: 10.1007/978-3-319-35114-8.
- (61) Goldschmidt, V. M. Die Gesetze der Krystallochemie. *Naturwissenschaften* **1926**, *14* (21), 477-485. DOI: 10.1007/BF01507527.
- (62) Li, Z.; Yang, M.; Park, J.-S.; Wei, S.-H.; Berry, J. J.; Zhu, K. Stabilizing Perovskite Structures by Tuning Tolerance Factor: Formation of Formamidinium and Cesium Lead Iodide Solid-State Alloys. *Chemistry of Materials* **2016**, *28* (1), 284-292. DOI: 10.1021/acs.chemmater.5b04107.
- (63) Li, C.; Soh, K. C. K.; Wu, P. Formability of ABO₃ perovskites. *Journal of Alloys and Compounds* **2004**, *372* (1), 40-48. DOI: <https://doi.org/10.1016/j.jallcom.2003.10.017>.
- (64) Misra, R. K.; Aharon, S.; Li, B.; Mogilyansky, D.; Visoly-Fisher, I.; Etgar, L.; Katz, E. A. Temperature- and Component-Dependent Degradation of Perovskite Photovoltaic Materials under Concentrated Sunlight. *The journal of physical chemistry letters* **2015**, *6* (3), 326-330. DOI: 10.1021/jz502642b.
- (65) Azpiroz, J. M.; Mosconi, E.; Bisquert, J.; De Angelis, F. Defect migration in methylammonium lead iodide and its role in perovskite solar cell operation. *Energy & Environmental Science* **2015**, *8* (7), 2118-2127, 10.1039/C5EE01265A. DOI: 10.1039/C5EE01265A.
- (66) Elumalai, N. K.; Uddin, A. Hysteresis in organic-inorganic hybrid perovskite solar cells. *Solar Energy Materials and Solar Cells* **2016**, *157*, 476-509. DOI: <https://doi.org/10.1016/j.solmat.2016.06.025>.
- (67) Pellet, N.; Gao, P.; Gregori, G.; Yang, T. Y.; Nazeeruddin, M. K.; Maier, J.; Grätzel, M. J. A. c. Mixed-organic-cation Perovskite photovoltaics for enhanced solar-light harvesting. **2014**, *126* (12), 3215-3221.
- (68) Saliba, M.; Matsui, T.; Seo, J.-Y.; Domanski, K.; Correa-Baena, J.-P.; Nazeeruddin, M. K.; Zakeeruddin, S. M.; Tress, W.; Abate, A.; Hagfeldt, A.; et al. Cesium-containing triple cation perovskite solar cells: improved stability, reproducibility and high efficiency. *Energy & Environmental Science* **2016**, *9* (6), 1989-1997, 10.1039/C5EE03874J. DOI: 10.1039/C5EE03874J.

- (69) Byranvand, M. M.; Otero-Martínez, C.; Ye, J.; Zuo, W.; Manna, L.; Saliba, M.; Hoyer, R. L. Z.; Polavarapu, L. Recent Progress in Mixed A-Site Cation Halide Perovskite Thin-Films and Nanocrystals for Solar Cells and Light-Emitting Diodes. **2022**, *10* (14), 2200423. DOI: <https://doi.org/10.1002/adom.202200423>.
- (70) Binek, A.; Hanusch, F. C.; Docampo, P.; Bein, T. Stabilization of the Trigonal High-Temperature Phase of Formamidinium Lead Iodide. *The journal of physical chemistry letters* **2015**, *6* (7), 1249-1253. DOI: 10.1021/acs.jpcllett.5b00380.
- (71) Ghosh, D.; Smith, A. R.; Walker, A. B.; Islam, M. S. Mixed A-Cation Perovskites for Solar Cells: Atomic-Scale Insights Into Structural Distortion, Hydrogen Bonding, and Electronic Properties. *Chemistry of Materials* **2018**, *30* (15), 5194-5204. DOI: 10.1021/acs.chemmater.8b01851.
- (72) Doherty, T. A. S.; Nagane, S.; Kubicki, D. J.; Jung, Y.-K.; Johnstone, D. N.; Iqbal, A. N.; Guo, D.; Frohna, K.; Danaie, M.; Tennyson, E. M.; et al. Stabilized tilted-octahedra halide perovskites inhibit local formation of performance-limiting phases. **2021**, *374* (6575), 1598-1605. DOI: doi:10.1126/science.abl4890.
- (73) Mozur, E. M.; Neilson, J. R. Cation Dynamics in Hybrid Halide Perovskites. **2021**, *51* (1), 269-291. DOI: 10.1146/annurev-matsci-080819-012808.
- (74) Chen, C.; Song, Z.; Xiao, C.; Awni, R. A.; Yao, C.; Shrestha, N.; Li, C.; Bista, S. S.; Zhang, Y.; Chen, L.; et al. Arylammonium-Assisted Reduction of the Open-Circuit Voltage Deficit in Wide-Bandgap Perovskite Solar Cells: The Role of Suppressed Ion Migration. *ACS Energy Letters* **2020**, *5* (8), 2560-2568. DOI: 10.1021/acsenerylett.0c01350.
- (75) Pavlovets, I. M.; Brennan, M. C.; Draguta, S.; Ruth, A.; Moot, T.; Christians, J. A.; Aleshire, K.; Harvey, S. P.; Toso, S.; Nanayakkara, S. U.; et al. Suppressing Cation Migration in Triple-Cation Lead Halide Perovskites. *ACS Energy Letters* **2020**, *5* (9), 2802-2810. DOI: 10.1021/acsenerylett.0c01207.
- (76) Cao, J.; Tao, S. X.; Bobbert, P. A.; Wong, C. P.; Zhao, N. J. A. M. Interstitial occupancy by extrinsic alkali cations in perovskites and its impact on ion migration. **2018**, *30* (26), 1707350.
- (77) Abdi-Jalebi, M.; Andaji-Garmaroudi, Z.; Cacovich, S.; Stavarakas, C.; Philippe, B.; Richter, J. M.; Alsari, M.; Booker, E. P.; Hutter, E. M.; Pearson, A. J. J. N. Maximizing and stabilizing luminescence from halide perovskites with potassium passivation. **2018**, *555* (7697), 497-501.
- (78) Schelhas, L. T.; Li, Z.; Christians, J. A.; Goyal, A.; Kairys, P.; Harvey, S. P.; Kim, D. H.; Stone, K. H.; Luther, J. M.; Zhu, K. J. E.; et al. Insights into operational stability and processing of halide perovskite active layers. **2019**, *12* (4), 1341-1348.
- (79) Li, N.; Luo, Y.; Chen, Z.; Niu, X.; Zhang, X.; Lu, J.; Kumar, R.; Jiang, J.; Liu, H.; Guo, X. J. J. Microscopic degradation in formamidinium-cesium lead iodide perovskite solar cells under operational stressors. **2020**, *4* (8), 1743-1758.
- (80) Saidaminov, M. I.; Williams, K.; Wei, M.; Johnston, A.; Quintero-Bermudez, R.; Vafaie, M.; Pina, J. M.; Proppe, A. H.; Hou, Y.; Walters, G. J. N. m. Multi-cation perovskites prevent carrier reflection from grain surfaces. **2020**, *19* (4), 412-418.
- (81) Liu, L.; Lu, J.; Wang, H.; Cui, Z.; Giorgi, G.; Bai, Y.; Chen, Q. A-site phase segregation in mixed cation perovskite. *Materials Reports: Energy* **2021**, *1* (4), 100064. DOI: <https://doi.org/10.1016/j.matre.2021.100064>.
- (82) Ghosh, D.; Acharya, D.; Zhou, L.; Nie, W.; Prezhdo, O. V.; Tretiak, S.; Neukirch, A. J. J. T. J. o. P. C. L. Lattice expansion in hybrid perovskites: Effect on optoelectronic properties and charge carrier dynamics. **2019**, *10* (17), 5000-5007.
- (83) Bakulin, A. A.; Selig, O.; Bakker, H. J.; Rezus, Y. L.; Müller, C.; Glaser, T.; Lovrincic, R.; Sun, Z.; Chen, Z.; Walsh, A. J. T. j. o. p. c. l. Real-time observation of organic cation reorientation in methylammonium lead iodide perovskites. **2015**, *6* (18), 3663-3669.

- (84) Selig, O.; Sadhanala, A.; Müller, C.; Lovrincic, R.; Chen, Z.; Rezus, Y. L.; Frost, J. M.; Jansen, T. L.; Bakulin, A. A. J. J. o. t. A. C. S. Organic cation rotation and immobilization in pure and mixed methylammonium lead-halide perovskites. **2017**, *139* (11), 4068-4074.
- (85) Stranks, S. D.; Eperon, G. E.; Grancini, G.; Menelaou, C.; Alcocer, M. J. P.; Leijtens, T.; Herz, L. M.; Petrozza, A.; Snaith, H. J. Electron-Hole Diffusion Lengths Exceeding 1 Micrometer in an Organometal Trihalide Perovskite Absorber. **2013**, *342* (6156), 341-344. DOI: doi:10.1126/science.1243982.
- (86) Snaith, H. J.; Abate, A.; Ball, J. M.; Eperon, G. E.; Leijtens, T.; Noel, N. K.; Stranks, S. D.; Wang, J. T.-W.; Wojciechowski, K.; Zhang, W. Anomalous Hysteresis in Perovskite Solar Cells. *The journal of physical chemistry letters* **2014**, *5* (9), 1511-1515. DOI: 10.1021/jz500113x.
- (87) Knight, A. J.; Borchert, J.; Oliver, R. D. J.; Patel, J. B.; Radaelli, P. G.; Snaith, H. J.; Johnston, M. B.; Herz, L. M. Halide Segregation in Mixed-Halide Perovskites: Influence of A-Site Cations. *ACS Energy Letters* **2021**, *6* (2), 799-808. DOI: 10.1021/acseenergylett.0c02475.
- (88) Chiang, C.-H.; Lin, J.-W.; Wu, C.-G. J. J. o. M. C. A. One-step fabrication of a mixed-halide perovskite film for a high-efficiency inverted solar cell and module. **2016**, *4* (35), 13525-13533.
- (89) Isikgor, F. H.; Li, B.; Zhu, H.; Xu, Q.; Ouyang, J. J. J. o. M. C. A. High performance planar perovskite solar cells with a perovskite of mixed organic cations and mixed halides, MA_{1-x}FA_xPb_{1-y}Cl_y. **2016**, *4* (32), 12543-12553.
- (90) Tonui, P.; Oseni, S. O.; Sharma, G.; Yan, Q.; Mola, G. T. J. R.; Reviews, S. E. Perovskites photovoltaic solar cells: An overview of current status. **2018**, *91*, 1025-1044.
- (91) Liu, S.; Guan, Y.; Sheng, Y.; Hu, Y.; Rong, Y.; Mei, A.; Han, H. A Review on Additives for Halide Perovskite Solar Cells. *Advanced Energy Materials* **2020**, *10* (13). DOI: 10.1002/aenm.201902492 WorldCat.org.
- (92) Jiang, Q.; Zhao, Y.; Zhang, X.; Yang, X.; Chen, Y.; Chu, Z.; Ye, Q.; Li, X.; Yin, Z.; You, J. Surface passivation of perovskite film for efficient solar cells. *Nature Photonics* **2019**, *13* (7), 460-466. DOI: 10.1038/s41566-019-0398-2.
- (93) Quan, L. N.; Yuan, M.; Comin, R.; Voznyy, O.; Beauregard, E. M.; Hoogland, S.; Buin, A.; Kirmani, A. R.; Zhao, K.; Amassian, A.; et al. Ligand-Stabilized Reduced-Dimensionality Perovskites. *Journal of the American Chemical Society* **2016**, *138* (8), 2649-2655. DOI: 10.1021/jacs.5b11740.
- (94) Tsai, H.; Nie, W.; Blancon, J. C.; Stoumpos, C. C.; Asadpour, R.; Harutyunyan, B.; Neukirch, A. J.; Verduzco, R.; Crochet, J. J.; Tretiak, S.; et al. High-efficiency two-dimensional Ruddlesden-Popper perovskite solar cells. *Nature* **2016**, *536* (7616), 312-316. DOI: 10.1038/nature18306 From NLM.
- (95) Mao, L.; Ke, W.; Pedesseau, L.; Wu, Y.; Katan, C.; Even, J.; Wasielewski, M. R.; Stoumpos, C. C.; Kanatzidis, M. G. Hybrid Dion-Jacobson 2D Lead Iodide Perovskites. *Journal of the American Chemical Society* **2018**, *140* (10), 3775-3783. DOI: 10.1021/jacs.8b00542.
- (96) Lee, J. W.; Dai, Z.; Han, T. H.; Choi, C.; Chang, S. Y.; Lee, S. J.; De Marco, N.; Zhao, H.; Sun, P.; Huang, Y.; et al. 2D perovskite stabilized phase-pure formamidinium perovskite solar cells. *Nat Commun* **2018**, *9* (1), 3021. DOI: 10.1038/s41467-018-05454-4 From NLM.
- (97) Li, N.; Zhu, Z.; Dong, Q.; Li, J.; Yang, Z.; Chueh, C.-C.; Jen, A. K.-Y.; Wang, L. Enhanced Moisture Stability of Cesium-Containing Compositional Perovskites by a Feasible Interfacial Engineering. **2017**, *4* (20), 1700598. DOI: <https://doi.org/10.1002/admi.201700598>.
- (98) Bai, Y.; Xiao, S.; Hu, C.; Zhang, T.; Meng, X.; Lin, H.; Yang, Y.; Yang, S. Dimensional Engineering of a Graded 3D-2D Halide Perovskite Interface Enables Ultrahigh Voc Enhanced Stability in the p-i-n Photovoltaics. **2017**, *7* (20), 1701038. DOI: <https://doi.org/10.1002/aenm.201701038>.

- (99) Yoo, H.-S.; Park, N.-G. Post-treatment of perovskite film with phenylalkylammonium iodide for hysteresis-less perovskite solar cells. *Solar Energy Materials and Solar Cells* **2018**, *179*, 57-65. DOI: <https://doi.org/10.1016/j.solmat.2018.02.015>.
- (100) Ghahremani, A. H.; Martin, B.; Gupta, A.; Bahadur, J.; Ankireddy, K.; Druffel, T. Rapid fabrication of perovskite solar cells through intense pulse light annealing of SnO₂ and triple cation perovskite thin films. *Materials & Design* **2020**, *185*, 108237. DOI: <https://doi.org/10.1016/j.matdes.2019.108237>.
- (101) Ankireddy, K.; Ghahremani, A. H.; Martin, B.; Gupta, G.; Druffel, T. Rapid thermal annealing of CH₃NH₃PbI₃ perovskite thin films by intense pulsed light with aid of diiodomethane additive. *Journal of Materials Chemistry A* **2018**, *6* (20), 9378-9383. DOI: 10.1039/c8ta01237g.
- (102) Xu, W.; Piper, R. T.; Zheng, Y.; Malko, A. V.; Hsu, J. W. P. Elucidating Diiodomethane-Induced Improvement in Photonically Cured MAPbI₃ Solar Cells. *ACS Applied Energy Materials* **2022**, *5* (6), 7328-7334. DOI: 10.1021/acsaem.2c00848.
- (103) Lai, T.-H.; Tsang, S.-W.; Manders, J. R.; Chen, S.; So, F. Properties of interlayer for organic photovoltaics. *Materials Today* **2013**, *16* (11), 424-432. DOI: <https://doi.org/10.1016/j.mattod.2013.10.001>.
- (104) Rombach, F. M.; Haque, S. A.; Macdonald, T. J. Lessons learned from spiro-OMeTAD and PTAA in perovskite solar cells. *Energy & Environmental Science* **2021**, *14* (10), 5161-5190, 10.1039/D1EE02095A. DOI: 10.1039/D1EE02095A.
- (105) Energy, U. S. D. o. Quadrennial Technology Review: Roll to Roll Processing Technology Assessments. *Quadrennial Technology Review* **2015**.
- (106) Higuchi, H.; Negami, T. J. J. J. o. A. P. Largest highly efficient 203× 203 mm² CH₃NH₃PbI₃ perovskite solar modules. **2018**, *57* (8S3), 08RE11.
- (107) Razza, S.; Di Giacomo, F.; Matteocci, F.; Cina, L.; Palma, A. L.; Casaluci, S.; Cameron, P.; D'epifanio, A.; Licocchia, S.; Reale, A. J. J. o. P. S. Perovskite solar cells and large area modules (100 cm²) based on an air flow-assisted PbI₂ blade coating deposition process. **2015**, *277*, 286-291.
- (108) Di Giacomo, F.; Shanmugam, S.; Fledderus, H.; Bruijnaers, B. J.; Verhees, W. J.; Dorenkamper, M. S.; Veenstra, S. C.; Qiu, W.; Gehlhaar, R.; Merckx, T. J. S. E. M.; et al. Up-scalable sheet-to-sheet production of high efficiency perovskite module and solar cells on 6-in. substrate using slot die coating. **2018**, *181*, 53-59.
- (109) Yang, J.; Hu, Y.; Yan, B.; Chang, J.; Yao, J.; Han, H. Large-area Perovskite Optoelectronic Devices and the Fabrication Techniques. In *Perovskite Materials and Devices*, 2022; pp 433-477.
- (110) Green, M. A.; Hishikawa, Y.; Dunlop, E. D.; Levi, D. H.; Hohl-Ebinger, J.; Ho-Baillie, A. W. Y. Solar cell efficiency tables (version 52). **2018**, *26* (7), 427-436. DOI: <https://doi.org/10.1002/pip.3040>.
- (111) Heo, J. H.; Lee, M. H.; Jang, M. H.; Im, S. H. J. J. o. M. C. A. Highly efficient CH₃NH₃PbI_{3-x}Cl_x mixed halide perovskite solar cells prepared by re-dissolution and crystal grain growth via spray coating. **2016**, *4* (45), 17636-17642.
- (112) Green, M. A.; Dunlop, E. D.; Hohl-Ebinger, J.; Yoshita, M.; Kopidakis, N.; Hao, X. J. P. i. P. R.; Applications. Solar cell efficiency tables (version 56). **2020**, *28* (7), 629-638.
- (113) Japan's, N. J. B.-F. P. Panasonic Achieve the World's Highest Conversion Efficiency of 16.09% for Largest-area Perovskite Solar Cell Module. **2020**.
- (114) De Rossi, F.; Baker, J. A.; Beynon, D.; Hooper, K. E. A.; Meroni, S. M. P.; Williams, D.; Wei, Z.; Yasin, A.; Charbonneau, C.; Jewell, E. H.; et al. All Printable Perovskite Solar Modules with 198 cm² Active Area and Over 6% Efficiency. **2018**, *3* (11), 1800156. DOI: <https://doi.org/10.1002/admt.201800156>.

- (115) Heo, J. H.; Zhang, F.; Xiao, C.; Heo, S. J.; Park, J. K.; Berry, J. J.; Zhu, K.; Im, S. H. J. J. Efficient and stable graded CsPbI₃-xBr_x perovskite solar cells and submodules by orthogonal processable spray coating. **2021**, *5* (2), 481-494.
- (116) Tait, J. G.; Manghooli, S.; Qiu, W.; Rakocevic, L.; Kootstra, L.; Jaysankar, M.; Masse de la Huerta, C. A.; Paetzold, U. W.; Gehlhaar, R.; Cheyng, D.; et al. Rapid composition screening for perovskite photovoltaics via concurrently pumped ultrasonic spray coating. *Journal of Materials Chemistry A* **2016**, *4* (10), 3792-3797, 10.1039/C6TA00739B. DOI: 10.1039/C6TA00739B.
- (117) Bu, T.; Li, J.; Li, H.; Tian, C.; Su, J.; Tong, G.; Ono, L. K.; Wang, C.; Lin, Z.; Chai, N. J. S. Lead halide-templated crystallization of methylamine-free perovskite for efficient photovoltaic modules. **2021**, *372* (6548), 1327-1332.
- (118) Deng, Y.; Zheng, X.; Bai, Y.; Wang, Q.; Zhao, J.; Huang, J. J. N. E. Surfactant-controlled ink drying enables high-speed deposition of perovskite films for efficient photovoltaic modules. **2018**, *3* (7), 560-566.
- (119) Chen, S.; Dai, X.; Xu, S.; Jiao, H.; Zhao, L.; Huang, J. J. S. Stabilizing perovskite-substrate interfaces for high-performance perovskite modules. **2021**, *373* (6557), 902-907.
- (120) Yaghoobi Nia, N.; Giordano, F.; Zendejdel, M.; Cinà, L.; Palma, A. L.; Medaglia, P. G.; Zakeeruddin, S. M.; Grätzel, M.; Di Carlo, A. Solution-based heteroepitaxial growth of stable mixed cation/anion hybrid perovskite thin film under ambient condition via a scalable crystal engineering approach. *Nano Energy* **2020**, *69*, 104441. DOI: <https://doi.org/10.1016/j.nanoen.2019.104441>.
- (121) Vak, D.; Hwang, K.; Faulks, A.; Jung, Y.-S.; Clark, N.; Kim, D.-Y.; Wilson, G. J.; Watkins, S. E. 3D Printer Based Slot-Die Coater as a Lab-to-Fab Translation Tool for Solution-Processed Solar Cells. **2015**, *5* (4), 1401539. DOI: <https://doi.org/10.1002/aenm.201401539>.
- (122) Bi, E.; Tang, W.; Chen, H.; Wang, Y.; Barbaud, J.; Wu, T.; Kong, W.; Tu, P.; Zhu, H.; Zeng, X.; et al. Efficient Perovskite Solar Cell Modules with High Stability Enabled by Iodide Diffusion Barriers. *Joule* **2019**, *3* (11), 2748-2760. DOI: <https://doi.org/10.1016/j.joule.2019.07.030>.
- (123) Yang, M.; Li, Z.; Reese, M. O.; Reid, O. G.; Kim, D. H.; Siol, S.; Klein, T. R.; Yan, Y.; Berry, J. J.; van Hest, M. F. A. M.; et al. Perovskite ink with wide processing window for scalable high-efficiency solar cells. *Nature Energy* **2017**, *2* (5), 17038. DOI: 10.1038/nenergy.2017.38.
- (124) Cai, L.; Liang, L.; Wu, J.; Ding, B.; Gao, L.; Fan, B. Large area perovskite solar cell module. *Journal of Semiconductors* **2017**, *38* (1), 014006. DOI: 10.1088/1674-4926/38/1/014006.
- (125) Guo, F.; Qiu, S.; Hu, J.; Wang, H.; Cai, B.; Li, J.; Yuan, X.; Liu, X.; Forberich, K.; Brabec, C. J.; et al. A Generalized Crystallization Protocol for Scalable Deposition of High-Quality Perovskite Thin Films for Photovoltaic Applications. **2019**, *6* (17), 1901067. DOI: <https://doi.org/10.1002/advs.201901067>.
- (126) Hu, J.; Wang, C.; Qiu, S.; Zhao, Y.; Gu, E.; Zeng, L.; Yang, Y.; Li, C.; Liu, X.; Forberich, K.; et al. Spontaneously Self-Assembly of a 2D/3D Heterostructure Enhances the Efficiency and Stability in Printed Perovskite Solar Cells. **2020**, *10* (17), 2000173. DOI: <https://doi.org/10.1002/aenm.202000173>.
- (127) Lee, D.; Jung, Y. S.; Heo, Y. J.; Lee, S.; Hwang, K.; Jeon, Y. J.; Kim, J. E.; Park, J.; Jung, G. Y.; Kim, D. Y. Slot-Die Coated Perovskite Films Using Mixed Lead Precursors for Highly Reproducible and Large-Area Solar Cells. *ACS applied materials & interfaces* **2018**, *10* (18), 16133-16139. DOI: 10.1021/acsami.8b02549 From NLM.
- (128) Xu, Z.; Chen, R.; Wu, Y.; He, R.; Yin, J.; Lin, W.; Wu, B.; Li, J.; Zheng, N. Br-containing alkyl ammonium salt-enabled scalable fabrication of high-quality perovskite films for efficient and stable perovskite modules. *Journal of Materials Chemistry A* **2019**, *7* (47), 26849-26857, 10.1039/C9TA09101G. DOI: 10.1039/C9TA09101G.

- (129) Chen, R.; Wu, Y.; Wang, Y.; Xu, R.; He, R.; Fan, Y.; Huang, X.; Yin, J.; Wu, B.; Li, J.; et al. Crown Ether-Assisted Growth and Scaling Up of FACsPbI₃ Films for Efficient and Stable Perovskite Solar Modules. **2021**, *31* (11), 2008760. DOI: <https://doi.org/10.1002/adfm.202008760>.
- (130) Du, M.; Zhu, X.; Wang, L.; Wang, H.; Feng, J.; Jiang, X.; Cao, Y.; Sun, Y.; Duan, L.; Jiao, Y.; et al. High-Pressure Nitrogen-Extraction and Effective Passivation to Attain Highest Large-Area Perovskite Solar Module Efficiency. **2020**, *32* (47), 2004979. DOI: <https://doi.org/10.1002/adma.202004979>.
- (131) Liang, Z.; Zhang, S.; Xu, X.; Wang, N.; Wang, J.; Wang, X.; Bi, Z.; Xu, G.; Yuan, N.; Ding, J. A large grain size perovskite thin film with a dense structure for planar heterojunction solar cells via spray deposition under ambient conditions. *RSC Advances* **2015**, *5* (74), 60562-60569, 10.1039/C5RA09110A. DOI: 10.1039/C5RA09110A.
- (132) Li, P.; Zhang, Y.; Liang, C.; Xing, G.; Liu, X.; Li, F.; Liu, X.; Hu, X.; Shao, G.; Song, Y. Phase Pure 2D Perovskite for High-Performance 2D–3D Heterostructured Perovskite Solar Cells. **2018**, *30* (52), 1805323. DOI: <https://doi.org/10.1002/adma.201805323>.
- (133) Fan, Y.; Fang, J.; Chang, X.; Tang, M.-C.; Barrit, D.; Xu, Z.; Jiang, Z.; Wen, J.; Zhao, H.; Niu, T. J. Scalable ambient fabrication of high-performance CsPbI₂Br solar cells. **2019**, *3* (10), 2485-2502.
- (134) Huang, H.; Shi, J.; Zhu, L.; Li, D.; Luo, Y.; Meng, Q. Two-step ultrasonic spray deposition of CH₃NH₃PbI₃ for efficient and large-area perovskite solar cell. *Nano Energy* **2016**, *27*, 352-358.
- (135) Lin, D.; Zhang, T.; Wang, J.; Long, M.; Xie, F.; Chen, J.; Wu, B.; Shi, T.; Yan, K.; Xie, W.; et al. Stable and scalable 3D-2D planar heterojunction perovskite solar cells via vapor deposition. *Nano Energy* **2019**, *59*, 619-625. DOI: <https://doi.org/10.1016/j.nanoen.2019.03.014>.
- (136) Li, J.; Munir, R.; Fan, Y.; Niu, T.; Liu, Y.; Zhong, Y.; Yang, Z.; Tian, Y.; Liu, B.; Sun, J. J. Phase transition control for high-performance blade-coated perovskite solar cells. **2018**, *2* (7), 1313-1330.
- (137) He, M.; Li, B.; Cui, X.; Jiang, B.; He, Y.; Chen, Y.; O’Neil, D.; Szymanski, P.; Ei-Sayed, M. A.; Huang, J.; et al. Meniscus-assisted solution printing of large-grained perovskite films for high-efficiency solar cells. *Nature Communications* **2017**, *8* (1), 16045. DOI: 10.1038/ncomms16045.
- (138) Wei, Z.; Chen, H.; Yan, K.; Yang, S. Inkjet Printing and Instant Chemical Transformation of a CH₃NH₃PbI₃/Nanocarbon Electrode and Interface for Planar Perovskite Solar Cells. **2014**, *53* (48), 13239-13243. DOI: <https://doi.org/10.1002/anie.201408638>.
- (139) Hwang, K.; Jung, Y.-S.; Heo, Y.-J.; Scholes, F. H.; Watkins, S. E.; Subbiah, J.; Jones, D. J.; Kim, D.-Y.; Vak, D. Toward Large Scale Roll-to-Roll Production of Fully Printed Perovskite Solar Cells. **2015**, *27* (7), 1241-1247. DOI: <https://doi.org/10.1002/adma.201404598>.
- (140) Mathies, F.; Abzieher, T.; Hochstuhl, A.; Glaser, K.; Colsmann, A.; Paetzold, U. W.; Hernandez-Sosa, G.; Lemmer, U.; Quintilla, A. Multipass inkjet printed planar methylammonium lead iodide perovskite solar cells. *Journal of Materials Chemistry A* **2016**, *4* (48), 19207-19213, 10.1039/C6TA07972E. DOI: 10.1039/C6TA07972E.
- (141) Wu, W.-Q.; Wang, Q.; Fang, Y.; Shao, Y.; Tang, S.; Deng, Y.; Lu, H.; Liu, Y.; Li, T.; Yang, Z.; et al. Molecular doping enabled scalable blading of efficient hole-transport-layer-free perovskite solar cells. *Nature Communications* **2018**, *9* (1), 1625. DOI: 10.1038/s41467-018-04028-8.
- (142) Zuo, C.; Scully, A. D.; Vak, D.; Tan, W.; Jiao, X.; McNeill, C. R.; Angmo, D.; Ding, L.; Gao, M. Self-Assembled 2D Perovskite Layers for Efficient Printable Solar Cells. **2019**, *9* (4), 1803258. DOI: <https://doi.org/10.1002/aenm.201803258>.
- (143) Deng, Y.; Peng, E.; Shao, Y.; Xiao, Z.; Dong, Q.; Huang, J. J. E.; Science, E. Scalable fabrication of efficient organolead trihalide perovskite solar cells with doctor-bladed active layers. **2015**, *8* (5), 1544-1550.

- (144) Das, S.; Yang, B.; Gu, G.; Joshi, P. C.; Ivanov, I. N.; Rouleau, C. M.; Aytug, T.; Geohegan, D. B.; Xiao, K. High-Performance Flexible Perovskite Solar Cells by Using a Combination of Ultrasonic Spray-Coating and Low Thermal Budget Photonic Curing. *ACS Photonics* **2015**, *2* (6), 680-686. DOI: 10.1021/acsp Photonics.5b00119.
- (145) Whitaker, J. B.; Kim, D. H.; Larson, Bryon W.; Zhang, F.; Berry, J. J.; van Hest, M. F. A. M.; Zhu, K. Scalable slot-die coating of high performance perovskite solar cells. *Sustainable Energy & Fuels* **2018**, *2* (11), 2442-2449, 10.1039/C8SE00368H. DOI: 10.1039/C8SE00368H.
- (146) Liu, J.; Shirai, Y.; Yang, X.; Yue, Y.; Chen, W.; Wu, Y.; Islam, A.; Han, L. High-Quality Mixed-Organic-Cation Perovskites from a Phase-Pure Non-stoichiometric Intermediate (FAI)_{1-x}PbI₂ for Solar Cells. *Advanced materials (Deerfield Beach, Fla.)* **2015**, *27* (33), 4918-4923. DOI: 10.1002/adma.201501489 PubMed.
- (147) Li, S.-G.; Jiang, K.-J.; Su, M.-J.; Cui, X.-P.; Huang, J.-H.; Zhang, Q.-Q.; Zhou, X.-Q.; Yang, L.-M.; Song, Y.-L. Inkjet printing of CH₃NH₃PbI₃ on a mesoscopic TiO₂ film for highly efficient perovskite solar cells. *Journal of Materials Chemistry A* **2015**, *3* (17), 9092-9097, 10.1039/C4TA05675B. DOI: 10.1039/C4TA05675B.
- (148) Liang, C.; Li, P.; Gu, H.; Zhang, Y.; Li, F.; Song, Y.; Shao, G.; Mathews, N.; Xing, G. One-Step Inkjet Printed Perovskite in Air for Efficient Light Harvesting. **2018**, *2* (2), 1700217. DOI: <https://doi.org/10.1002/solr.201700217>.
- (149) Xia, X.; Wu, W.; Li, H.; Zheng, B.; Xue, Y.; Xu, J.; Zhang, D.; Gao, C.; Liu, X. Spray reaction prepared FA_{1-x}Cs_xPbI₃ solid solution as a light harvester for perovskite solar cells with improved humidity stability. *RSC Advances* **2016**, *6* (18), 14792-14798, 10.1039/C5RA23359C. DOI: 10.1039/C5RA23359C.
- (150) Barrows, A. T.; Pearson, A. J.; Kwak, C. K.; Dunbar, A. D. F.; Buckley, A. R.; Lidzey, D. G. Efficient planar heterojunction mixed-halide perovskite solar cells deposited via spray-deposition. *Energy & Environmental Science* **2014**, *7* (9), 2944-2950, 10.1039/C4EE01546K. DOI: 10.1039/C4EE01546K.
- (151) Tang, S.; Deng, Y.; Zheng, X.; Bai, Y.; Fang, Y.; Dong, Q.; Wei, H.; Huang, J. Composition Engineering in Doctor-Blading of Perovskite Solar Cells. **2017**, *7* (18), 1700302. DOI: <https://doi.org/10.1002/aenm.201700302>.
- (152) Le Berre, M.; Chen, Y.; Baigl, D. J. L. From convective assembly to Landau–Levich deposition of multilayered phospholipid films of controlled thickness. **2009**, *25* (5), 2554-2557.
- (153) Kim, J. H.; Williams, S. T.; Cho, N.; Chueh, C. C.; Jen, A. K. Y. J. A. e. m. Enhanced environmental stability of planar heterojunction perovskite solar cells based on blade-coating. **2015**, *5* (4), 1401229.
- (154) Liu, C.; Cheng, Y.-B.; Ge, Z. Understanding of perovskite crystal growth and film formation in scalable deposition processes. *Chemical Society Reviews* **2020**, *49* (6), 1653-1687. DOI: 10.1039/c9cs00711c WorldCat.org.
- (155) Kwon, S. G.; Hyeon, T. Formation Mechanisms of Uniform Nanocrystals via Hot-Injection and Heat-Up Methods. *Small* **2011**, *7* (19), 2685-2702. DOI: 10.1002/smll.201002022 WorldCat.org.
- (156) Sugimoto, T. Preparation of monodispersed colloidal particles. *Advances in Colloid and Interface Science* **1987**, *28*, 65-108. DOI: [https://doi.org/10.1016/0001-8686\(87\)80009-X](https://doi.org/10.1016/0001-8686(87)80009-X).
- (157) Ostwald, W. J. Z. f. p. C. Über die vermeintliche Isomerie des roten und gelben Quecksilberoxyds und die Oberflächenspannung fester Körper. **1900**, *34* (1), 495-503.
- (158) Baldan, A. Review Progress in Ostwald ripening theories and their applications to nickel-base superalloys Part I: Ostwald ripening theories. *Journal of Materials Science* **2002**, *37* (11), 2171-2202. DOI: 10.1023/A:1015388912729.

- (159) Seo, Y.-H.; Kim, E.-C.; Cho, S.-P.; Kim, S.-S.; Na, S.-I. High-performance planar perovskite solar cells: Influence of solvent upon performance. *Applied Materials Today* **2017**, *9*, 598-604. DOI: <https://doi.org/10.1016/j.apmt.2017.11.003>.
- (160) Guo, X.; McCleese, C.; Kolodziej, C.; Samia, A. C. S.; Zhao, Y.; Burda, C. Identification and characterization of the intermediate phase in hybrid organic–inorganic MAPbI₃ perovskite. *Dalton Transactions* **2016**, *45* (9), 3806-3813, 10.1039/C5DT04420K. DOI: 10.1039/C5DT04420K.
- (161) Lee, J.-W.; Dai, Z.; Lee, C.; Lee, H. M.; Han, T.-H.; De Marco, N.; Lin, O.; Choi, C. S.; Dunn, B.; Koh, J.; et al. Tuning Molecular Interactions for Highly Reproducible and Efficient Formamidinium Perovskite Solar Cells via Adduct Approach. *Journal of the American Chemical Society* **2018**, *140* (20), 6317-6324. DOI: 10.1021/jacs.8b01037.
- (162) Yang, W. S.; Noh, J. H.; Jeon, N. J.; Kim, Y. C.; Ryu, S.; Seo, J.; Seok, S. I. SOLAR CELLS. High-performance photovoltaic perovskite layers fabricated through intramolecular exchange. *Science* **2015**, *348* (6240), 1234-1237. DOI: 10.1126/science.aaa9272 From NLM.
- (163) Stampelcoskie, K. G.; Manser, J. S.; Kamat, P. V. Dual nature of the excited state in organic–inorganic lead halide perovskites. *Energy & Environmental Science* **2015**, *8* (1), 208-215, 10.1039/C4EE02988G. DOI: 10.1039/C4EE02988G.
- (164) Sharenko, A.; Mackeen, C.; Jewell, L.; Bridges, F.; Toney, M. F. Evolution of Iodoplumbate Complexes in Methylammonium Lead Iodide Perovskite Precursor Solutions. *Chemistry of Materials* **2017**, *29* (3), 1315-1320. DOI: 10.1021/acs.chemmater.6b04917.
- (165) Cao, X.; Zhi, L.; Li, Y.; Cui, X.; Ci, L.; Ding, K.; Wei, J. Enhanced performance of perovskite solar cells by strengthening a self-embedded solvent annealing effect in perovskite precursor films. *RSC Advances* **2017**, *7* (77), 49144-49150, 10.1039/C7RA10294A. DOI: 10.1039/C7RA10294A.
- (166) Kim, H.-B.; Choi, H.; Jeong, J.; Kim, S.; Walker, B.; Song, S.; Kim, J. Y. Mixed solvents for the optimization of morphology in solution-processed, inverted-type perovskite/fullerene hybrid solar cells. *Nanoscale* **2014**, *6* (12), 6679-6683, 10.1039/C4NR00130C. DOI: 10.1039/C4NR00130C.
- (167) Xiao, S.; Bai, Y.; Meng, X.; Zhang, T.; Chen, H.; Zheng, X.; Hu, C.; Qu, Y.; Yang, S. Unveiling a Key Intermediate in Solvent Vapor Postannealing to Enlarge Crystalline Domains of Organometal Halide Perovskite Films. **2017**, *27* (12), 1604944. DOI: <https://doi.org/10.1002/adfm.201604944>.
- (168) Zhang, K.; Wang, Z.; Wang, G.; Wang, J.; Li, Y.; Qian, W.; Zheng, S.; Xiao, S.; Yang, S. A prenucleation strategy for ambient fabrication of perovskite solar cells with high device performance uniformity. *Nature Communications* **2020**, *11* (1), 1006. DOI: 10.1038/s41467-020-14715-0.
- (169) Yan, K.; Long, M.; Zhang, T.; Wei, Z.; Chen, H.; Yang, S.; Xu, J. Hybrid Halide Perovskite Solar Cell Precursors: Colloidal Chemistry and Coordination Engineering behind Device Processing for High Efficiency. *Journal of the American Chemical Society* **2015**, *137* (13), 4460-4468. DOI: 10.1021/jacs.5b00321.
- (170) Zhang, Y.; Gao, P.; Oveisi, E.; Lee, Y.; Jeangros, Q.; Grancini, G.; Paek, S.; Feng, Y.; Nazeeruddin, M. K. Pbl₂-HMPA Complex Pretreatment for Highly Reproducible and Efficient CH₃NH₃Pbl₃ Perovskite Solar Cells. *Journal of the American Chemical Society* **2016**, *138* (43), 14380-14387. DOI: 10.1021/jacs.6b08347 From NLM.
- (171) Fateev, S. A.; Petrov, A. A.; Khrustalev, V. N.; Dorovatovskii, P. V.; Zubavichus, Y. V.; Goodilin, E. A.; Tarasov, A. B. Solution Processing of Methylammonium Lead Iodide Perovskite from γ -Butyrolactone: Crystallization Mediated by Solvation Equilibrium. *Chemistry of Materials* **2018**, *30* (15), 5237-5244. DOI: 10.1021/acs.chemmater.8b01906.
- (172) Saidaminov, M. I.; Abdelhady, A. L.; Maculan, G.; Bakr, O. M. Retrograde solubility of formamidinium and methylammonium lead halide perovskites enabling rapid single crystal

growth. *Chemical Communications* **2015**, 51 (100), 17658-17661, 10.1039/C5CC06916E. DOI: 10.1039/C5CC06916E.

(173) Yao, Z.; Wang, W.; Shen, H.; Zhang, Y.; Luo, Q.; Yin, X.; Dai, X.; Li, J.; Lin, H. CH₃NH₃PbI₃ grain growth and interfacial properties in meso-structured perovskite solar cells fabricated by two-step deposition. *Science and technology of advanced materials* **2017**, 18 (1), 253-262. DOI: 10.1080/14686996.2017.1298974 From NLM.

(174) Im, J.-H.; Kim, H.-S.; Park, N.-G. Morphology-photovoltaic property correlation in perovskite solar cells: One-step versus two-step deposition of CH₃NH₃PbI₃. *APL Materials* **2014**, 2 (8), 081510. DOI: 10.1063/1.4891275 (accessed 2023/01/30).

(175) Chao, L.; Niu, T.; Gao, W.; Ran, C.; Song, L.; Chen, Y.; Huang, W. Solvent Engineering of the Precursor Solution toward Large-Area Production of Perovskite Solar Cells. **2021**, 33 (14), 2005410. DOI: <https://doi.org/10.1002/adma.202005410>.

(176) Deng, Y.; Van Brackle, C. H.; Dai, X.; Zhao, J.; Chen, B.; Huang, J. Tailoring solvent coordination for high-speed, room-temperature blading of perovskite photovoltaic films. **2019**, 5 (12), eaax7537. DOI: doi:10.1126/sciadv.aax7537.

(177) Ye, F.; Chen, H.; Xie, F.; Tang, W.; Yin, M.; He, J.; Bi, E.; Wang, Y.; Yang, X.; Han, L. Soft-cover deposition of scaling-up uniform perovskite thin films for high cost-performance solar cells. *Energy & Environmental Science* **2016**, 9 (7), 2295-2301, 10.1039/C6EE01411A. DOI: 10.1039/C6EE01411A.

(178) Kim, B. J.; Lee, S.; Jung, H. S. Recent progressive efforts in perovskite solar cells toward commercialization. *Journal of Materials Chemistry A* **2018**, 6 (26), 12215-12236, 10.1039/C8TA02159G. DOI: 10.1039/C8TA02159G.

(179) Kim, M.; Kim, G.-H.; Lee, T. K.; Choi, I. W.; Choi, H. W.; Jo, Y.; Yoon, Y. J.; Kim, J. W.; Lee, J.; Huh, D.; et al. Methylammonium Chloride Induces Intermediate Phase Stabilization for Efficient Perovskite Solar Cells. *Joule* **2019**, 3 (9), 2179-2192. DOI: <https://doi.org/10.1016/j.joule.2019.06.014>.

(180) Cao, X.; Zhi, L.; Li, Y.; Fang, F.; Cui, X.; Ci, L.; Ding, K.; Wei, J. Fabrication of Perovskite Films with Large Columnar Grains via Solvent-Mediated Ostwald Ripening for Efficient Inverted Perovskite Solar Cells. *ACS Applied Energy Materials* **2018**, 1 (2), 868-875. DOI: 10.1021/acsaem.7b00300.

(181) Cheng, P.; Xu, Z.; Li, J.; Liu, Y.; Fan, Y.; Yu, L.; Smilgies, D.-M.; Müller, C.; Zhao, K.; Liu, S. F. Highly Efficient Ruddlesden–Popper Halide Perovskite PA₂MA₄Pb₅I₁₆ Solar Cells. *ACS Energy Letters* **2018**, 3 (8), 1975-1982. DOI: 10.1021/acsenerylett.8b01153.

(182) Qiu, J.; Zheng, Y.; Xia, Y.; Chao, L.; Chen, Y.; Huang, W. Rapid Crystallization for Efficient 2D Ruddlesden–Popper (2DRP) Perovskite Solar Cells. **2019**, 29 (47), 1806831. DOI: <https://doi.org/10.1002/adfm.201806831>.

(183) Chen, J.; Xiong, Y.; Rong, Y.; Mei, A.; Sheng, Y.; Jiang, P.; Hu, Y.; Li, X.; Han, H. Solvent effect on the hole-conductor-free fully printable perovskite solar cells. *Nano Energy* **2016**, 27, 130-137. DOI: <https://doi.org/10.1016/j.nanoen.2016.06.047>.

(184) Cao, J.; Jing, X.; Yan, J.; Hu, C.; Chen, R.; Yin, J.; Li, J.; Zheng, N. Identifying the Molecular Structures of Intermediates for Optimizing the Fabrication of High-Quality Perovskite Films. *Journal of the American Chemical Society* **2016**, 138 (31), 9919-9926. DOI: 10.1021/jacs.6b04924.

(185) Wu, Y.; Islam, A.; Yang, X.; Qin, C.; Liu, J.; Zhang, K.; Peng, W.; Han, L. Retarding the crystallization of PbI₂ for highly reproducible planar-structured perovskite solar cells via sequential deposition. *Energy & Environmental Science* **2014**, 7 (9), 2934-2938, 10.1039/C4EE01624F. DOI: 10.1039/C4EE01624F.

- (186) Hendriks, K. H.; van Franeker, J. J.; Bruijnaers, B. J.; Anta, J. A.; Wienk, M. M.; Janssen, R. A. J. 2-Methoxyethanol as a new solvent for processing methylammonium lead halide perovskite solar cells. *Journal of Materials Chemistry A* **2017**, *5* (5), 2346-2354, 10.1039/C6TA09125C. DOI: 10.1039/C6TA09125C.
- (187) Noel, N. K.; Habisreutinger, S. N.; Wenger, B.; Klug, M. T.; Hörantner, M. T.; Johnston, M. B.; Nicholas, R. J.; Moore, D. T.; Snaith, H. J. A low viscosity, low boiling point, clean solvent system for the rapid crystallisation of highly specular perovskite films. *Energy & Environmental Science* **2017**, *10* (1), 145-152, 10.1039/C6EE02373H. DOI: 10.1039/C6EE02373H.
- (188) Wang, K.; Wu, C.; Hou, Y.; Yang, D.; Li, W.; Deng, G.; Jiang, Y.; Priya, S. A Nonionic and Low-Entropic MA(MMA)_nPbI₃-Ink for Fast Crystallization of Perovskite Thin Films. *Joule* **2020**, *4* (3), 615-630. DOI: <https://doi.org/10.1016/j.joule.2020.01.004>.
- (189) Li, L.; Chen, Y.; Liu, Z.; Chen, Q.; Wang, X.; Zhou, H. The Additive Coordination Effect on Hybrids Perovskite Crystallization and High-Performance Solar Cell. *Advanced materials* **2016**, *28* (44), 9862-9868. DOI: 10.1002/adma.201603021 From NLM.
- (190) Gardner, K. L.; Tait, J. G.; Merckx, T.; Qiu, W.; Paetzold, U. W.; Kootstra, L.; Jaysankar, M.; Gehlhaar, R.; Cheyns, D.; Heremans, P.; et al. Nonhazardous Solvent Systems for Processing Perovskite Photovoltaics. **2016**, *6* (14), 1600386. DOI: <https://doi.org/10.1002/aenm.201600386>.
- (191) Hsieh, T.-Y.; Pylnev, M.; Palomares, E.; Wei, T.-C. Exceptional Long Electron Lifetime in Methylammonium Lead Iodide Perovskite Solar Cell Made from Aqueous Lead Nitrate Precursor. **2020**, *30* (10), 1909644. DOI: <https://doi.org/10.1002/adfm.201909644>.
- (192) Wu, C.-G.; Chiang, C.-H.; Tseng, Z.-L.; Nazeeruddin, M. K.; Hagfeldt, A.; Grätzel, M. High efficiency stable inverted perovskite solar cells without current hysteresis. *Energy & Environmental Science* **2015**, *8* (9), 2725-2733, 10.1039/C5EE00645G. DOI: 10.1039/C5EE00645G.
- (193) Liu, D.; Traverse, C. J.; Chen, P.; Elinski, M.; Yang, C.; Wang, L.; Young, M.; Lunt, R. R. Aqueous-Containing Precursor Solutions for Efficient Perovskite Solar Cells. *Adv Sci (Weinh)* **2018**, *5* (1), 1700484. DOI: 10.1002/advs.201700484 From NLM.
- (194) Deegan, R. D.; Bakajin, O.; Dupont, T. F.; Huber, G.; Nagel, S. R.; Witten, T. A. Contact line deposits in an evaporating drop. *Physical Review E* **2000**, *62* (1), 756-765. DOI: 10.1103/PhysRevE.62.756.
- (195) L. Landau, B. L. Dragging of a Liquid by a Moving Plate. *Acta Physicochimica URSS* **1942**, *17* (42), 42-54.
- (196) Mallajosyula, A. T.; Fernando, K.; Bhatt, S.; Singh, A.; Alphenaar, B. W.; Blancon, J.-C.; Nie, W.; Gupta, G.; Mohite, A. D. J. A. M. T. Large-area hysteresis-free perovskite solar cells via temperature controlled doctor blading under ambient environment. **2016**, *3*, 96-102.
- (197) Ernst, M.; Herterich, J.-P.; Margenfeld, C.; Kohlstädt, M.; Würfel, U. Multilayer Blade-Coating Fabrication of Methylammonium-Free Perovskite Photovoltaic Modules with 66 cm² Active Area. **2022**, *6* (3), 2100535. DOI: <https://doi.org/10.1002/solr.202100535>.
- (198) Davis, R. L.; Jayaraman, S.; Chaikin, P. M.; Register, R. A. Creating Controlled Thickness Gradients in Polymer Thin Films via Flowcoating. *Langmuir* **2014**, *30* (19), 5637-5644. DOI: 10.1021/la501247x.
- (199) Ding, X.; Liu, J.; Harris, T. A. J. A. J. A review of the operating limits in slot die coating processes. **2016**, *62* (7), 2508-2524.
- (200) Ruschak, K. J. Limiting flow in a pre-metered coating device. *Chemical Engineering Science* **1976**, *31* (11), 1057-1060. DOI: [https://doi.org/10.1016/0009-2509\(76\)87026-1](https://doi.org/10.1016/0009-2509(76)87026-1).
- (201) Chen, C.; Gao, J.; Feng, S.-P. J. I. M. R. The strategies for widening processing windows for perovskite solar cells: a mini review on the role of solvent/antisolvent. **2022**, 1-22.

- (202) Liao, H. C.; Guo, P.; Hsu, C. P.; Lin, M.; Wang, B.; Zeng, L.; Huang, W.; Soe, C. M. M.; Su, W. F.; Bedzyk, M. J. J. A. E. M. Enhanced efficiency of hot-cast large-area planar perovskite solar cells/modules having controlled chloride incorporation. **2017**, 7 (8), 1601660.
- (203) Nie, W.; Tsai, H.; Asadpour, R.; Blancon, J.-C.; Neukirch, A. J.; Gupta, G.; Crochet, J. J.; Chhowalla, M.; Tretiak, S.; Alam, M. A. J. S. High-efficiency solution-processed perovskite solar cells with millimeter-scale grains. **2015**, 347 (6221), 522-525.
- (204) Gao, L.-L.; Li, C.-X.; Li, C.-J.; Yang, G.-J. Large-area high-efficiency perovskite solar cells based on perovskite films dried by the multi-flow air knife method in air. *Journal of Materials Chemistry A* **2017**, 5 (4), 1548-1557, 10.1039/C6TA09565H. DOI: 10.1039/C6TA09565H.
- (205) Ternes, S.; Börnhorst, T.; Schwenzer, J. A.; Hossain, I. M.; Abzieher, T.; Mehlmann, W.; Lemmer, U.; Scharfer, P.; Schabel, W.; Richards, B. S.; et al. Drying Dynamics of Solution-Processed Perovskite Thin-Film Photovoltaics: In Situ Characterization, Modeling, and Process Control. **2019**, 9 (39), 1901581. DOI: <https://doi.org/10.1002/aenm.201901581>.
- (206) Li, X.; Bi, D.; Yi, C.; Décoppet, J.-D.; Luo, J.; Zakeeruddin, S. M.; Hagfeldt, A.; Grätzel, M. J. S. A vacuum flash-assisted solution process for high-efficiency large-area perovskite solar cells. **2016**, 353 (6294), 58-62.
- (207) Ding, B.; Gao, L.; Liang, L.; Chu, Q.; Song, X.; Li, Y.; Yang, G.; Fan, B.; Wang, M.; Li, C. J. A. m.; et al. Facile and scalable fabrication of highly efficient lead iodide perovskite thin-film solar cells in air using gas pump method. **2016**, 8 (31), 20067-20073.
- (208) Gao, L.-L.; Liang, L.-S.; Song, X.-X.; Ding, B.; Yang, G.-J.; Fan, B.; Li, C.-X.; Li, C.-J. J. J. o. M. C. A. Preparation of flexible perovskite solar cells by a gas pump drying method on a plastic substrate. **2016**, 4 (10), 3704-3710.
- (209) Ding, B.; Li, Y.; Huang, S.-Y.; Chu, Q.-Q.; Li, C.-X.; Li, C.-J.; Yang, G.-J. Material nucleation/growth competition tuning towards highly reproducible planar perovskite solar cells with efficiency exceeding 20%. *Journal of Materials Chemistry A* **2017**, 5 (15), 6840-6848, 10.1039/C7TA00027H. DOI: 10.1039/C7TA00027H.
- (210) Martin, H. Heat and Mass Transfer between Impinging Gas Jets and Solid Surfaces. In *Advances in Heat Transfer*, Hartnett, J. P., Irvine, T. F. Eds.; Vol. 13; Elsevier, 1977; pp 1-60.
- (211) Ding, J.; Han, Q.; Ge, Q.-Q.; Xue, D.-J.; Ma, J.-Y.; Zhao, B.-Y.; Chen, Y.-X.; Liu, J.; Mitzi, D. B.; Hu, J.-S. Fully Air-Bladed High-Efficiency Perovskite Photovoltaics. *Joule* **2019**, 3 (2), 402-416. DOI: <https://doi.org/10.1016/j.joule.2018.10.025>.
- (212) Sandha Gupta, K. S. Structural and Thermo-Mechanical Study of Aluminum Coated Polyethylene Terphthalate (PET) Film. *International Journal of Innovative Research in Electronics and Communications* **2016**, 3 (2), 7-14.
- (213) Pandey, M.; Wang, Z.; Kapil, G.; Baranwal, A. K.; Hirotnani, D.; Hamada, K.; Hayase, S. Dependence of ITO-Coated Flexible Substrates in the Performance and Bending Durability of Perovskite Solar Cells. *Advanced Engineering Materials* **2019**, 21 (8), 1900288. DOI: 10.1002/adem.201900288 (accessed 2020/06/07).
- (214) Ragay, P. G.; Parks, R. W.; Garcia, L. A. R.; Kruzek, R. G. Rapid thermal firing IR conveyor furnace having high intensity heating section. United States 7,805,064, 2009.
- (215) Sowade, E.; Kang, H.; Mitra, K. Y.; Weiß, O. J.; Weber, J.; Baumann, R. R. Roll-to-roll infrared (IR) drying and sintering of an inkjet-printed silver nanoparticle ink within 1 second. *Journal of Materials Chemistry C* **2015**, 3 (45), 11815-11826, 10.1039/C5TC02291F. DOI: 10.1039/C5TC02291F.
- (216) Perelaer, J.; de Gans, B. J.; Schubert, U. S. Ink-jet Printing and Microwave Sintering of Conductive Silver Tracks. *Advanced Materials* **2006**, 18 (16), 2101-2104. DOI: 10.1002/adma.200502422.

- (217) Ouyang, Z.; Yang, M.; Whitaker, J. B.; Li, D.; van Hest, M. F. A. M. Toward Scalable Perovskite Solar Modules Using Blade Coating and Rapid Thermal Processing. *ACS Applied Energy Materials* **2020**, *3* (4), 3714-3720. DOI: 10.1021/acsaem.0c00180.
- (218) Fouassier, J. P. *Photoinitiation Photopolymerization and Photocuring*; Hanser/Gardner Publications, Inc., 1995.
- (219) Druffel, T.; Dharmadasa, R.; Lavery, B. W.; Ankireddy, K. Intense pulsed light processing for photovoltaic manufacturing. *Solar Energy Materials and Solar Cells* **2018**, *174*, 359-369. DOI: 10.1016/j.solmat.2017.09.010.
- (220) Ghahremani, A. H.; Martin, B.; Gupta, A.; Bahadur, J.; Ankireddy, K.; Druffel, T. Rapid fabrication of perovskite solar cells through intense pulse light annealing of SnO₂ and triple cation perovskite thin films. *Materials & Design* **2020**, *185*. DOI: 10.1016/j.matdes.2019.108237.
- (221) Xu, W.; Daunis, T. B.; Piper, R. T.; Hsu, J. W. P. Effects of Photonic Curing Processing Conditions on MAPbI₃ Film Properties and Solar Cell Performance. *ACS Applied Energy Materials* **2020**. DOI: 10.1021/acsaem.0c01243.
- (222) Feleki, B.; Bex, G.; Andriessen, R.; Galagan, Y.; Di Giacomo, F. Rapid and low temperature processing of mesoporous TiO₂ for perovskite solar cells on flexible and rigid substrates. *Materials Today Communications* **2017**, *13*, 232-240. DOI: <https://doi.org/10.1016/j.mtcomm.2017.09.007>.
- (223) Zhu, M.; Liu, W.; Ke, W.; Clark, S.; Secor, E. B.; Song, T.-B.; Kanatzidis, M. G.; Li, X.; Hersam, M. C. Millisecond-pulsed photonic annealing of tin oxide electron transport layers for efficient perovskite solar cells. *Journal of Materials Chemistry A* **2017**, *5* (46), 24110-24115.
- (224) Troughton, J.; Carnie, M. J.; Davies, M. L.; Charbonneau, C.; Jewell, E. H.; Worsley, D. A.; Watson, T. M. Photonic flash-annealing of lead halide perovskite solar cells in 1 ms. *Journal of Materials Chemistry A* **2016**, *4* (9), 3471-3476, 10.1039/C5TA09431C. DOI: 10.1039/C5TA09431C.
- (225) Bahadur, J.; Ghahremani, A. H.; Gupta, S.; Druffel, T.; Sunkara, M. K.; Pal, K. Enhanced moisture stability of MAPbI₃ perovskite solar cells through Barium doping. *Solar Energy* **2019**, *190*, 396-404. DOI: 10.1016/j.solener.2019.08.033.
- (226) Ghahremani, A. H.; Pishgar, S.; Bahadur, J.; Druffel, T. Intense Pulse Light Annealing of Perovskite Photovoltaics Using Gradient Flashes. *ACS Applied Energy Materials* **2020**, *3* (12), 11641-11654. DOI: 10.1021/acsaem.0c01520.
- (227) Lavery, B. W.; Kumari, S.; Konermann, H.; Draper, G. L.; Spurgeon, J.; Druffel, T. Intense Pulsed Light Sintering of CH₃NH₃PbI₃ Solar Cells. *ACS Applied Materials & Interfaces* **2016**, *8* (13), 8419-8426. DOI: 10.1021/acsami.5b10166.
- (228) Muydinov, R.; Seeger, S.; Vinoth Kumar, S. H. B.; Klimm, C.; Kraehnert, R.; Wagner, M. R.; Szyszka, B. Crystallisation behaviour of CH₃NH₃PbI₃ films: The benefits of sub-second flash lamp annealing. *Thin Solid Films* **2018**, *653*, 204-214. DOI: <https://doi.org/10.1016/j.tsf.2018.03.050>.
- (229) Xu, W.; Liu, Z.; Piper, R. T.; Hsu, J. W. P. Bayesian Optimization of photonic curing process for flexible perovskite photovoltaic devices. *Solar Energy Materials and Solar Cells* **2023**, *249*, 112055. DOI: <https://doi.org/10.1016/j.solmat.2022.112055>.
- (230) Martin, B.; Chapagain, S.; Armstrong, P.; Grapperhaus, C.; Reese, M. O.; Druffel, T. IPL-annealed mixed cation perovskites with robust coating window towards scalable manufacturing of commercial perovskite solar cells. *ACS Applied Energy Materials* **2023**.
- (231) Ankireddy, K.; Druffel, T.; Vunnam, S.; Filipič, G.; Dharmadasa, R.; Amos, D. A. Seed mediated copper nanoparticle synthesis for fabricating oxidation free interdigitated electrodes using intense pulse light sintering for flexible printed chemical sensors. *Journal of Materials Chemistry C* **2017**, *5* (42), 11128-11137. DOI: 10.1039/c7tc03522e.

- (232) Kang, H.; Sowade, E.; Baumann, R. R. Direct intense pulsed light sintering of inkjet-printed copper oxide layers within six milliseconds. *ACS Appl Mater Interfaces* **2014**, *6* (3), 1682-1687. DOI: 10.1021/am404581b.
- (233) Hösel, M.; Krebs, F. C. Large-scale roll-to-roll photonic sintering of flexo printed silver nanoparticle electrodes. *Journal of Materials Chemistry* **2012**, *22* (31). DOI: 10.1039/c2jm32977h.
- (234) Weiss, M.; Junginger, M.; Patel, M. K.; Blok, K. A review of experience curve analyses for energy demand technologies. *Technological Forecasting and Social Change* **2010**, *77* (3), 411-428. DOI: 10.1016/j.techfore.2009.10.009.
- (235) Chang, Nathan L.; Ho-Baillie, A.; Wenham, S.; Woodhouse, M.; Evans, R.; Tjahjono, B.; Qi, F.; Chong, C. M.; Egan, R. J. A techno-economic analysis method for guiding research and investment directions for c-Si photovoltaics and its application to Al-BSF, PERC, LDSE and advanced hydrogenation. *Sustainable Energy & Fuels* **2018**, *2* (5), 1007-1019, 10.1039/C8SE00047F. DOI: 10.1039/C8SE00047F.
- (236) IEA. Energy Prices: Overview. *IEA* **2021**, Paris.
- (237) Lindholm, F. A.; Fossum, J. G.; Burgess, E. L. Application of the superposition principle to solar-cell analysis. *IEEE Transactions on Electron Devices* **1979**, *26* (3), 165-171. DOI: 10.1109/T-ED.1979.19400.
- (238) Polat, S. HEAT AND MASS TRANSFER IN IMPINGEMENT DRYING. *Drying Technology* **1993**, *11* (6), 1147-1176. DOI: 10.1080/07373939308916894.
- (239) Etemoglu, A. B.; Can, M. Performance studies of energy consumption for single and multiple nozzle systems under impinging air jets. *Heat and Mass Transfer* **2013**, *49* (8), 1057-1070. DOI: 10.1007/s00231-013-1137-8.
- (240) Dharmadasa, R.; Jha, M.; Amos, D. A.; Druffel, T. Room Temperature Synthesis of a Copper Ink for the Intense Pulsed Light Sintering of Conductive Copper Films. *ACS applied materials & interfaces* **2013**, *5* (24), 13227-13234. DOI: 10.1021/am404226e.
- (241) Lavery, B. W.; Kumari, S.; Konermann, H.; Draper, G. L.; Spurgeon, J.; Druffel, T. Intense Pulsed Light Sintering of CH₃NH₃PbI₃ Solar Cells. *ACS applied materials & interfaces* **2016**, *8* (13), 8419-8426. DOI: 10.1021/acsami.5b10166.
- (242) Peng, C.; Jia, Z.; Bianculli, D.; Li, T.; Lou, J. In situ electro-mechanical experiments and mechanics modeling of tensile cracking in indium tin oxide thin films on polyimide substrates. **2011**, *109* (10), 103530. DOI: 10.1063/1.3592341.
- (243) Dharmadasa, R.; Dharmadasa, I. M.; Druffel, T. Intense Pulsed Light Sintering of Electrodeposited CdS Thin Films. **2014**, *16* (11), 1351-1361. DOI: <https://doi.org/10.1002/adem.201400008>.
- (244) Martin, B.; Yang, M.; Bramante, R. C.; Amerling, E.; Gupta, G.; van Hest, M. F. A. M.; Druffel, T. Fabrication of flexible perovskite solar cells via rapid thermal annealing. *Materials Letters* **2020**, *276*, 128215. DOI: <https://doi.org/10.1016/j.matlet.2020.128215>.
- (245) Kumar, A.; Bieri, M.; Reindl, T.; Aberle, A. G. Economic Viability Analysis of Silicon Solar Cell Manufacturing: Al-BSF versus PERC. *Energy Procedia* **2017**, *130*, 43-49. DOI: <https://doi.org/10.1016/j.egypro.2017.09.412>.
- (246) Woodhouse, M. A.; Smith, B.; Ramdas, A.; Margolis, R. M. *Crystalline silicon photovoltaic module manufacturing costs and sustainable pricing: 1H 2018 Benchmark and Cost Reduction Road Map*; National Renewable Energy Lab.(NREL), Golden, CO (United States), 2019.
- (247) Chang, N. L.; Ho-Baillie, A. W. Y.; Vak, D.; Gao, M.; Green, M. A.; Egan, R. J. Manufacturing cost and market potential analysis of demonstrated roll-to-roll perovskite photovoltaic cell processes. *Solar Energy Materials and Solar Cells* **2018**, *174*, 314-324. DOI: <https://doi.org/10.1016/j.solmat.2017.08.038>.

- (248) Gao, L.-L.; Zhang, K.-J.; Chen, N.; Yang, G.-J. Boundary layer tuning induced fast and high performance perovskite film precipitation by facile one-step solution engineering. *Journal of Materials Chemistry A* **2017**, *5* (34), 18120-18127, 10.1039/C7TA05012G. DOI: 10.1039/C7TA05012G.
- (249) Bruening, K.; Dou, B.; Simonaitis, J.; Lin, Y.-Y.; van Hest, M. F. A. M.; Tassone, C. J. Scalable Fabrication of Perovskite Solar Cells to Meet Climate Targets. *Joule* **2018**, *2* (11), 2464-2476. DOI: <https://doi.org/10.1016/j.joule.2018.09.014>.
- (250) Wang, Y.; Wu, J.; Zhang, P.; Liu, D.; Zhang, T.; Ji, L.; Gu, X.; David Chen, Z.; Li, S. Stitching triple cation perovskite by a mixed anti-solvent process for high performance perovskite solar cells. *Nano Energy* **2017**, *39*, 616-625. DOI: <https://doi.org/10.1016/j.nanoen.2017.07.046>.
- (251) Cao, X.; Zhi, L.; Jia, Y.; Li, Y.; Cui, X.; Zhao, K.; Ci, L.; Ding, K.; Wei, J. High annealing temperature induced rapid grain coarsening for efficient perovskite solar cells. *Journal of colloid and interface science* **2018**, *524*, 483-489. DOI: 10.1016/j.jcis.2018.04.019 From NLM.
- (252) Sánchez, S.; Hua, X.; Günzler, A.; Bermúdez-Ureña, E.; Septiadi, D.; Saliba, M.; Steiner, U. Flash Infrared Pulse Time Control of Perovskite Crystal Nucleation and Growth from Solution. *Crystal Growth & Design* **2020**, *20* (2), 670-679. DOI: 10.1021/acs.cgd.9b01083.
- (253) Greener, J.; Pearson, G.; Cakmak, M. *Roll-to-Roll Manufacturing: Process Elements and Recent Advances*; Wiley, 2018.
- (254) Piper, R. T.; Daunis, T. B.; Xu, W.; Schroder, K. A.; Hsu, J. W. P. Photonic Curing of Nickel Oxide Transport Layer and Perovskite Active Layer for Flexible Perovskite Solar Cells: A Path Towards High-Throughput Manufacturing. **2021**, *9*, Original Research. DOI: 10.3389/fenrg.2021.640960.
- (255) Chapagain, S.; Chandrasekhar, P. S.; McGott, D.; Bramante, R. C.; van Hest, M. F. A. M.; Reese, M. O.; Druffel, T.; Grapperhaus, C. A. Direct Deposition of Nonaqueous SnO₂ Dispersion by Blade Coating on Perovskites for the Scalable Fabrication of p-i-n Perovskite Solar Cells. *ACS Applied Energy Materials* **2021**, *4* (10), 10477-10483. DOI: 10.1021/acsaem.1c01287.
- (256) Chandrasekhar, P. S.; Chapagain, S.; Blake, M.; Armstrong, P. J.; Grapperhaus, C.; Druffel, T. L. Rapid scalable fabrication of roll-to-roll slot-die coated flexible perovskite solar cells using intense pulse light annealing. *Sustainable Energy & Fuels* **2022**, *6* (23), 5316-5323, 10.1039/D2SE00911K. DOI: 10.1039/D2SE00911K.
- (257) Zuo, C.; Vak, D.; Angmo, D.; Ding, L.; Gao, M. J. N. E. One-step roll-to-roll air processed high efficiency perovskite solar cells. **2018**, *46*, 185-192.
- (258) Dou, B.; Whitaker, J. B.; Bruening, K.; Moore, D. T.; Wheeler, L. M.; Ryter, J.; Breslin, N. J.; Berry, J. J.; Garner, S. M.; Barnes, F. S.; et al. Roll-to-Roll Printing of Perovskite Solar Cells. *ACS Energy Letters* **2018**, *3* (10), 2558-2565. DOI: 10.1021/acseenergylett.8b01556.
- (259) Abbas, M.; Zeng, L.; Guo, F.; Rauf, M.; Yuan, X.-C.; Cai, B. A Critical Review on Crystal Growth Techniques for Scalable Deposition of Photovoltaic Perovskite Thin Films. *Materials* **2020**, *13*, 1-42. DOI: 10.3390/ma13214851.
- (260) Deng, Y.; Van Brackle, C. H.; Dai, X.; Zhao, J.; Chen, B.; Huang, J. Tailoring solvent coordination for high-speed, room-temperature blading of perovskite photovoltaic films. *Sci Adv* **2019**, *5* (12), eaax7537. DOI: 10.1126/sciadv.aax7537.
- (261) Su, J.; Cai, H.; Ye, X.; Zhou, X.; Yang, J.; Wang, D.; Ni, J.; Li, J.; Zhang, J. Efficient Perovskite Solar Cells Prepared by Hot Air Blowing to Ultrasonic Spraying in Ambient Air. *ACS applied materials & interfaces* **2019**, *11* (11), 10689-10696. DOI: 10.1021/acsaami.9b01843.
- (262) Sánchez, S.; Vallés-Pelarda, M.; Alberola-Borràs, J.-A.; Vidal, R.; Jerónimo-Rendón, J. J.; Saliba, M.; Boix, P. P.; Mora-Seró, I. Flash infrared annealing as a cost-effective and low environmental impact processing method for planar perovskite solar cells. *Materials Today* **2019**, *31*, 39-46. DOI: <https://doi.org/10.1016/j.mattod.2019.04.021>.

- (263) Chen, Q.; Ma, T.; Wang, F.; Liu, Y.; Liu, S.; Wang, J.; Cheng, Z.; Chang, Q.; Yang, R.; Huang, W. J. A. S. Rapid Microwave-Annealing Process of Hybrid Perovskites to Eliminate Miscellaneous Phase for High Performance Photovoltaics. **2020**, 7 (12), 2000480.
- (264) Martin, B.; Amos, D.; Brehob, E.; van Hest, M. F. A. M.; Druffel, T. Techno-economic analysis of roll-to-roll production of perovskite modules using radiation thermal processes. *Applied Energy* **2022**, 307, 118200. DOI: <https://doi.org/10.1016/j.apenergy.2021.118200>.
- (265) Huang, T.; Tan, S.; Nuryyeva, S.; Yavuz, I.; Babbe, F.; Zhao, Y.; Abdelsamie, M.; Weber, M. H.; Wang, R.; Houk, K. N. J. S. a. Performance-limiting formation dynamics in mixed-halide perovskites. **2021**, 7 (46), eabj1799.
- (266) Cheng, Y.; Peng, Y.; Jen, A. K.-Y.; Yip, H.-L. J. S. R. Development and challenges of metal halide perovskite solar modules. **2022**, 6 (3), 2100545.
- (267) Gao, L.; Yang, G. Organic-Inorganic Halide Perovskites: From Crystallization of Polycrystalline Films to Solar Cell Applications. *Solar RRL* **2020**, 4 (2). DOI: 10.1002/solr.201900200 WorldCat.org.
- (268) Deng, Y.; Van Brackle, C. H.; Dai, X.; Zhao, J.; Chen, B.; Huang, J. Tailoring solvent coordination for high-speed, room-temperature blading of perovskite photovoltaic films. *Science Advances* **2019**, 5 (12), eaax7537. DOI: 10.1126/sciadv.aax7537.
- (269) Di, J.; Chang, J.; Liu, S. Recent progress of two-dimensional lead halide perovskite single crystals: Crystal growth, physical properties, and device applications. *EcoMat* **2020**, 2 (3), e12036, <https://doi.org/10.1002/eom2.12036>. DOI: <https://doi.org/10.1002/eom2.12036> (accessed 2022/12/20).
- (270) Su, J.; Cai, H.; Yang, J.; Ye, X.; Han, R.; Ni, J.; Li, J.; Zhang, J. Perovskite Ink with an Ultrawide Processing Window for Efficient and Scalable Perovskite Solar Cells in Ambient Air. *ACS Applied Materials and Interfaces* **2020**, 12 (3), 3531-3538. DOI: 10.1021/acsami.9b17141 WorldCat.org.
- (271) Park, N.-G.; Zhu, K. Scalable fabrication and coating methods for perovskite solar cells and solar modules. *Nature Reviews Materials* **2020**, 5 (5), 333-350. DOI: 10.1038/s41578-019-0176-2.
- (272) Martin, B.; van Hest, M.; Yang, M.; Druffel, T. Fabrication of flexible perovskite solar cells via rapid thermal annealing. In *2020 47th IEEE Photovoltaic Specialists Conference (PVSC)*, 2020; IEEE: pp 1786-1788.
- (273) Arora, N.; Greco, A.; Meloni, S.; Hinderhofer, A.; Mattoni, A.; Rothlisberger, U.; Hagenlocher, J.; Caddeo, C.; Zakeeruddin, S. M.; Schreiber, F.; et al. Kinetics and energetics of metal halide perovskite conversion reactions at the nanoscale. *Communications Materials* **2022**, 3 (1), 22. DOI: 10.1038/s43246-022-00239-1.

APPENDIX

COGS:

A1 – Key to Tabs

Tab in Spreadsheet	Description
Assumptions	List of global assumptions used throughout spreadsheet
Charts	Updated graphs of important results
Materials usage	Chemical and material use for the proposed PSC design
Learning rate	Model for cost of chemicals/materials as a function of quantity
Material	Cost of materials as a function of web speed
Equipment	Equipment costs per item
Utilities	Cost of electricity used in production
Labor	Cost of labor to operate facility
Evaporation	Utility cost to evaporate and recapture solvent
Prod Costs	Summation of all production costs from previous tables
Monte Carlo	Monte Carlo simulation used to estimate uncertainty effect of materials and utilities
Oven Comp	Comparison of the energy requirements per m ² of a traditional oven and IPL

A2 – Assumptions

Web Assumptions		
Web Width		1.5 m
Module Assumptions		
Module Power Conversion Efficiency (PCE)		18
Max Power		180 W/m ²
Factory Assumptions		
Average Yearly Uptime		0.85
Average Yield		0.9
Average yearly Uptime (hours)		7884 hours
Labor Assumptions		
Labor overhead rate		50%
Equipment Assumptions		
Depreciation		10 years
salvage value		5%
installation costs		10,000 \$/m ²
side access		4 m
Maintenance Rate		4% capex per year
Building Assumptions		
Footprint		10000 m ²
Depreciation		20 years
cost		1000 \$/m ²
building depreciation		\$ 500,000 per year
Material Assumptions		
perovskite density	4.823	g/cm ³
DMF density	0.944	g/cm ³
DMSO density	1.1	g/cm ³
Utilities Assumptions		
Cost of Electricity	0.0683	\$/kW-hr

A3 – Production Costs

Overall output (CV)	Area to Produce (m ²)	Production Rate (m/min)	Materials (\$Millions)			Labor (\$Millions)	Utilities (\$Million)	Maintenance (\$Million)	Depreciation (\$Million)	Total Costs (\$/m ²)			Total Costs (\$/W)		
			Low	Mid	High					Low	Ave	High	Low	Ave	High
0.08	500,000.00	0.70	\$ 3.56	\$ 6.30	\$ 8.73	2.693	0.010	0.601	2.030	17.80	23.27	28.14	0.0989	0.1293	0.1563
0.16	1,000,000.00	1.41	\$ 6.06	\$ 11.34	\$ 16.24	2.693	0.021	0.601	2.030	11.40	16.68	21.59	0.0633	0.0927	0.1199
0.24	1,500,000.00	2.11	\$ 8.26	\$ 15.99	\$ 23.35	2.693	0.031	0.601	2.030	9.08	14.23	19.14	0.0504	0.0791	0.1063
0.32	2,000,000.00	2.82	\$ 10.30	\$ 20.41	\$ 30.21	2.693	0.042	0.601	2.030	7.83	12.89	17.79	0.0435	0.0716	0.0988
0.41	2,500,000.00	3.52	\$ 12.22	\$ 24.66	\$ 36.90	2.693	0.052	0.601	2.030	7.04	12.01	16.91	0.0391	0.0667	0.0939
0.49	3,000,000.00	4.23	\$ 14.05	\$ 28.78	\$ 43.44	2.693	0.063	0.601	2.030	6.48	11.39	16.27	0.0360	0.0633	0.0904
0.57	3,500,000.00	4.93	\$ 15.81	\$ 32.80	\$ 49.87	2.693	0.073	0.601	2.030	6.06	10.91	15.79	0.0337	0.0606	0.0877
0.65	4,000,000.00	5.64	\$ 17.51	\$ 36.74	\$ 56.20	2.693	0.084	0.601	2.030	5.73	10.54	15.40	0.0318	0.0585	0.0856
0.73	4,500,000.00	6.34	\$ 19.16	\$ 40.59	\$ 62.45	2.693	0.094	0.601	2.030	5.46	10.22	15.08	0.0303	0.0568	0.0838
0.81	5,000,000.00	7.05	\$ 20.77	\$ 44.39	\$ 68.63	2.693	0.105	0.601	2.030	5.24	9.96	14.81	0.0291	0.0554	0.0823
0.89	5,500,000.00	7.75	\$ 22.34	\$ 48.12	\$ 74.74	2.693	0.115	0.601	2.030	5.05	9.74	14.58	0.0281	0.0541	0.0810
0.97	6,000,000.00	8.46	\$ 23.88	\$ 51.81	\$ 80.79	2.693	0.126	0.601	2.030	4.89	9.54	14.37	0.0272	0.0530	0.0799
1.05	6,500,000.00	9.16	\$ 25.39	\$ 55.45	\$ 86.80	2.693	0.136	0.601	2.030	4.74	9.37	14.19	0.0265	0.0522	0.0788
1.13	7,000,000.00	9.87	\$ 26.87	\$ 59.04	\$ 92.75	2.693	0.147	0.601	2.030	4.61	9.21	14.04	0.0259	0.0516	0.0779
1.22	7,500,000.00	10.57	\$ 28.33	\$ 62.60	\$ 98.66	2.693	0.157	0.601	2.030	4.51	9.07	13.92	0.0254	0.0510	0.0771
1.30	8,000,000.00	11.27	\$ 29.76	\$ 66.12	\$ 104.53	2.693	0.168	0.601	2.030	4.42	8.95	13.82	0.0250	0.0505	0.0764
1.38	8,500,000.00	11.98	\$ 31.18	\$ 69.61	\$ 110.36	2.693	0.178	0.601	2.030	4.35	8.86	13.74	0.0247	0.0501	0.0758
1.46	9,000,000.00	12.68	\$ 32.57	\$ 73.07	\$ 116.15	2.693	0.189	0.601	2.030	4.27	8.79	13.67	0.0244	0.0497	0.0752
1.54	9,500,000.00	13.39	\$ 33.95	\$ 76.50	\$ 121.91	2.693	0.199	0.601	2.030	4.21	8.74	13.60	0.0242	0.0494	0.0747
1.62	10,000,000.00	14.09	\$ 35.31	\$ 79.90	\$ 127.64	2.693	0.210	0.601	2.030	4.17	8.69	13.54	0.0240	0.0491	0.0742
1.70	10,500,000.00	14.80	\$ 36.65	\$ 83.27	\$ 133.34	2.693	0.220	0.601	2.030	4.12	8.65	13.49	0.0238	0.0488	0.0737
1.78	11,000,000.00	15.50	\$ 37.98	\$ 86.62	\$ 139.01	2.693	0.231	0.601	2.030	4.08	8.61	13.44	0.0236	0.0485	0.0732
1.86	11,500,000.00	16.21	\$ 39.29	\$ 89.95	\$ 144.66	2.693	0.242	0.601	2.030	4.04	8.57	13.39	0.0234	0.0482	0.0727
1.94	12,000,000.00	16.91	\$ 40.60	\$ 93.26	\$ 150.28	2.693	0.252	0.601	2.030	4.00	8.53	13.34	0.0232	0.0479	0.0722
2.03	12,500,000.00	17.62	\$ 41.88	\$ 96.54	\$ 155.87	2.693	0.263	0.601	2.030	3.97	8.50	13.29	0.0230	0.0476	0.0717
2.11	13,000,000.00	18.32	\$ 43.16	\$ 99.81	\$ 161.44	2.693	0.273	0.601	2.030	3.93	8.46	13.25	0.0228	0.0473	0.0712
2.19	13,500,000.00	19.03	\$ 44.43	\$ 103.05	\$ 166.99	2.693	0.284	0.601	2.030	3.89	8.42	13.21	0.0226	0.0470	0.0707
2.27	14,000,000.00	19.73	\$ 45.68	\$ 106.28	\$ 172.51	2.693	0.294	0.601	2.030	3.85	8.38	13.17	0.0224	0.0467	0.0702
2.35	14,500,000.00	20.44	\$ 46.92	\$ 109.49	\$ 178.02	2.693	0.305	0.601	2.030	3.81	8.34	13.13	0.0222	0.0464	0.0697
2.43	15,000,000.00	21.14	\$ 48.16	\$ 112.68	\$ 183.51	2.693	0.315	0.601	2.030	3.77	8.30	13.09	0.0220	0.0461	0.0692
2.51	15,500,000.00	21.84	\$ 49.38	\$ 115.86	\$ 188.97	2.693	0.326	0.601	2.030	3.73	8.26	13.05	0.0218	0.0458	0.0687
2.59	16,000,000.00	22.55	\$ 50.60	\$ 119.02	\$ 194.42	2.693	0.337	0.601	2.030	3.69	8.22	13.01	0.0216	0.0455	0.0682
2.67	16,500,000.00	23.25	\$ 51.80	\$ 122.17	\$ 199.85	2.693	0.347	0.601	2.030	3.65	8.18	12.97	0.0214	0.0452	0.0677
2.75	17,000,000.00	23.96	\$ 53.00	\$ 125.30	\$ 205.27	2.693	0.358	0.601	2.030	3.61	8.14	12.93	0.0212	0.0449	0.0672
2.84	17,500,000.00	24.66	\$ 54.19	\$ 128.42	\$ 210.66	2.693	0.368	0.601	2.030	3.57	8.10	12.89	0.0210	0.0446	0.0667
2.92	18,000,000.00	25.37	\$ 55.37	\$ 131.52	\$ 216.04	2.693	0.379	0.601	2.030	3.53	8.06	12.85	0.0208	0.0443	0.0662
3.00	18,500,000.00	26.07	\$ 56.54	\$ 134.61	\$ 221.41	2.693	0.390	0.601	2.030	3.49	8.02	12.81	0.0206	0.0440	0.0657
3.08	19,000,000.00	26.78	\$ 57.71	\$ 137.69	\$ 226.79	2.693	0.400	0.601	2.030	3.45	7.98	12.77	0.0204	0.0437	0.0652
3.16	19,500,000.00	27.48	\$ 58.87	\$ 140.76	\$ 232.09	2.693	0.411	0.601	2.030	3.41	7.94	12.73	0.0202	0.0434	0.0647
3.24	20,000,000.00	28.19	\$ 60.02	\$ 143.82	\$ 237.42	2.693	0.421	0.601	2.030	3.37	7.90	12.69	0.0200	0.0431	0.0642
3.32	20,500,000.00	28.89	\$ 61.17	\$ 146.86	\$ 242.72	2.693	0.432	0.601	2.030	3.33	7.86	12.65	0.0198	0.0428	0.0637
3.40	21,000,000.00	29.60	\$ 62.31	\$ 149.89	\$ 248.02	2.693	0.443	0.601	2.030	3.29	7.82	12.61	0.0196	0.0425	0.0632
3.48	21,500,000.00	30.30	\$ 63.44	\$ 152.91	\$ 253.30	2.693	0.453	0.601	2.030	3.25	7.78	12.57	0.0194	0.0422	0.0627
3.56	22,000,000.00	31.01	\$ 64.56	\$ 155.92	\$ 258.56	2.693	0.464	0.601	2.030	3.21	7.74	12.53	0.0192	0.0419	0.0622

A4 – Materials Usage

Raw Material	CAS #	Weight (kg/m ²)			
Chlorobenzene (CB)	108-90-7	0.000438			
Ethanol (EtOH)	64-17-5	0.003943			
Nickel Oxide (NiO)	1313-99-1	0.000117			
Dimethylsulfoxide (DMSO)	7-68-5	0.000890			
Dimethylformamide (DMF)	68-12-2	0.006871			
Lead Iodide (PbI ₂)	10101-63-0	0.001864			
Methylammonium Iodide (MAI)	14965-49-2	0.000643			
Tin Oxide (SnO ₂)	18282-10-5	0.000499			
Water	7732-18-6	0.016118			
Copper (Cu)	7440-50-8	0.001673			
1-Methoxy-2-Propanol (PM)	107-98-2	0.015060			
Perovskite Weight Calculation					
Molarity	1	m ²			Reference
Film thickness	0.5	micron			10.1002/solr.201800034 Find R2R reference
Wet Film Thickness	10.27	micron			
Wet Film Volume	1.03E-05	m ³			
		0.01	L		
Molarity	1				Wang, S.; Ma, Z.; Liu, B.; Wu, W.; Zhu, Y.; Ma, R.; Wang, C., High-Performance Perovskite Solar Cells with Large Grain-Size obtained by using the Lewis Acid-Base Adduct of Thiourea. Solar RRL 2018, 2 (6), 1800034.
PbI ₂ :[PbI ₂ +MAI]	0.5				
DMF:[DMF+DMSO]	0.9				
Material	Molar Density (kg/mol)	Density (kg/m ³)	Weight (kg/L)	wt%	mass (kg/m ²)
PbI ₂	0.461	6160	0.231	0.182	0.00186
MAI	0.159	-	0.080	0.063	0.00064
DMF	0.073	944	0.850	0.669	0.00687
DMSO	0.078	1100	0.110	0.087	0.00089
CH ₃ NH ₃ PbI ₃	-	4823	-	-	-
			1.270		
SnO₂ Weight Calculation					
Film thickness	0.05	micron	Reference		Smith, J. A.; Game, O. S.; Bishop, J. E.; Spooner, E. L. K.; Kilbride, R. C.; Greenland, C.; Jayaprakash, R.; Alanazi, T. I.; Cassella, E. J.;
Wet Film Thickness	14.1	micron	10.1021/acsam.0c00525		
Volume per m ²	0.0000141	m ³ /m ²			
Material	Density (kg/mol)	Density (kg/m ³)	Weight (kg/L)	wt%	mass (kg/m ²)
SnO ₂	-	6950	-	0.03	0.000498506
H ₂ O	-	1000	-	0.97	0.016118345
NiO Weight Calculation					
Film thickness	0.02	micron	Reference		Liang, X.; Yi, Q.; Bai, S.; Dai, X.; Wang, X.; Ye, Z.; Gao, F.; Zhang, F.; Sun, B.; Jin, Y., Synthesis of Unstable Colloidal Inorganic Nanocrystals through
Wet Film Thickness	4.622314622	micron	10.1021/nl501763z		
Volume per m ²	4.62231E-06				
Material	Density (kg/mol)	Density (kg/m ³)	Weight (kg/L)	wt%	mass (kg/m ²)
NiO	-	6670	-	0.026	0.000116956
CB	-	1110	-	0.0974	0.000438135
EtOH	-	789	-	0.8766	0.003943214
Copper Weight Calculation					
Film thickness	0.1	micron	Reference		Ankireddy, K.; Druffel, T.; Vunnam, S.; Filipič, G.; Dharmadasa, R.; Amos, D. A., Seed mediated copper nanoparticle synthesis for fabricating
Wet Film Thickness	9.717391304	micron	10.1039/c7tc03522e		
Volume per m ²	9.71739E-06	m ³ /m ²			
Material	Density (kg/mol)	Density (kg/m ³)	Weight (kg/L)	wt%	mass (kg/m ²)
Cu	-	8940	-	0.1	0.001673335
PM	-	920	-	0.9	0.015060013

A5 – Learning Rate ITO/PET

ITO coated PET							
LR	15%		LR	10%		LR	7%
b	-0.234		b	-0.152		b	-0.105
A	\$ 154.57		A	\$ 92.59		A	\$ 69.00
	500			500			500
\$ 36.00	500	m ²	\$ 36.00	500	m ²	\$ 36.00	500 m ²
Yearly output	Q	P					Mathews et.al.
0.08	500000	\$ 7.13	500000	\$ 12.60	500000	\$ 17.47	\$ 13.78
0.97	6000000	\$ 3.98	6000000	\$ 8.63	6000000	\$ 13.47	\$ 10.87
1.94	12000000	\$ 3.38	12000000	\$ 7.77	12000000	\$ 12.52	\$ 10.18
3.00	18500000	\$ 3.06	18500000	\$ 7.28	18500000	\$ 11.97	\$ 9.77
3.97	24500000	\$ 2.86	24500000	\$ 6.97	24500000	\$ 11.62	\$ 9.51

A6 – Material Costs

			Total Cost per m²		
Factory Throughput (m ² /yr)	Output (GW)	Web speed (m/min)	Low Total Cost per area (\$/m ²)	Mid Total Cost per area (\$/m ²)	High Total Cost per area (\$/m ²)
500,000	0.08	0.70	\$ 13.25	\$ 18.72	\$ 23.59
1,000,000	0.16	1.41	\$ 11.59	\$ 16.87	\$ 21.78
1,500,000	0.24	2.11	\$ 10.72	\$ 15.87	\$ 20.78
2,000,000	0.32	2.82	\$ 10.15	\$ 15.20	\$ 20.11
2,500,000	0.41	3.52	\$ 9.73	\$ 14.70	\$ 19.60
3,000,000	0.49	4.23	\$ 9.40	\$ 14.31	\$ 19.19
3,500,000	0.57	4.93	\$ 9.13	\$ 13.98	\$ 18.86
4,000,000	0.65	5.64	\$ 8.90	\$ 13.70	\$ 18.57
4,500,000	0.73	6.34	\$ 8.70	\$ 13.47	\$ 18.32
5,000,000	0.81	7.05	\$ 8.53	\$ 13.25	\$ 18.10
5,500,000	0.89	7.75	\$ 8.38	\$ 13.07	\$ 17.91
6,000,000	0.97	8.46	\$ 8.24	\$ 12.90	\$ 17.73
6,500,000	1.05	9.16	\$ 8.12	\$ 12.74	\$ 17.57
7,000,000	1.13	9.87	\$ 8.01	\$ 12.60	\$ 17.42
7,500,000	1.22	10.57	\$ 7.90	\$ 12.47	\$ 17.28
8,000,000	1.30	11.27	\$ 7.81	\$ 12.35	\$ 17.15
8,500,000	1.38	11.98	\$ 7.72	\$ 12.24	\$ 17.04
9,000,000	1.46	12.68	\$ 7.64	\$ 12.14	\$ 16.92
9,500,000	1.54	13.39	\$ 7.56	\$ 12.04	\$ 16.82
10,000,000	1.62	14.09	\$ 7.49	\$ 11.95	\$ 16.72
10,500,000	1.70	14.80	\$ 7.42	\$ 11.86	\$ 16.63
11,000,000	1.78	15.50	\$ 7.36	\$ 11.78	\$ 16.54
11,500,000	1.86	16.21	\$ 7.30	\$ 11.70	\$ 16.46
12,000,000	1.94	16.91	\$ 7.24	\$ 11.63	\$ 16.38
12,500,000	2.03	17.62	\$ 7.18	\$ 11.55	\$ 16.30
13,000,000	2.11	18.32	\$ 7.13	\$ 11.49	\$ 16.23
13,500,000	2.19	19.03	\$ 7.08	\$ 11.42	\$ 16.16
14,000,000	2.27	19.73	\$ 7.03	\$ 11.36	\$ 16.09
14,500,000	2.35	20.44	\$ 6.99	\$ 11.30	\$ 16.03
15,000,000	2.43	21.14	\$ 6.94	\$ 11.24	\$ 15.97
15,500,000	2.51	21.84	\$ 6.90	\$ 11.19	\$ 15.91
16,000,000	2.59	22.55	\$ 6.86	\$ 11.14	\$ 15.85
16,500,000	2.67	23.25	\$ 6.82	\$ 11.08	\$ 15.79
17,000,000	2.75	23.96	\$ 6.78	\$ 11.04	\$ 15.74
17,500,000	2.84	24.66	\$ 6.75	\$ 10.99	\$ 15.69
18,000,000	2.92	25.37	\$ 6.71	\$ 10.94	\$ 15.64
18,500,000	3.00	26.07	\$ 6.68	\$ 10.90	\$ 15.59
19,000,000	3.08	26.78	\$ 6.64	\$ 10.85	\$ 15.54
19,500,000	3.16	27.48	\$ 6.61	\$ 10.81	\$ 15.49
20,000,000	3.24	28.19	\$ 6.58	\$ 10.77	\$ 15.45
20,500,000	3.32	28.89	\$ 6.55	\$ 10.73	\$ 15.41
21,000,000	3.40	29.60	\$ 6.52	\$ 10.69	\$ 15.36
21,500,000	3.48	30.30	\$ 6.49	\$ 10.65	\$ 15.32
22,000,000	3.56	31.01	\$ 6.46	\$ 10.62	\$ 15.28
22,500,000	3.65	31.71	\$ 6.44	\$ 10.58	\$ 15.24
23,000,000	3.73	32.41	\$ 6.41	\$ 10.55	\$ 15.21
23,500,000	3.81	33.12	\$ 6.39	\$ 10.51	\$ 15.17
24,000,000	3.89	33.82	\$ 6.36	\$ 10.48	\$ 15.13
24,500,000	3.97	34.53	\$ 6.34	\$ 10.45	\$ 15.10
25,000,000	4.05	35.23	\$ 6.31	\$ 10.42	\$ 15.06
25,500,000	4.13	35.94	\$ 6.29	\$ 10.39	\$ 15.03
26,000,000	4.21	36.64	\$ 6.27	\$ 10.36	\$ 14.99
26,500,000	4.29	37.35	\$ 6.25	\$ 10.33	\$ 14.96
27,000,000	4.37	38.05	\$ 6.22	\$ 10.30	\$ 14.93
27,500,000	4.46	38.76	\$ 6.20	\$ 10.27	\$ 14.90
28,000,000	4.54	39.46	\$ 6.18	\$ 10.24	\$ 14.87
28,500,000	4.62	40.17	\$ 6.16	\$ 10.21	\$ 14.84
29,000,000	4.70	40.87	\$ 6.14	\$ 10.19	\$ 14.81
29,500,000	4.78	41.58	\$ 6.12	\$ 10.16	\$ 14.78
30,000,000	4.86	42.28	\$ 6.10	\$ 10.14	\$ 14.75
30,500,000	4.94	42.98	\$ 6.09	\$ 10.11	\$ 14.72
31,000,000	5.02	43.69	\$ 6.07	\$ 10.09	\$ 14.70
31,500,000	5.10	44.39	\$ 6.05	\$ 10.06	\$ 14.67
32,000,000	5.18	45.10	\$ 6.03	\$ 10.04	\$ 14.64
32,500,000	5.27	45.80	\$ 6.01	\$ 10.02	\$ 14.62
33,000,000	5.35	46.51	\$ 6.00	\$ 9.99	\$ 14.59
33,500,000	5.43	47.21	\$ 5.98	\$ 9.97	\$ 14.57
34,000,000	5.51	47.92	\$ 5.96	\$ 9.95	\$ 14.54
34,500,000	5.59	48.62	\$ 5.95	\$ 9.93	\$ 14.52
35,000,000	5.67	49.33	\$ 5.93	\$ 9.90	\$ 14.50
35,500,000	5.75	50.03	\$ 5.92	\$ 9.88	\$ 14.47
36,000,000	5.83	50.74	\$ 5.90	\$ 9.86	\$ 14.45
36,500,000	5.91	51.44	\$ 5.89	\$ 9.84	\$ 14.43
37,000,000	5.99	52.14	\$ 5.87	\$ 9.82	\$ 14.40
37,500,000	6.08	52.85	\$ 5.86	\$ 9.80	\$ 14.38
38,000,000	6.16	53.55	\$ 5.84	\$ 9.78	\$ 14.36
38,500,000	6.24	54.26	\$ 5.83	\$ 9.76	\$ 14.34
39,000,000	6.32	54.96	\$ 5.82	\$ 9.75	\$ 14.32
39,500,000	6.40	55.67	\$ 5.80	\$ 9.73	\$ 14.30
40,000,000	6.48	56.37	\$ 5.79	\$ 9.71	\$ 14.28
40,500,000	6.56	57.08	\$ 5.78	\$ 9.69	\$ 14.26
41,000,000	6.64	57.78	\$ 5.76	\$ 9.67	\$ 14.24
41,500,000	6.72	58.49	\$ 5.75	\$ 9.66	\$ 14.22
42,000,000	6.80	59.19	\$ 5.74	\$ 9.64	\$ 14.20
42,500,000	6.89	59.90	\$ 5.72	\$ 9.62	\$ 14.18
43,000,000	6.97	60.60	\$ 5.71	\$ 9.60	\$ 14.16
43,500,000	7.05	61.31	\$ 5.70	\$ 9.59	\$ 14.14
44,000,000	7.13	62.01	\$ 5.69	\$ 9.57	\$ 14.12
44,500,000	7.21	62.71	\$ 5.68	\$ 9.56	\$ 14.11
45,000,000	7.29	63.42	\$ 5.66	\$ 9.54	\$ 14.09
45,500,000	7.37	64.12	\$ 5.65	\$ 9.52	\$ 14.07
46,000,000	7.45	64.83	\$ 5.64	\$ 9.51	\$ 14.05
46,500,000	7.53	65.53	\$ 5.63	\$ 9.49	\$ 14.03
47,000,000	7.61	66.24	\$ 5.62	\$ 9.48	\$ 14.02
47,500,000	7.70	66.94	\$ 5.61	\$ 9.46	\$ 14.00
48,000,000	7.78	67.65	\$ 5.60	\$ 9.45	\$ 13.98
48,500,000	7.86	68.35	\$ 5.59	\$ 9.43	\$ 13.97
49,000,000	7.94	69.06	\$ 5.58	\$ 9.42	\$ 13.95

A7 – Equipment

Layer	Process	Equipment	Cost	Salvage	Depreciation	Maintenance	Length	
R2R	Roll-to-Roll Equipment	Rollers, Motors, CPUs, control systems, Electrical	\$ 620,000	\$ 31,000	\$ 58,900	\$ 24,800	5	New Era Converting
	Surface Treatment	Corona discharge	\$ 50,000	\$ 2,500	\$ 4,750	\$ 2,000	0.5	Enercon
Device Architecture	Laser Scribe (P1,P2,P3)	Yb:SHG laser	\$ 100,000	\$ 5,000	\$ 9,500	\$ 4,000	0.5	Chang R2R model
SnO ₂ (CTL)	Print SnO ₂	Slot-Die	\$ 343,564	\$ 17,178	\$ 32,639	\$ 13,743	1	Coating Tech Slot-Dies
	Evaporate Solvent	Airknife*	\$ 575,000	\$ 28,750	\$ 54,625	\$ 23,000	1	exAir + Ingersoll Rand
	Post-process (Anneal)	IPL	\$ 3,000,000	\$ 150,000	\$ 285,000	\$ 120,000	1	Xenon Corp
MAPbI ₃ (Absorber)	Print MAPbI ₃	Slot-Die	\$ 343,564	\$ 17,178	\$ 32,639	\$ 13,743	1	Coating Tech Slot-Dies
	Evaporate Solvent	Airknife*	\$ 575,000	\$ 28,750	\$ 54,625	\$ 23,000	1	exAir + Ingersoll Rand
	Post-process (Anneal)	IPL	\$ 2,500,000	\$ 125,000	\$ 237,500	\$ 100,000	1	Xenon Corp
NiO (CTL)	Print NiO	Slot-Die	\$ 343,564	\$ 17,178	\$ 32,639	\$ 13,743	1	Coating Tech Slot-Dies
	Evaporate Solvent	Airknife*	\$ 575,000	\$ 28,750	\$ 54,625	\$ 23,000	1	exAir + Ingersoll Rand
	Post-process (IPL)	IPL	\$ 2,500,000	\$ 125,000	\$ 237,500	\$ 100,000	1	Xenon Corp
Cu (Electrode)	Print Cu	Slot-Die	\$ 343,564	\$ 17,178	\$ 32,639	\$ 13,743	1	Coating Tech Slot-Dies
	Evaporate Solvent	Airknife*	\$ 575,000	\$ 28,750	\$ 54,625	\$ 23,000	1	exAir + Ingersoll Rand
	Post-process	IPL	\$ 2,500,000	\$ 125,000	\$ 237,500	\$ 100,000	1	Xenon Corp
Laminate	Lamination	Laminator	\$ 28,000	\$ 1,400	\$ 2,660	\$ 1,120	0.5	Chang et. al. Model
Testing	Module Testing	Module Tester	\$ 58,000	\$ 2,900	\$ 5,510	\$ 2,320		Chang et. al. Model
Install	Installation	Installation costs	\$ 1,017,500		\$ 101,750			
				Total	\$ 1,529,624	\$ 601,210		

A8 – Utilities

Layer	Process	Utilities (\$/m ²)			
Device Architecture	Laser Scribe (P1,P2,P3)	0.008000			
NiO (CTL)	Evaporate Solvent	0.000409			
	Post-process (IPL)	0.001518			
MAPbI ₃ (Absorber)	Evaporate Solvent	0.003056			
	Post-process (Anneal)	0.000683			
SnO ₂ (CTL)	Evaporate Solvent	0.001740			
	Post-process (Anneal)	0.003794			
Cu (Electrode)	Evaporate Solvent	0.000003			
	Post-process	0.001708			
Laminate	Lamination*	0.000000			
Testing		0.000000			
		Total	0.0209		

Layer	Wet Thickness (m)	Viscosity (cP)	Slot Width (micron)	Land Length (cm)	Power (J/W-s ²)
NiO	4.62E-06	1	20	2.5	1922.92
MAPbI ₃	1.03E-05	0.9	20	2.5	8539.37
SnO ₂	1.41E-05	0.9	20	2.5	16103.61
Cu					0.00

IPL Utility Cost	Energy Density (kJ/m ²)	Pulses	kW-hr/m ²	Cost (\$/m ²)	
SnO ₂	40	5	0.0556	0.0038	
MAPbI ₃	12	3	0.0100	0.0007	
NiO	20	4	0.0222	0.0015	
Cu	30	3	0.0250	0.0017	
				Total	0.0077027

A9 – Labor

Position	Position Code	Number	Mean Hourly Wage
Supervisor	17-2112	1	\$ 44.55
Prepress Technician	51-5111	2	\$ 20.45
Printing Press Operator	51-5112	4	\$ 18.80
Maintenance	49-9040	1	\$ 26.60
QA	19-2031	1	\$ 40.46
Total			\$ 227.71
Yearly Total/line			\$ 1,795,265.64

A10 – Oven Comparison

Layer	Plastic Heating (kW)	LEL (%)	Max C (g/m ³)	Airflow (m ³ /sec)	Airflow Power (kW)	Losses (kW)	IPL (kW-hr/m ²)	Oven (kW-hr/m ²)
SnO ₂	6.2			0.35	33.46875	11.3	0.0555556	0.0566319
MAPbI ₃	6.2	2.2	1.839854973	0.933629	89.27831	11.3	0.01	0.1186426
NiO	6.2	3.3	4.378391578	0.225152	21.53016	11.3	0.0222222	0.0433668
Cu	6.2	1.6	1.085460599	3.468577	331.6826	11.3	0.025	0.3879807
Total							0.1127778	0.6066221

CURRICULUM VITAE

Blake Martin

Ph. D. Candidate, Chemical Engineering

Address:

216 Eastern Parkway
University of Louisville, Ernst Hall
Louisville, KY 40292

Home Address:

9710 Meadow Vale Dr, Louisville, KY 40242

LinkedIn: <https://www.linkedin.com/in/blake-martin-76a9a2121/>

Phone: 859-797-5429

Email: bemartin93@gmail.com

Education

- May 2017 - present **University of Louisville, Louisville, KY, pursuing PhD in Chemical Engineering**
J.B. Speed School of Engineering
Advisors: Thad Druffel, PhD; Gautam Gupta, PhD
GPA: 3.750
- Aug 2016 – May 2017 **University of Louisville, Louisville, KY, post-baccalaureate in Chemical Engineering**
- Aug 2012 – May 2016 **Centre College, Danville, KY, B.S. in Chemistry**

Research Experience

- Sep 2019 – Dec 2019 **Research Scientist, National Renewable Energy Laboratory, Golden, CO**
- Conducted research on rapid manufacturing of perovskite solar cells using rapid thermal processing
 - Worked extensively with solar simulator, 2D glass scribe, blade-coater, spin-coater, glove boxes, rapid thermal processor, and thermal evaporator systems
- Mar 2017 - present **Research Scientist, University of Louisville, Louisville, KY**
- Developed methods to produce high-throughput perovskite solar cells on temperature sensitive flexible substrates using radiative annealing techniques
 - Conducted research on a novel corrosion testing system by blending elements of electrochemistry and gel electrophoresis
- Jul 2016 – Aug 2016 **Research Scientist, University of Cincinnati, Cincinnati, OH**

- Optimize RNA isolation protocol for *C. neoformans* using both homogenization/pulverization and GITC extraction methods
- Operated autoclave to sanitize used glassware, plated cell cultures, “cold shocked” samples with liquid nitrogen for homogenization, operated bullet blender homogenizer, and reviewed weekly, topical research articles

Sep 2014 – May
2015

Research Scientist, Centre College, Danville, KY

- Developed synthetic procedures to produce potential MurA inhibitors, used NMR and IR characterization techniques, and performed Diels-Alder reaction protocols
- Presented at 2015 Centre College RICE symposium

Awards

- RE3 Clean Energy Entrepreneurship: Student Pitch Competition - 1st place

Publications/Workshops/Conferences

Journal Papers:

1. Martin, B.; Amos, D.; Brehob, E.; van Hest, M. F. A. M.; Druffel, T., Techno-economic analysis of roll-to-roll production of perovskite modules using radiation thermal processes. *Applied Energy* **2022**, *307*, 118200.
2. Martin, B.; Yang, M.; Bramante, R. C.; Amerling, E.; Gupta, G.; van Hest, M. F. A. M.; Druffel, T., Fabrication of flexible perovskite solar cells via rapid thermal annealing. *Materials Letters* **2020**, *276*, 128215.
3. Martin, B.; Chapagain, S.; Armstrong, P.; Grapperhaus, C.; Reese, M. O.; Druffel, T., IPL-annealed mixed cation perovskites with robust coating window towards scalable manufacturing of commercial perovskite solar cells. *ACS Applied Energy Materials* **2023**.
4. Chapagain, S.; Martin, B.; Armstrong, P.; Perkins, C. L.; Reese, M. O.; Druffel, T.; Grapperhaus, C., High Performing Inverted Flexible Perovskite Solar Cells via Solution Phase Deposition of Yttrium-Doped SnO₂ Directly on Perovskite. *ACS Applied Energy Materials* **2023**.
5. Ghahremani, A. H.; Martin, B.; Gupta, A.; Bahadur, J.; Ankireddy, K.; Druffel, T., Rapid fabrication of perovskite solar cells through intense pulse light annealing of SnO₂ and triple cation perovskite thin films. *Materials & Design* **2020**, *185*, 108237.
6. Ghahremani, A. H.; Martin, B.; Ankireddy, K.; Druffel, T., Rapid processing of perovskite solar cells through pulsed photonic annealing: a review. *Journal of Coatings Technology and Research* **2019**, *16* (6), 1637-1642.
7. Bahadur, J.; Ghahremani, A. H.; Martin, B.; Pishgar, S.; Druffel, T.; Sunkara, M. K.; Pal, K., A study on the material characteristics of low temperature cured SnO₂ films for perovskite solar cells under high humidity. *Journal of Materials Science: Materials in Electronics* **2019**, *30* (20), 18452-18461.
8. Bahadur, J.; Ghahremani, A. H.; Martin, B.; Druffel, T.; Sunkara, M. K.; Pal, K., Solution processed Mo doped SnO₂ as an effective ETL in the fabrication of low temperature planer perovskite solar cell under ambient conditions. *Organic Electronics* **2019**, *67*, 159-167.

9. Ankireddy, K.; Ghahremani, A. H.; Martin, B.; Gupta, G.; Druffel, T., Rapid thermal annealing of CH₃NH₃PbI₃ perovskite thin films by intense pulsed light with aid of diiodomethane additive. *Journal of Materials Chemistry A* **2018**, *6* (20), 9378-9383.

Conference Papers/Presentations:

- June – August 2020 **2020 47th IEEE Photovoltaic Specialists Conference (PVSC)**
- **Blake Martin**, Maikel van Hest, Mengjin Yang, Thad Druffel, “Fabrication of Flexible Perovskite Solar Cells via Rapid Thermal Annealing”, Poster presentation
- Oct 2019 **236th ECS Meeting, Hilton Atlanta, Atlanta, GA**
- **Blake Martin**, Amir Hossein Ghahremani, and Thad Druffel, “Scalable Hole-Transport Materials for Roll-to-Roll Perovskite Photovoltaic Modules”, Oral presentation
- Jul 2018 **Kentucky Nanoscale & Additive Manufacturing Symposium, Speed Art Museum, Louisville, KY**
- **Blake Martin**, “Laminated Perovskite Solar Cells Compatible with Roll-to-Roll Manufacturing”, poster presentation
- Mar 2017 **Renewable Energy & Energy Efficiency (RE3) Workshop, Muhammed Ali Center, Louisville, KY**
- **Blake Martin**, Brandon Lavery, Venkata Vasiraju, Gautam Gupta, Thad Druffel “Tuning of composition and reaction conditions of inorganic-organic hybrid perovskites to model crystal growth”, poster presentation
 - Alexander Gupta, Jianchao Zhao, **Blake Martin**, Theodore Kalbfleisch, Thad Druffel, and Gautam Gupta “Catalysts for Hydrogen Evolution Reaction using Intense Pulsed Light”, poster presentation
 - **Blake Martin** “Biochar”, presentation given during Clean Energy Entrepreneurship: Student Pitch Competition

Workshops:

- Aug 2018 **Hands on Photovoltaic Experience (HOPE) at National Renewable Energy Laboratory, Golden, CO**
- Learned from pioneers in the field of photovoltaics about different types of PV materials, commonly used characterization equipment, and standard methods for reporting power conversion efficiency

Technical Experience

Glove Box System

- Developed standard operating procedure (SOP) and train new users for glove box system
- Conduct routine checks & refill consumable components in glove box system (pump fluids, air filters, solvent trap systems)
- Facilitate hazardous waste removal from system & collection through coordination with Department of Environmental Health & Safety at the University of Louisville

- Coordinate with local compressed gas supplier to regularly deliver and install N₂ feed line into glove box system
- Reinstall butyl gloves in the event of a blow out or significant wear and tear
- Carry out catalyst regeneration protocol by regulating regeneration gas flow using repurposed flowmeter
- Removed a compromised rotary pump used for exhaust and circulation between glove box units and installed a repurposed rotary pump.

Scanning Electron Microscope (SEM) instrument

- Worked to optimize beam intensity, working distance and beam shift to overcome charging of non-conductive substrates
- Executed sample preparation methods to address excessive charging concerns (gold sputtering, etc.)

X-Ray Diffraction (XRD) Analyzer

- Examined a wide range of materials (perovskites, metal oxides, pure metals) for a variety of different applications (corrosion, crystalline PV materials, etc.)
- Addressed staging issues for thin films deposited onto substrates that did not match XRD focal length

Roll-to-Roll printing machine

- Install components (slot-die coater, laminar flow knife, IR heater, Intense Pulsed Light) to carry out perovskite thin film deposition and conversion for photovoltaic applications
- Reorder and reorganize components within roll-to-roll machine for tailored layer depositions
- Careful, precise instrument installation as optimized slot-die gap equals 100 μm with little margin for error

Intense Pulse Light

- Constructed Xenon™ S-2210 High-Energy pulsed light lamp housing and high-voltage electrical connections with
- Installed IPL machine within the Roll-to-Roll housing to allow inline annealing after perovskite deposition

2D-Laser engraver

- Assembly of support scaffold using 80/20 T-slot aluminum bars to house laser and motors for precise (<0.1mm) etching of perovskite solar cell materials

Solar Simulator

- Constructed enclosure for solar simulator lamp that simultaneously allows ease of access and protection of user from harmful light exposure
- Designed electrochemical testing program using NOVA 2.1 software to measure JV and IS data from perovskite solar cells
- Worked with scientists at the NREL to standardize reference cells for calibration of solar simulator lamp

Lab Manager

- Established lab safety protocols in compliance with DEHS lab safety protocols
- Facilitate hazardous waste collection within the lab and coordinate with DEHS for removal

Work/Leadership Experience

- Aug 2018 – May 2020 **President, Chemical Engineering Graduate Student Association, University of Louisville, Louisville, KY**
- Aug 2019– May 2020 **Senator Proxy, Graduate Student Council, University of Louisville, Louisville, KY**
- Sep 2013 – May 2016 **Centre College Residential Assistant, Danville, KY**

Teaching and Tutoring Experience

- Jan 2018 – Apr 2018 **Teaching Assistant, CHE 498 Unit Operations**
- Established method to determine conversion for lab scale packed-bed reactor
 - Reinstalled tubing, controls, and seals to make the catalytic reactor operational
- May 2018 – Aug 2018 **Teaching Assistant, CHE 253 Materials Science**
- Taught classes and developed exams, lesson plans, and weekly assignments
- Aug 2017 – Dec 2017 **Teaching Assistant, CHE 653 Polymer Processing**
- Jan 2017 – May 2018 **Physics Tutor for local high school student**

Activities/Volunteer Work

- 2018 – present **Big, Big Brothers Big Sisters of Kentuckiana, Louisville, KY**
- 2012 – 2015 **Athlete, Centre College Football, Danville, KY**
- 2012 – 2015 **Camp Horsin' Around, Perryville, KY**
- 2013 – 2014 **Danville-Boyle County Humane Society, Danville, KY**